

UNIVERSITY OF SOUTHERN QUEENSLAND

Stellar Photometry
for the
Shared Skies Partnership

A dissertation submitted by
Jason Monsour, BEng

For the Award of
Master of Science

Department of Biological and Physical Sciences
University of Southern Queensland

July 2010

This page is intentionally blank.

© Copyright

Jason Monsour

2010

This page is intentionally blank.

Abstract

This thesis forms a feasibility study into the use of remotely operable telescopes at Mount Kent Observatory in Australia and Moore Observatory in the USA for precision stellar photometry by distance education students, for an initiative called the Shared Skies Partnership.

The thesis introduces stellar activity and exoplanet science as motivations for stellar photometry and the use of remotely operable telescopes for education through research. Methods for stellar photometry are reviewed as are the technical details of the telescopes at Mt Kent and Moore Observatories. Light curve results of standard stars, spotted stars and an exoplanet transit are presented. Discussion of these results is made, and suggestions offered regarding the use of pipeline processing software and robotic operation of the telescopes as future developments.

It is concluded that scientifically useful stellar photometry can be obtained using remotely operable telescopes at Mount Kent and Moore Observatories but general use must await the implementation of robust robotic telescope operation and pipeline processing of data to avoid the downloading of large amounts of raw data over the internet.

This page is intentionally blank.

Certification of Dissertation

I certify that the ideas, experimental work, results, analyses, software and conclusions reported in this dissertation are entirely my own effort, except where otherwise acknowledged. I also certify that the work is original and has not been previously submitted for any other award, except where otherwise acknowledged.

Signature of Candidate and Date

Endorsement

Signature of Supervisor and Date

This page is intentionally blank.

Acknowledgements

It has only been possible to write this thesis with the help of a great many people. In particular, I would like to acknowledge and thank a number of people who played a major role in helping me develop and refine the thesis.

Firstly, special thanks are due to my supervisor, Dr Brad Carter at the University of Southern Queensland for his ongoing encouragement, support and guidance. His enthusiastic approach to astronomy education and thoughtful insights have been an inspiration to me.

Special thanks are also due to Dr Rhodes Hart at the University of Southern Queensland for his support with the observations at Mount Kent Observatory. His dedication and willingness to assist me has made my observation work a smooth and effortless activity for which I am very grateful.

I am also indebted to Ian Waite for his patient tutelage in the use of IRAF and for supplying observations of HIP71933 made at Mount Kent Observatory with the CDK20 telescope.

The role played by Professor John Kielkopf of the University of Louisville Kentucky in establishing the Southern Skies Program and funding the installation and upkeep of the Mount Kent Observatory CDK20 telescope is acknowledged with gratitude. I'd also like to thank Karen Collins, also from the University of Louisville, for her assistance in gathering exoplanet transit observations using the Moore Observatory telescopes.

Finally, a special word of thanks to my family for their understanding and support by creating an environment in which it was possible to write this thesis.

Jason Monsour

This page is intentionally blank.

CONTENTS

Chapter 1: Introduction	1
1.1 Foreword	1
1.2 Stellar photometry	2
1.3 Zeeman Doppler imaging	2
1.3.1 Mapping stellar spots & magnetic fields	2
1.3.2 Photometry to determine rotation period	2
1.3.3 Photometry and low-latitude star spots	3
1.4 Exoplanet detection techniques	4
1.4.1 Astrometric displacement	4
1.4.2 Pulsar timing	4
1.4.3 Doppler spectroscopy	4
1.4.3.1 Anglo-Australian Planet Search (AAPS)	4
1.4.4 Transit photometry	5
1.4.4.1 Intrinsic stellar activity & exoplanet effects	6
1.4.4.2 Rossiter McLaughlin effect	7
1.4.4.3 Transit survey	7
1.4.4.4 Transit plus radial velocity observations	8
1.4.5 Gravitational microlensing	8
1.4.5.1 Targets of opportunity	9
1.4.5.2 MicroFUN	9
1.5 Digital Science Partnership	10
1.5.1 Science education through research	11
1.5.2 The teaching-research nexus	11
1.5.3 Astronomy, science & technology	11
1.5.4 MKO astronomical distance education	11
1.5.5 Student observing	12
1.5.6 Robotic observing	12
1.5.7 Data processing in astronomy	13
1.5.8 DSP and remote live observing	13

1.5.9	Hybrid robotic system	13
1.5.10	Stellar photometry for the Shared Skies Partnership	13
Chapter 2: Facilities & Methods		15
2.1	Mt Kent Observatory	15
2.1.1	Site	15
2.1.2	Educational Development Group building	15
2.1.3	MKO telescopes	16
2.1.3.1	Webb telescope	16
2.1.3.2	O'Mara telescope	16
2.1.3.3	University of Louisville telescopes at MKO	16
2.1.4	CCD camera	16
2.1.5	Dome	17
2.1.6	Communications	17
2.1.7	Additional instrumentation	18
2.2	Moore Observatory	18
2.2.1	Site	18
2.2.2	Main Building	19
2.2.3	Moore Observatory telescopes	19
2.2.3.1	Ritchey Chrétien telescope	19
2.2.3.2	Corrected Dall-Kirkham telescope (CDK20n)	19
2.2.3.3	Schmidt-Cassegrain	19
2.2.4	CCD cameras	20
2.2.5	Dome	20
2.2.6	Communications	20
2.2.7	Additional instrumentation	20
2.3	Common equipment	21
2.3.1	Corrected Dall-Kirkham telescope	21
2.3.2	Computer hardware	21
2.3.2.1	INDI Servers	21
2.3.3	Computer software	22

2.3.3.1	XmCCD	22
2.3.3.2	XmGuider	22
2.3.3.3	XmTel	23
2.3.3.4	XmDome	23
2.3.3.5	XEphem	24
2.4	Remote observing	25
2.4.1	Differences with traditional observing	25
2.4.2	Internet	25
2.4.3	Data transfer	26
2.4.4	Unix	26
2.4.5	Virtual Private Network	27
2.4.6	Skype	27
2.4.7	Planning	27
2.5	Photometry	28
2.5.1	Shot noise	28
2.5.2	Readout noise	28
2.5.3	CCD linearity	29
2.5.4	Photon transfer curve	29
2.6	Atmospherics	31
2.6.1	Astronomical seeing	31
2.6.2	Scintillation	31
2.6.3	Extinction	31
2.7	Data reduction	32
2.7.1	IRAF	32
2.7.2	Image calibration	32
2.7.2.1	Dark current	32
2.7.2.2	Dark frames	33
2.7.2.3	Flat frames	33
2.8	Observing procedures	34
2.8.1	Target selection	34
2.8.2	Capturing bias, dark & flat frames	35
2.8.3	Exposure time	36

2.8.4	Observing run	36
2.9	Calibration of Graham’s E2-Region	36
2.9.1	Photometry techniques	38
2.9.1.1	Aperture photometry	38
2.9.1.2	Point spread function photometry	39
2.9.2	Differential photometry	39
2.10	Data interpretation	40
2.10.1	Use of photometry to support DI	40
2.10.2	Transit light curves for exoplanet studies	40
2.10.2.1	Period	40
2.10.2.2	Transit depth	40
2.10.2.3	Transit duration	41
2.10.2.4	Transit shape	41
2.10.2.5	Out-of-transit features	41
2.10.3	Photometry for the MicroFUN microlensing network	42
Chapter 3: Results		43
3.1	Introduction	43
3.2	Observing log	43
3.3	Summary of results	43
3.4	Graham’s E2-Region photometric standards	44
3.4.1	Photometric precision	46
3.5	Spotted star HIP71933	47
3.6	Spotted star HIP93378	50
3.7	WASP 12b exoplanet transit	52
Chapter 4: Discussion		57
4.1	Introduction	57
4.2	Requirements for star spot imaging	57
4.3	Requirements for exoplanet transit studies	57
4.4	Performance of the RC24 telescope	58

4.5	Performance of the CDK20 telescopes	58
4.6	Prospects for the CDK700 telescope	59
4.7	O'Mara robotic telescope	59
4.8	Photometric precision of the MKO & Moore telescopes	60
4.9	Data quantity & processing	61
Chapter 5: Conclusions		63
5.1	Introduction	63
5.2	Recommendations	64
5.2.1	Remote telescope operation	64
5.2.2	Future development & work activities	65
5.3	Thesis summary	66
Appendix A Differential photometry		67
A1	Introduction	67
A2	First order extinction	67
A3	Second order extinction	69
A4	Transformation coefficients	70
A5	Perform differential photometry	71
Appendix B E2-Region photometry results		75
Appendix C IRAF photometry processing		79
C1	Introduction	79
C2	IRAF guide	80
C3	Sort data	81
C4	Startup & configure IRAF	81
C4.1	Observatory configuration	81
C4.2	Navigate to appropriate folder	83

C5	Update headers	83
C5.1	Set Julian date	84
C5.2	Set airmass	85
C6	Image calibration	85
C6.1	Bias frames	85
C6.2	Dark frames	86
C6.3	Flat frames	87
C6.4	Science frames	88
C7	Image verification	89
C8	Image rotation	90
C9	Image alignment	90
C9.1	Examine images & record target position	91
C9.2	Calculate coordinate shifts	92
C9.3	Image alignment	92
C10	Star identification	93
C10.1	Determine full width at half maximum	93
C10.2	Choose appropriate apertures	93
C11	Photometry	97
C12	Scilab function: pixel_shift(pixel)	100
C13	Scilab function: position_sort(p)	100
C14	Scilab function: light_c20(num_star)	100
C15	Scilab function: sex2dec_fits(t)	102
References		103

LIST OF FIGURES

Figure 1.1	Maximum entropy brightness reconstruction for R58.....	3
Figure 1.2	Simulated transit event and light curve	5
Figure 1.3	TrES-1 phased light curve from HST observations.....	6
Figure 1.4	The Rossiter-McLaughlin Effect	7
Figure 1.5	Kepler’s first five exoplanet discoveries	8
Figure 1.6	Microlensing light curve of OGLE-2005-BLG-390L b	9
Figure 2.1	EDG Building at Mt Kent Observatory	15
Figure 2.2	Mount Kent Observatory	17
Figure 2.3	MKO Microwave data link.....	18
Figure 2.4	Moore Observatory main building.....	19
Figure 2.5	Moore Observatory remote/robotic telescope dome.....	20
Figure 2.6	XmCCD & XmGuider screen shots	23
Figure 2.7	XmTel & XmDome screen shots.....	24
Figure 2.8	XEphem screen shots.....	25
Figure 2.9	Example photon transfer curves	30
Figure 2.10	Example calibration images.....	37
Figure 2.11	Pre and post image calibration frames of Graham’s E2 Region....	37
Figure 2.12	Aperture photometry.....	38
Figure 2.13	Exoplanet light curve.....	41
Figure 3.1	Graham’s E2-Region star identification frame.....	44
Figure 3.2	Graham’s E2:C standard star light curve.....	45
Figure 3.3	Graham’s E2:s standard star light curve.....	46

Figure 3.4	Differential photometry accuracy as a function of magnitude.....	47
Figure 3.5	HIP71933 star identification frame.....	48
Figure 3.6	Spotted star HIP71933 - 25 March 2009	49
Figure 3.7	Spotted star HIP71933 - 27 March 2009	49
Figure 3.8	HIP93378 star identification frame.....	50
Figure 3.9	Spotted star HIP93378 - 27 June 2010	51
Figure 3.10	Spotted star HIP93378 - 03 July 2010	52
Figure 3.11	WASP12 star identification frame	53
Figure 3.12	Raw WASP12b transit light curve (CDK20n).....	54
Figure 3.13	Corrected WASP12b transit light curve (CDK20n)	55
Figure 3.14	Exoplanet transit light curve of WASP12b (RC24).....	56
Figure 3.15	Exoplanet transit light curve of WASP12b (RC24 & CDK20n) ...	56
Figure A2.1	Example Magnitude Vs Air Mass plot.....	69
Figure B0.1	Graham's E2-Region standard star light curves - set 1/4	75
Figure B0.2	Graham's E2-Region standard star light curves - set 2/4	76
Figure B0.3	Graham's E2-Region standard star light curves - set 3/4	77
Figure B0.4	Graham's E2-Region standard star light curves - set 4/4	78
Figure C2.1	IRAF Photometry processing flowchart	80
Figure C3.1	Observation data management.....	81
Figure C5.1	Example IRAF obsdb.dat user defined observatories.....	83
Figure C5.2	IRAF asthedit parameters	84
Figure C5.3	IRAF setjd parameters	84
Figure C5.4	IRAF setairmass parameters	85

Figure C6.1	IRAF zerocombine parameters	86
Figure C6.2	IRAF darkcombine parameters	87
Figure C6.3	IRAF flatcombine parameters.....	88
Figure C7.1	IRAF imexamine parameters	89
Figure C8.1	IRAF rotate parameters.....	90
Figure C9.1	IRAF imalign parameters	92
Figure C10.1	IRAF datapars parameters	94
Figure C10.2	IRAF findpars parameters.....	94
Figure C10.3	IRAF daofind parameters	95
Figure C10.4	IRAF tvmark parameters	96
Figure C10.5	IRAF tvmark example	97
Figure C11.1	IRAF fitskypars parameters	98
Figure C11.2	IRAF photpars parameters	98
Figure C11.3	IRAF phot parameters.....	99

This page is intentionally blank.

LIST OF TABLES

Table 3.1	Journal of photometric observations.....	43
Table 3.2	Photometry target summary.....	43
Table 3.3	Graham’s E2-Region targets.....	44
Table 3.4	HIP71933 comparison and check stars.....	47
Table 3.5	HIP93378 comparison and check stars.....	50
Table 3.6	WASP12b transit ephemeris data	52
Table 3.7	WASP12 comparison and check stars	53
Table 5.1	Approximations for extinction coefficients.....	67

This page is intentionally blank.

Chapter 1: Introduction

1.1 Foreword

Traditionally, mass-market telescopes have been the domain of amateur astronomers the world over, but have not found the same utility in the professional arena. These telescopes are typically a half metre aperture or less and are loosely termed “small telescopes”. They are popular amongst amateurs because of their low cost, ease of use and availability, but have significant draw-backs including limiting magnitude and optical aberrations. With the constant improvement in their quality, performance and aperture and accompanying CCD cameras, these telescopes have become potentially important scientific tools for both amateur and professional astronomers alike. One area in which small telescopes can excel is the monitoring of stellar variability.

This thesis outlines the use of telescopes at Mount Kent Observatory (Queensland, Australia) and Moore Observatory (Kentucky, USA) for use in monitoring stellar variability such as star spot and exoplanet studies carried out at USQ. The key motivations for undertaking this research project are (1) the detection and monitoring of exoplanets, and (2) star spot photometry to study stellar magnetic activity. To date, these facilities have not been used for exoplanet work and have had only limited use for star spot work, and so their performance in these niche areas is largely unknown. In the past, the telescopes at Mount Kent and Moore have instead been used for astrophotography and educational activities supporting the University of Southern Queensland (USQ) and the University of Louisville (UoL) courses.

The key advantage of smaller telescopes for stellar photometry is that in general, they can be allocated large periods of time at short notice to follow interesting objects and events. The results presented in this thesis pave the way for robotic stellar photometry for student research, using remote access to northern and southern hemisphere telescopes and automatic photometric processing of observations. Such capability can add significantly to the educational and research capacity of any astronomical observatory.

USQ and UoL have collaborated as part of a program called the The Digital Science Partnership. Its main objectives are astronomy education, research training and provision of outreach projects. Section 1.5 provides further information on the formation and goals of the partnership. Under the partnership, the UoL has provided funding that was used to procure identical Celestron (now PlaneWave Instruments) branded CDK20 telescopes that have been installed at Moore Observatory, Kentucky USA and Mount Kent Observatory (MKO), Queensland, Australia. For convenience, the northern telescope is designated CDK20n, and the southern, CDK20s.

In addition to the above CDK20 telescopes, a 0.6m aperture RC Optical Systems Inc. Ritchey-Chrétien RC24 telescope has been installed at Moore Observatory, and a PlaneWave Instruments CDK700 0.7m telescope is due to be installed at MKO later

in 2010. Taken together, the availability of the CDK20, CDK700 and RC24 telescopes allows for extensive monitoring of both northern and southern stars, and time-series photometry that uses the longitude difference to advantage.

1.2 Stellar photometry

Photometry is the science of measuring the intensity of an object's electromagnetic radiation. Many stars exhibit variations in their luminosity that can be detected by ground-based telescopes. Whilst photometric measurements of these targets is an interesting and fulfilling activity in its own right, the data can also provide useful information about the target, thus adding to the scientific knowledge base. There are many organisations that focus on the art and science of photometry, two of the more prominent groups being the American Association of Variable Star Observers ([AAVSO](#)) and the International Amateur-Professional Photoelectric Photometry association ([IAPPP](#)).

1.3 Zeeman Doppler imaging

1.3.1 Mapping stellar spots & magnetic fields

Doppler Imaging (DI) is a technique for imaging the giant sunspot-like features and prominences of solar-type stars with intense solar-type activity. Zeeman Doppler Imaging (ZDI) adds to this by allowing the mapping of magnetic fields. ZDI makes use of the ability of magnetic fields to polarize the light present in spectral lines formed in the stellar atmosphere - the Zeeman effect. The periodic modulation of Zeeman signatures due to the Doppler effect during stellar rotation is employed to reconstruct maps or images of magnetic field vectors at the stellar surface ([Marsden 2005](#)). ZDI also provides star spot maps using the intensity and Doppler information present in the spectral lines.

ZDI research includes a collaborative effort between astronomers in Australia, France and elsewhere. The Anglo-Australian Telescope (AAT) at Siding Spring Observatory is used to study active young solar-type stars in an ongoing effort to learn more about the early history of the Sun and its intense magnetic activity.

1.3.2 Photometry to determine rotation period

As the basis of ZDI is the detailed measurement of spectral line shapes and polarisations, it requires relatively large telescopes and sophisticated spectropolarimetry to be effective. ZDI is thus primarily the domain of large professional observatories rather than those operated by the majority of university departments and amateur astronomers.

On the other hand, the rotation period of stars studied using ZDI remains a key piece of information, and is unknown for many potential new targets. ZDI targets have

visual magnitudes ranging from about 6 to 12. Photometry is therefore a complementary activity associated with ZDI research that is well within the reach of smaller telescopes such as those at MKO and Moore. A large amount of telescope time at these sites can be dedicated to a single ZDI target, making these facilities ideal counterparts to the spectroscopy done for ZDI.

The MKO CDK20 has recently been employed for photometry in support of ZDI undertaken at the AAT at Siding Spring Observatory. Photometry results for the ZDI targets HIP71933 and HIP93378 are thus presented as part of this thesis.

1.3.3 Photometry and low-latitude star spots

In addition to providing rotation periods, photometry can help improve the Doppler imaging of star spots. Star spot photometry is generally useful for studying spot maculation effects for spots across a range of latitudes. While Doppler imaging remains sensitive to high latitude features, photometry is more sensitive to low latitude features, making the two techniques complimentary. Spectroscopic observations combined with simultaneous photometry data thus can improve the definition of low-latitude star spot features. In 2000, [Marsden](#) undertook a Doppler imaging study of R58, a G2 dwarf star in an open cluster designated IC 2602 in the constellation Carina (also known as the Theta Carinae Cluster or Southern Pleiades), where his results demonstrated that the photometric data could be used to enhance the low-latitude features of the star when compared to the spectroscopic data alone ([Figure 1.1](#)). The observed total spot coverage of the star incorporating photometry is $\sim 13\%$ while the observed coverage is $\sim 11\%$ when no photometry is included. In particular, the additional spot features detected are at lower latitudes and these features can be useful in determining the type of dynamo operating inside the star.

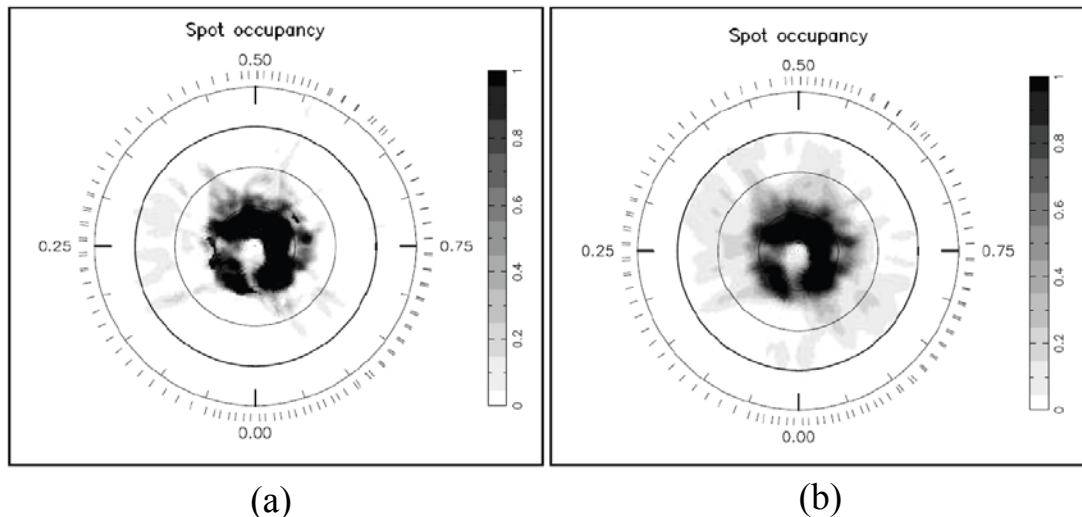


Figure 1.1 Maximum entropy brightness reconstruction for R58

R58 is a G2 dwarf in IC 2602. These plots are flattened polar projections looking down on the pole of the star. The bold lines denote the equator and the thin lines are $+30^\circ$ and $+60^\circ$ latitude. The radial ticks outside the plot indicate the phases at which the star was observed. Plot (a) shows the reconstruction using only the spectroscopic data while plot (b) shows the same reconstruction incorporating the photometry data. It can be seen that the overall structure of the surface features is retained but lower latitude features enhanced when the photometry data are included. ([Marsden 2002](#)).

1.4 Exoplanet detection techniques

Exoplanets are worlds which are in orbit around stars other than the Sun. They are generally difficult targets due to them being very faint and having very low mass. The visibility of an exoplanet relies on it reflecting light from its host star thus making its brightness some 20-30 magnitudes or 10^8 to 10^{12} times fainter than the host star ([Schultz 1999](#)). Further, such a planet has little gravitational influence on its host star making it difficult to detect by astrometric or radial velocity methods. Nevertheless, as of the time of writing, more than 400 exoplanets have been found mainly using the radial velocity method ([NASA PlanetQuest](#)).

The following methods are in use or are being trialled in the ongoing search for exoplanets:

1.4.1 Astrometric displacement

This technique relies on taking images of the host star and making measurements of its position over time. A periodic displacement in its position may indicate the presence of an exoplanet (or planets) orbiting the star. Due to the very small variations in the position of the host star caused by an exoplanet, this method has not been very successful until recently. In 2009 astronomers from NASA's Jet Propulsion Laboratory, Pasadena, California announced the astrometric discovery of a planet, VB10b orbiting the very small red dwarf star VB10 about 20 light years away in the constellation of Aquila ([NASA Mission News May 2009](#)). This discovery has not yet been confirmed by other exoplanet detection methods.

1.4.2 Pulsar timing

This technique uses a radio telescope to measure the small, regular variations in the timing of the radio pulses from a pulsar. Hence, this technique is only useful for detecting planetary-type bodies that may be orbiting pulsars.

1.4.3 Doppler spectroscopy

This technique is also known as the radial velocity or Doppler wobble method and involves the measurement of regular variations in the radial velocity of the host star. Measuring the radial velocity of a star by analysing the wavelength of its light has been more effective than attempting to measure the position of the star as in the astrometric displacement technique. Most of the exoplanets detected to date are due to Doppler spectroscopy.

1.4.3.1 Anglo-Australian Planet Search (AAPS)

The AAPS project is a successful southern hemisphere search for exoplanets. It started in January 1998 with the objective being to detect Jupiter-like planets in orbit around other stars using the 3.9m Anglo-Australian Telescope (AAT). The project monitors approximately 240 of the nearest and brightest Sun-like stars on 32 nights of

each year and performs these observations using the University College London Echelle Spectrograph (UCLES), enabling observations of the radial velocity of large numbers of spectral lines across the visible spectrum.

The small gravitational influence of a planet on its host star causes the star to wobble with its velocity varying periodically with respect to Earth. This enables detection of an exoplanet by the reflex motion of its parent star, which produces measurable Doppler shifts in the stellar spectrum. The velocity changes depend on the distance at which the planet orbits, the mass of the planet and the orbital eccentricity. For typical gas-giant planets, the Doppler velocity variations are in the range 1 to 100 m/s ([Anglo-Australian Planet Search](#)).

[Vogt et al. \(2009\)](#) outlines precision radial velocity data that reveal the presence of at least three planets orbiting the bright nearby G5V star 61 Virginis, with one of the planets apparently being the first example of a terrestrial planet orbiting a Sun-like star. This research was based on 4.6 years of combined Keck/HIRES observations and AAT precision radial velocity measurements.

1.4.4 Transit photometry

This technique relies on the measurement of small, regular variations in the apparent brightness of the host star caused by the passage of a planet between Earth and the stellar disk ([Figure 1.2](#)).

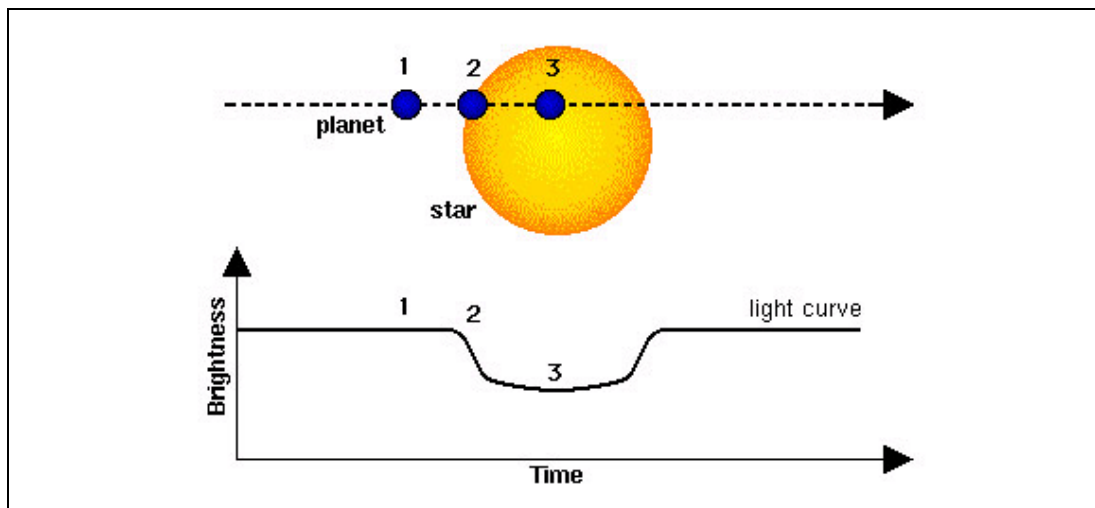


Figure 1.2 Simulated transit event and light curve

As an exoplanet transits its host star, a small reduction in brightness is observed. The region of the light curve where the planet first crosses the edge of the star (2) is referred to as the ingress, while the region where the planet crosses the opposite side of the stellar disk is called the egress. (Image from <http://www.portalciencia.net/images/corot2.jpg>).

A limitation of this technique is that the planet's orbit must be inclined such that the planet passes between the host star and Earth, however a major advantage of this technique is its accessibility. With this method, it is preferable to observe multiple

transits to confirm that they are due to orbital motion and not some other phenomenon such as star spots. Another advantage of this technique is that the timing and relative dimming of the host star allow the size of the exoplanet to be determined.

In principle, small telescopes such as the USQ and UoL CDK20's can be used to detect exoplanet transits. Based on existing results however, millimagnitude photometry is desirable, highlighting the need for attention to detail regarding observational techniques and data analysis. ([Exoplanet Transit Database](#), [Transitsearch.org](#) candidate page).

Transit searches are currently proving to be the second most successful technique after Doppler spectroscopy, and the list of observed transiting planets continues to grow, thanks to both ground-based work and the advent of the CoRoT and Kepler missions ([NASA PlanetQuest](#)). [Transitsearch.org](#) and the [Exoplanet Transit Database](#) provide online catalogues of known exoplanet transits and have been used to find suitable targets for this thesis.

1.4.4.1 Intrinsic stellar activity & exoplanet effects

Exoplanet transit work is closely related to the study of star spots. For example, TrES-1 is an exoplanet 512 light-years away orbiting GSC02652-01324 in the constellation of Lyra. It was discovered in 2004 by the Trans-Atlantic Exoplanet Survey (TrES) by detecting the transit of the planet across its parent star. In 2005, the Hubble Space Telescope (HST) observed numerous transits of TrES-1 and discovered a flux increase during one transit which was clearly a feature coming from the TrES-1 system itself ([Figure 1.3](#)).

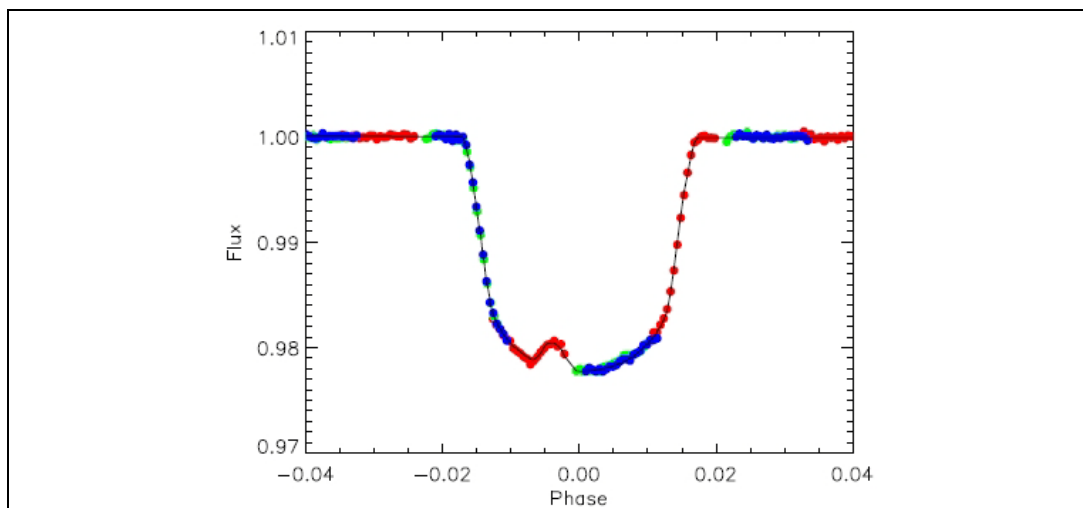


Figure 1.3 TrES-1 phased light curve from HST observations

The red, green and blue data correspond to different observing days. A flux increase can be seen in the red transit light curve data captured on 19 November 2004 ([Rabus et al.](#)).

[Rabus et al. \(2009\)](#) analysed this event in detail to ascertain if the flux increase was due to a star spot on the host star or a second transiting planet. The feature has a depth of 2.7 mmag whereas the standard deviation of the transit is 0.18 mmag and therefore the presence of the feature could not be attributed to noise. Rabus et al. concluded that

the flux-rise feature is likely a star spot on the host star but could not rule out the possibility that the feature was caused by an additional transiting planet. The true nature of the feature will require demonstration of a wavelength-dependency for the flux-rise or alternatively detection of an additional planet by either transit or radial velocity methods.

1.4.4.2 Rossiter McLaughlin effect

When a transiting exoplanet blocks part of the surface of its host star as seen from Earth, the apparent radial velocity of the host star is altered. When the exoplanet is out of transit, the rotating host star has a constant radial velocity because the blue shifted approaching and red shifted receding parts of the star's surface contribute equally and cancel each other out (Figure 1.4). When an exoplanet transits its host star, it blocks part of the star's surface, causing an anomalous net Doppler shift which changes the star's radial velocity in a predictable manner. This is known as the Rossiter McLaughlin (RM) effect. Ohta et al. (2005) reported that the signature of the RM effect was first reported by Schlesinger (1910) and later isolated and measured by Rossiter (1924) and McLaughlin (1924). This effect has been observed for exoplanets such as TrES-1 (Narita et al. 2007).

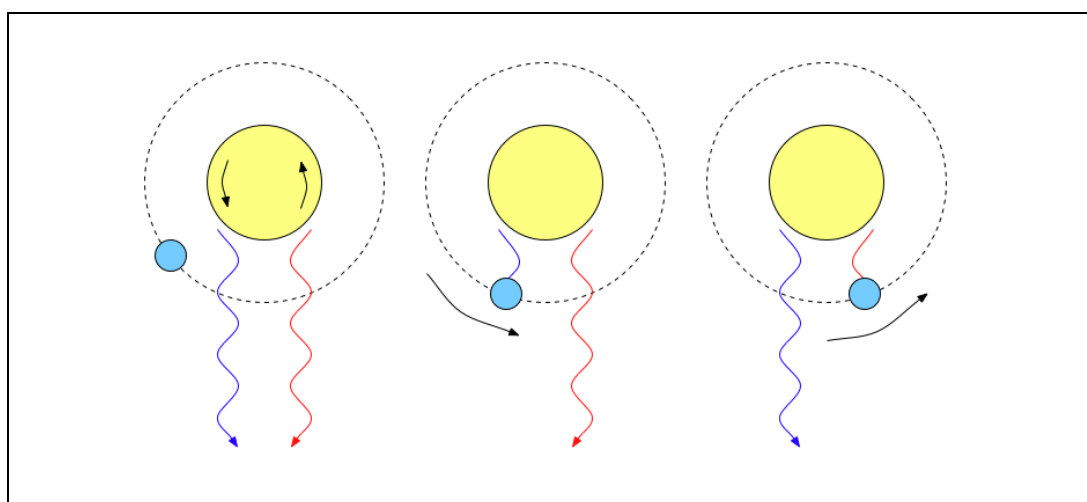


Figure 1.4 The Rossiter-McLaughlin Effect

Left Frame: Light from the anticlockwise-rotating star is blue-shifted on the approaching side, and red-shifted on the receding side as seen by an external observer situated at the bottom. Middle Frame: As the planet (blue) transits the star it blocks a fraction of light that is being blue-shifted by the rotating star. Right Frame: During the egress of the transit, the planet blocks a fraction of red-shifted light from the star. (Image from http://en.wikipedia.org/wiki/Image:Rossiter-McLaughlin_effect.png).

1.4.4.3 Transit survey

Transit surveys provide a way of detecting exoplanets including the confirmation of planets already discovered by radial velocity surveys such as the AAPS. In some cases, such as HD209458b, a planet can be observed both using radial velocity and transit methods.

In March 2009, NASA mission Kepler was launched to scan a large number of stars in the constellation Cygnus with a differential photometric precision of 20 parts per million for 12th magnitude solar-like stars over a 6.5-hour integration time and is expected to detect and characterise Earth-sized planets ([NASA Kepler Mission](#)). The NASA Kepler Mission uses the transit method to scan a hundred thousand stars for planets. In January 2010, the Kepler Mission announced that it had found its first five exoplanets. The new exoplanets range in size from similar to Neptune to larger than Jupiter and have orbits ranging from 3.3 to 4.9 days.

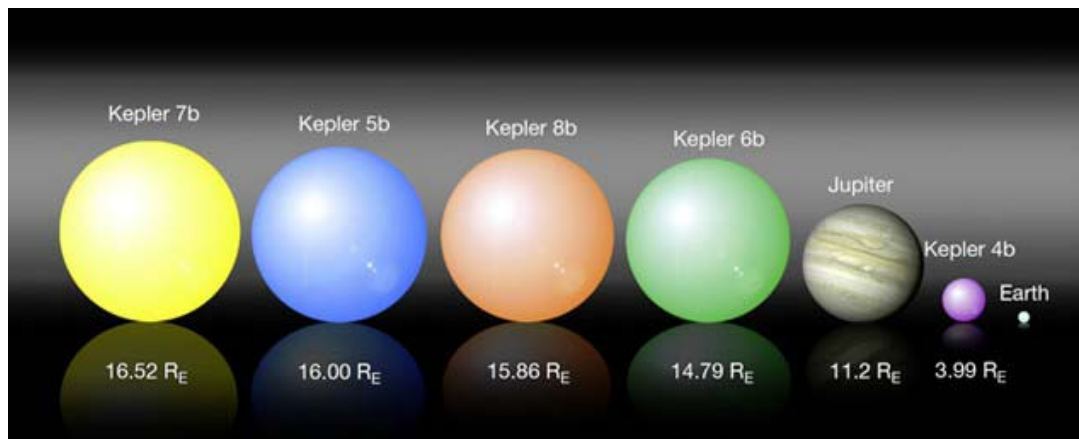


Figure 1.5 Kepler's first five exoplanet discoveries

Kepler is capable of detecting exoplanets the size of Earth. This figure shows the relative planet size of Kepler's first five planet discoveries as compared with Jupiter and Earth in our own solar system. Image from <http://kepler.nasa.gov/>.

1.4.4.4 Transit plus radial velocity observations

A limitation of the Doppler detection method is that the radial velocity detected (i.e. the line of sight velocity with respect to Earth) only provides $m \sin i$ (the mass of the planet times the sine of the angle of inclination of the planet to the line of sight to the observer) as opposed to actual mass. Another limitation of this detection method is that the Doppler shifts cannot be accurately measured for all stars i.e. for those stars with a rotation axis that is close to our line of sight. If an exoplanet can be detected using both the radial velocity and transit methods then the minimum mass of the planet can be found from the radial velocity method and the radius of the planet and the orbital inclination from the transit method. Together, these methods indicate the mass and density of the planet.

1.4.5 Gravitational microlensing

This technique makes use of the lens effect foreground stars have on the light from background objects. When a foreground star passes between Earth and a distant star, its gravity causes the light from the distant star to bend which is seen as an apparent brightening of the distant star. Any planets orbiting the foreground star cause anomalies in the lensing event light curve enabling their detection. This detection method has the advantage of being very sensitive as microlensing can produce high magnification for suitable star-planet-Earth alignments e.g. ([Bond et al. 2004](#)).

Examples of microlensing studies of planets include MACHO, OGLE, MOA and PLANET ([Wikipedia, Gravitational Microlensing](#)).

[Figure 1.6](#) shows the microlensing light curve of OGLE-2005-BLG-390Lb, one of the smallest exoplanets discovered at $\sim 5.5 M_{\text{Earth}}$. Six planets have been detected to date using this technique including OGLE-2005-BLG-390Lb ([Beaulieu et al. 2006](#)). The presence of the exoplanet causes a deviation in the otherwise “Bell-shaped” light curve of the host star OGLE-2005-BLG-390L. The first discovery using this technique was of OGLE 2003-BLG-235 in 2003 ([Bond et al. 2004](#)).

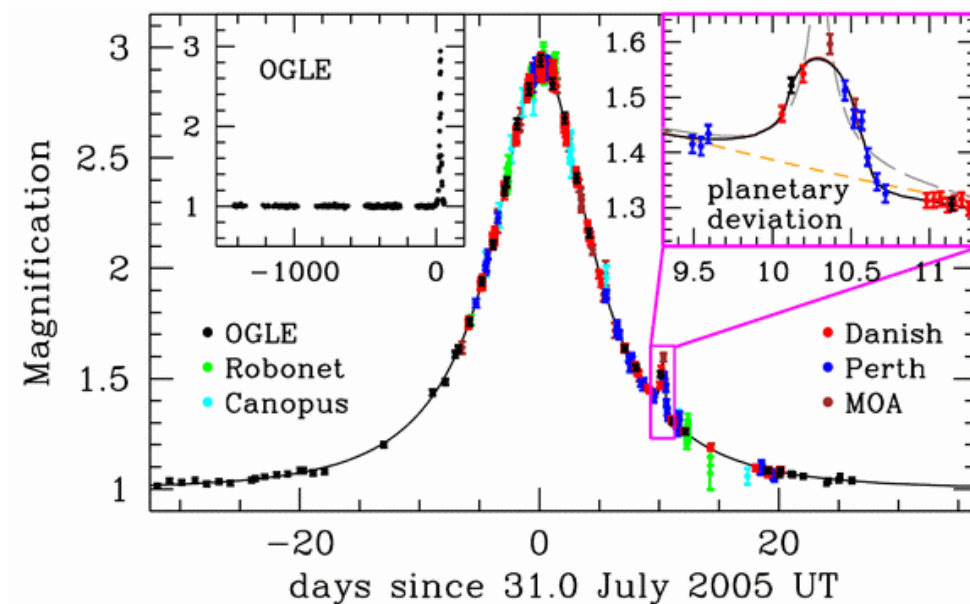


Figure 1.6 Microlensing light curve of OGLE-2005-BLG-390L b

The top right inset shows a zoom of the planetary deviation, covering a time interval of 1.5 days. (image from: <http://www.perthobservatory.wa.gov.au/research/planet-discovery.html>)

1.4.5.1 Targets of opportunity

Microlensing events in which an anomalous light curve is detected are rare and difficult to follow up on because the other exoplanet detection methods are generally ineffective in detecting such planets. The microlensing event itself is a target of opportunity relying on a fortuitous alignment of the lensing star (i.e. the star hosting a planet) and a background star. Such events may not occur again for any given host star for potentially hundreds of years making the follow-up observations and confirmation very difficult.

1.4.5.2 MicroFUN

The microlensing follow-up network known as MicroFun is an Ohio State University organised informal consortium of observers monitoring microlensing events in the galactic bulge with the primary scientific objective being the detection of exoplanets that may be orbiting lensing stars ([The Ohio State University MicroLensing Follow-Up Network](#)).

The MicroFUN members receive alerts when a microlensing event has been detected so that they may then focus their telescopes on the lensing event in order to record as much photometric data as possible. Most often, these alerts are received with very short notice and so the follow-up work is best performed with small telescopes able to be rapidly deployed and used to observe the microlensing event. Large telescopes are able to provide high accuracy photometry, however due to their strictly managed operating schedules they cannot be relied upon for short notice microlensing follow-up work. MicroFUN is a good example of the type of scientific consortium that MKO could join should it prove capable of precision photometric observations.

1.5 Digital Science Partnership

The Digital Science Partnership (DSP) is an initiative of the UoL and Northern Kentucky University that is funded by the United States National Aeronautics and Space Administration (NASA) to deliver live remote observing for astronomical education, research and outreach ([Carter et al. 2007](#)).

The Southern Skies Program is an extension of the DSP to the southern hemisphere, through a collaboration between the UoL and the USQ. The collaboration involves the implementation of two essentially identical telescopes, one at Mount Kent Observatory in Queensland Australia and the other at Moore Observatory in Kentucky USA. With the advent of access to Moore Observatory and the northern sky, the program has been extended and is now referred to as the [Shared Skies Partnership](#).

A key feature of the Shared Skies Partnership is its emphasis on developing open-source general-purpose robotic observing systems for education, research and outreach, and the use of mass-market telescope and camera hardware where practical. It is also focused on web-based delivery of imaging and data analysis, and shares its developed software so that others can emulate what is being achieved at other sites. The Shared Skies Partnership differs from other educational projects such as [Hands-on Universe](#) and [Las Cumbres Observatory Global Telescope Network](#) because it is designed to specifically support and complement the university studies of students at USQ and the UoL at both undergraduate and postgraduate levels, as well as supporting schools. All the same, it supports the academic approach of two universities engaged in distance education in astronomy which is inline with USQ's mission, strategy and goal to provide quality professional education opportunities that are accessible, flexible and borderless ([USQ Strategy](#)). As such, it aims to fill a gap between commercial robotic telescope systems such as [ROBOsky](#) and [SLOOH](#) for amateur astronomers and sophisticated robotic observatories dedicated to specific research projects such as the [Automated Astronomy Group](#) for stellar photometry, the [Pan-STARRS](#) project for asteroid surveys and the [SkyMapper](#) project for photometry and imaging.

1.5.1 Science education through research

The DSP fosters science education through research. Both the USQ and UoL offer research astronomy courses that provide students with access to researchers in their field of study, or related to their field of study. The complementary nature of ZDI spectropolarimetry and photometry is one example of how the MKO facility can directly and fruitfully contribute to professional research.

1.5.2 The teaching-research nexus

The teaching-research nexus offers benefits in incorporating research into education. For example, Associate Professor Gabrielle Baldwin of the Centre for the Study of Higher Education developed a teaching-research nexus for the University of Melbourne that provides a good example of how it can be successfully implemented (Baldwin 2005). The document outlines the benefits of incorporating an academic's research into the classroom teaching thus enriching the teaching experience for the students, and potentially assisting the academic in their field of study, through questions and fresh ideas from students not previously exposed to the specifics of research.

In the context of astronomy and the DSP, USQ and UoL have recognised and embraced the teaching-research nexus, by aiming to provide student involvement in studies relating to research being undertaken by academic staff. This interaction can help provide students with current disciplinary knowledge, and increase their interest in the subject through the teacher's/researcher's passion for his or her field of research. Students are thus able to relate in a meaningful way to university research, whilst at the same time achieving the learning outcomes of different courses.

1.5.3 Astronomy, science & technology

Astronomy is an ancient and diverse scientific discipline that therefore provides students with many alternative study options. Another aspect of astronomy is the high reliance on technology to undertake research. This is particularly true of observational astronomy where a student is typically exposed to complex computer systems, computer networks, radio communication links, mechanically complex telescopes, scientific grade CCD cameras, and control systems. All of this technology is required for even the most basic observational research endeavours. This aspect makes astronomy an ideal platform from which to teach science and technology together, and provide students with challenging goals requiring them to learn a range of new skills.

1.5.4 MKO astronomical distance education

USQ is a provider of on-campus and distance education programs with some three quarters of its students studying externally. USQ's forte is in the delivery of resources and technology enabling effective distance education.

This focus on distance education is one of the major driving forces behind current efforts to make the MKO CDK20 a fully robotic telescope. Students studying off-campus will be able utilise the telescope from their PC whatever their location in the world. This provides benefits to the university by way of attracting students due to the leading edge facilities and also provides benefits to the students by not having to travel significant distances to engage in observational activities.

1.5.5 Student observing

Traditional astronomical observing involves the researcher or student travelling to the location of the telescope, typically for many days at a time, to make the planned observations. This process can be arduous and requires steadfast dedication on the part of the researcher/student. The remote location of the telescope usually means that all other aspects of life go on hold for the duration of the observing run. A significant factor influencing the outcome of such an expedition is the weather, or more specifically, the unpredictability of the weather. Despite obtaining up to the minute forecasts, the availability of clear sky is never guaranteed compounding the issues already faced by the observer.

The difficulties of observing are heightened for a student that does not have ready access to an observatory. USQ, the UoL and a number of other universities around the world have recognised the impost placed on distance education students attempting to undertake observational astronomy activities. To address the issue, USQ and UoL have embarked on a program to make the CDK20 telescopes at their respective facilities fully robotic, so that distance education students can readily acquire useful astronomical data.

1.5.6 Robotic observing

Under the DSP, USQ and UoL intend to make the CDK20 telescopes at MKO and Moore Observatory into fully robotic telescopes. A robotic telescope is one that can operate autonomously, without human intervention, however the term “robotic telescope” is somewhat broad because there are a number of variations that can all be considered robotic. The most basic robotic telescope is one in which the telescope and its associated peripherals are controlled by a local computer. In this case the user is able to make observations by entering requests into the controlling computer.

The next level up from this basic robotic model involves a communications link to enable remote access by the user to the controlling computer. In practice, a user located anywhere in the world would define a target and submit the request to the robotic telescope system along with other information describing the type of observation and any limitations the user may impose. The robotic telescope would then schedule and subsequently perform the required observing and send advice to the user when completed.

Building on this concept is a robotic telescope in which the raw observations are not only captured but also processed in some meaningful way. Photometric analysis of a

specified target is one such example. This is the type of robot most suited for research and educational astronomy and is the type being implemented at MKO by USQ.

1.5.7 Data processing in astronomy

Given the vast quantities of astronomical data being acquired by telescopes around the world, students now have access to a wealth of data that is able to be explored for a range of projects. However, sorting through large quantities of data is unlikely to provide the level of engagement or interest for a student that can be offered when the student is involved at some level in the astronomical observation. Further, undertaking specific astronomical observations for one's own research may be the only way to gather the necessary quantity and quality of data.

1.5.8 DSP and remote live observing

The DSP was motivated by an aim to make it possible for students to remotely acquire their own data for a number of projects and being able to access the northern or southern skies as required. Under certain circumstances, live remote observing during the observer's local daylight can be provided by utilising the longitude difference between telescope and observer.

1.5.9 Hybrid robotic system

The facility at MKO continues to be developed with the aim to provide a mixture of observing experiences. In addition to traditional observing using a local telescope, the observatory currently offers a small imaging robotic telescope known as the O'Mara telescope, and is implementing a development project to make the CDK20 telescope into a robotic instrument for precision photometric monitoring. Further, a 0.7m CDK700 robotic telescope will be installed at MKO in late 2010, offering an additional capability for precision photometry for education and research.

1.5.10 Stellar photometry for the Shared Skies Partnership

This thesis is aimed at validating the hypothesis that the CDK20's and RC24 telescopes at MKO and Moore can deliver the required photometric precision for supporting ZDI and exoplanet transit research by university academics and their students. As such, the work involves a detailed photometric analysis of standard stars, spotted stars and exoplanet transit observations. This thesis covers the methodology and results of such an analysis, and presents its findings in a concluding chapter.

This page is intentionally blank.

Chapter 2: Facilities & Methods

2.1 Mt Kent Observatory

2.1.1 Site

Mt Kent Observatory is a USQ facility dedicated to astronomy teaching, research and outreach. The Observatory is located at a dark-sky site in Cambooya Shire, about 30 minutes drive south-west of the University's Toowoomba campus in Queensland, Australia (151° 51' 19.5"E -27° 47' 52.3"S). At 682m above mean sea level on the Great Dividing Range in a pastoral area of the Darling Downs, it offers frequent clear skies, good seeing (around 1.5 arcseconds) and established secure infrastructure (Carter et al. 2007). The site includes a utility building known as the "Educational Development Group" (EDG) building and there are 3 telescopes situated onsite in separate domes (section 2.1.3).

2.1.2 Educational Development Group building

The EDG building (Figure 2.1) at MKO provides a lecture room, accommodation facilities and a control room for indoor operation of the observatory telescopes. A weather station is located on the Observatory grounds and a high speed data link connects the site to the university campus.



Figure 2.1 EDG Building at Mt Kent Observatory

This building provides onsite accommodation for visiting researchers and students and includes a lecture room, computer/server/comms room, control room, and storage facilities.

2.1.3 MKO telescopes

2.1.3.1 Webb telescope

The Webb telescope is a 40cm aperture, f/10 (i.e. the focal length is 10 times the aperture diameter), Meade Instruments computer-controlled LX200 Schmidt-Cassegrain telescope with a fibreglass dome. The instrument is used visually for student and amateur viewing nights but is scheduled to be decommissioned later in 2010 to make way for the new CDK700 0.7m robotic telescope designed and manufactured by [PlaneWave Instruments](#).

In the past, the Webb telescope has been used for stellar photometry, the results of which have been published in scientific papers. Of particular note is the work undertaken by [Budding et al. \(2001\)](#) in which optical photometry was performed for the active Algol Binary KZ Pavonis.

2.1.3.2 O'Mara telescope

This telescope is owned by USQ and managed by Automated Patrol Telescopes Australia Pty Ltd (APTA). It is installed in its own dome at MKO and comprises a Software Bisque Paramount METM robotic mount equipped with a Meade 30cm aperture telescope with Schmidt-Cassegrain optics and a SBIG STL-1301 camera. Users are able to submit requests via a webpage maintained by APTA. This telescope was not considered for this thesis as explained in section [4.7](#).

2.1.3.3 University of Louisville telescopes at MKO

A 50cm/20inch Corrected Dall-Kirkham telescope known as CDK20s and its associated cameras have been installed at MKO as part of Southern Skies Project of the DSP. This allows students in Louisville, USA to control the telescope and see the southern night sky during their day. The telescope is also used for scientific research conducted by postgraduate students at USQ. Section [2.3.1](#) provides specific information about the telescope.

2.1.4 CCD camera

An SBIG model STL6303 camera is installed on the CDK20s delivering a 18.34'×27.51' field of view with 9 micron square pixels. A UBVRI (Ultraviolet, Blue, Visual, Red, Infrared) filter wheel is installed for photometry and general imaging, but is interchangeable with a LRBGC (Luminance, Red, Blue, Green, Clear) filter set if photorealistic colour imaging is required. A SBIG STV astronomical television camera with eFinder optics (2.7°×2.0°, 7.4 micron pixels) is used for target acquisition, and a Nikon Digital Single Lens Reflex (DSLR) (15.8°× 10.6°, 15 arcsecond pixels, f= 85mm lens) is used as a wide-field one colour piggyback camera ([Carter et al. 2007](#)).

2.1.5 Dome

The CDK20s telescope is housed in a Sirius Observatories™ 3.5m diameter fibreglass dome (Figure 2.2) equipped with a dome control system developed especially for the Southern Skies Project. The dome is installed on a site formerly used for the Arthur Page Telescope¹. The dome rotation is encoded with radio frequency identification tags for absolute azimuth readout.



Figure 2.2 Mount Kent Observatory

The dome housing the MKO CDK20 telescope is a Sirius Observatories 3.5m diameter fibreglass dome. Image from http://www.astro.louisville.edu/mkent/page_dome/index.html.

2.1.6 Communications

MKO is connected to the USQ Toowoomba campus by a 34 Mbit/s microwave link (Figure 2.3) then to Brisbane via fibre. A connection from Brisbane to Louisville, USA is provided via the internet (Kielkopf et al. 2006). This communications infrastructure allows robust and reliable remote operation and data transfer and has enough bandwidth to support real-time video and audio with an acceptable latency when dome video is being transmitted using an Axis 241 video server and video conferencing through a Polycom VSX 7000. The video conferencing system links MKO with the UoL's Gheens Science Hall and Rauch Planetarium.

1. Arthur Page donated his telescope for use at MKO from 1996 onwards. Eventually, this telescope fell into disuse, however when the UoL provided funding for a new telescope on the site, the dome housing the new telescope was named in honour of Arthur Page to recognise his contribution.



Figure 2.3 MKO Microwave data link

The MKO microwave link tower is seen in this image behind the EDG building. It provides a 34 Mbit/s microwave link to the USQ Toowoomba campus.

2.1.7 Additional instrumentation

A Davis Vantage ProTM Weather Station monitors site rainfall, wind, temperature and humidity, and a Boltwood Cloud Sensor is installed as a further check on conditions.

Electronic site security includes a remotely operable external security camera used for monitoring the site. On a fixed wall inside the dome, an additional remotely operable security camera with low-light capability is installed to allow remote observation of telescope and dome motion.

2.2 Moore Observatory

2.2.1 Site

Moore Observatory is located on the 200-acre Horner Wildlife Refuge in Oldham County, Kentucky, USA. The observatory is named for Walter Lee Moore, Professor of Mathematics at UoL from 1929 to 1967. It is a research and advanced teaching facility for graduate and undergraduate research at the UoL. Located at 85° 31' 43.4"W, 38° 20' 41.2"N and 230m above mean sea level, the observatory is a typical light-polluted midwestern site, however it is readily accessible by students on short notice ([Kielkopf et al. 2006](#)).

2.2.2 Main Building

This building performs the same function as the EDG building at MKO by providing a lecture room, accommodation facilities and a control room for indoor operation of the observatory telescopes.



Figure 2.4 Moore Observatory main building

Image from <http://mtkent1.mko.usq.edu.au/moore/history/histmoore.html>.

2.2.3 Moore Observatory telescopes

2.2.3.1 Ritchey Chrétien telescope

This 60cm/24-inch telescope from RC Optical Systems is a research grade instrument used by university academic staff and postgraduate students primarily involved in studies of the optical properties of the atmosphere in the near infrared, and the development of imaging and spectroscopic technology. The instrument features a robust fork mounting with an absolute Renishaw precision encoder on the polar axis. A Wide Field Spectral Imager is also used for research work on the dust content of galactic nebulae, and occasionally for bright comet spectroscopy (Kielkopf et al. 1998, Moore Observatory). This telescope has been used to observe exoplanet WASP12b for this thesis, enabling a comparative analysis between its performance and that of the smaller aperture CDK20 telescope (refer to section 3.7).

2.2.3.2 Corrected Dall-Kirkham telescope (CDK20n)

This telescope is identical to the one installed at MKO and is primarily used for education, public astronomy outreach, and target of opportunity research. It is referred to as the CDK20n. Refer to section 2.3.1 for details.

2.2.3.3 Schmidt-Cassegrain

This 40cm/16-inch telescope is available for hands-on CCD imaging and photometry by interested students, trained visitors, and guests.

2.2.4 CCD cameras

The CCD camera installed on the CDK20 at Moore Observatory is the SBIG model STL6303. This is the same model as installed at MKO (Refer to section 2.1.4). The RC24 telescope is fitted with an Apogee U9000 3056x3056 12.5 micron pixel CCD with a field of approximately 26 arcminutes.

2.2.5 Dome

A Sirius Observatories dome houses the CDK20 telescope and was installed in January 2006. The dome shutter motor is solar powered and operated remotely through a radio frequency controller avoiding the need to maintain electrical contacts to the rotating dome. Dome rotation is encoded by radio frequency identification tags attached to the drive gear on the inside of the dome.



Figure 2.5 Moore Observatory remote/robotic telescope dome

Trees to the west of the dome at Moore Observatory partially block the view of the bright western sky toward Louisville, and provide some shade in the late afternoon to reduce daytime heating inside the dome. Image from <http://www.astro.louisville.edu/moore/cdk20/dome/index.html>.

2.2.6 Communications

Moore Observatory is connected by a T1 1.5 Mbit/s link to the main campus network. This link is able to support real-time compressed image transfer and video conferencing while running remote control and data acquisition software.

2.2.7 Additional instrumentation

Instrumentation available for remote operation of the telescopes is listed on the [Moore Observatory Remote/Robotic Telescope](#) website.

2.3 Common equipment

Identical telescopes, computer hardware and software have been installed at both MKO and Moore Observatory.

2.3.1 Corrected Dall-Kirkham telescope

The CDK20 telescope is a PlaneWave Instruments Corrected Dall-Kirkham 50cm/20inch aperture, f/6.8 telescope. The telescope mount is a prototype Celestron computer-controlled German equatorial mount that runs on the NexStar control system. It features a temperature-stabilized optical system using a light weight conical Pyrex ellipsoidal primary and a spherical secondary, multilayer coated for 98% reflectivity in the visible band. This optical design provides a wide flat field for imaging with large format CCDs (Carter et al. 2007). The focuser on this telescope has a motor driven encoded screw drive and is exceptionally stable, typically maintaining good focus night after night. The focal scale of 59.7 arcseconds per millimeter provides a 27.5 x 18.3 arcminute field of view with the SBIG STL6303 camera that is its primary detector (section 2.1.4) (Kielkopf et al. 2006). It tracks with 5" accuracy without error correction, and sub-arcsecond accuracy with automated guiding. Pointing accuracy with a low-order telescope pointing model correction is sufficient to place a target near the centre of a CCD field of view.

The telescope is autoguided by an SBIG STV guider using a short focal length auxiliary lens. Drift scan or time delay integration (TDI) imaging is under development for long exposure robotic operation. For remote operation, TDI offers long exposures without the need to guide, and the data rate, typically 30 CCD lines per second, is compatible with slower networks while offering an image for educational use that pans the sky continuously.

The CDK20 was installed at MKO in 2006 as part of Southern Skies Project. A twin telescope has been installed at the Moore Observatory in Louisville (section 2.2.3.2).

2.3.2 Computer hardware

Dual redundant 0.5TB IBM x346 servers running Suse Linux operate at MKO and Moore Observatory to buffer and archive the data flow.

2.3.2.1 INDI Servers

A server known as the INDI Server resides in the CDK20 dome at each observatory to provide the necessary interface between the outside world and the onsite hardware. At each site, the INDI Server hardware runs the Instrument Neutral Device Interface (INDI) protocol designed to support control, automation, data acquisition, and exchange among hardware devices and software front ends with particular focus on astronomical instrumentation (INDI).

The INDI server at each Observatory sits between the physical devices onsite and the users, known as INDI clients. INDI clients are the software front ends that communicate with the hardware drivers.

2.3.3 Computer software

The user is able to control the telescope and its associated accessories using a single controlling computer. Professor John Kielkopf from the UoL has developed a series of open source Linux applications that provide graphical user interfaces to the telescope mount, dome, guider and camera. These applications are essentially INDI clients providing an interface between the human user and the INDI Server. They operate in parallel with other INDI clients such as XEphem. The following paragraphs outline the individual applications used at MKO and Moore Observatory. The content has been derived from information on the [Southern Skies Digital Science Partnership](#) website.

2.3.3.1 XmCCD

The XmCCD software creates FITS image files with comprehensive header information and displays the images using SAOImage ds9. Images may be processed for dark subtraction and flat fielding with the FITS file utilities that are included. ([Figure 2.6](#)).

2.3.3.2 XmGuider

The XmGuider software uses the SBIG SG-4 autoguider for automatic guiding of remotely controlled and robotic telescopes without operator intervention. This software implements most, but not all, control options provided through the serial interface: setting exposure time, taking dark frames, calibrating guider response, and toggling autonomous operation on or off. Image display is with SAOImage ds9, which is started automatically when XmGuider is started. This is useful for focusing, but is not needed for the autoguiding feature. Scripted and command line operation through the INDI client are supported.

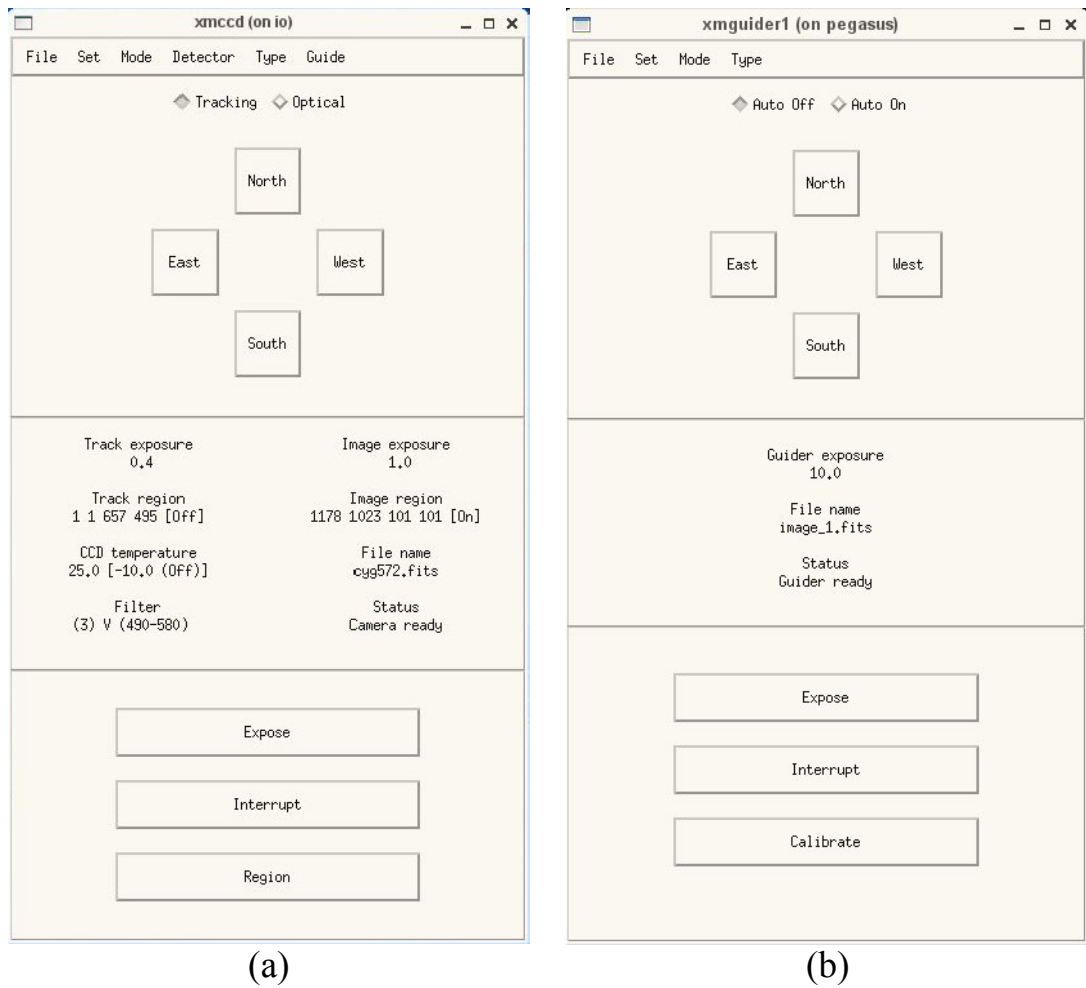


Figure 2.6 XmCCD & XmGuider screen shots

(a) *XmCCD* screen shot. Image from <http://www.astro.louisville.edu/software/xmccd/>. (b) *XmGuider* screen shot. Image from <http://www.astro.louisville.edu/software/xmguider/index.html>.

2.3.3.3 XmTel

XmTel software controls various telescope mounts via the INDI Server. It is compatible with Clear Sky Institute's XEphem. (Figure 2.7).

2.3.3.4 XmDome

XmDome provides a convenient graphical user interface for local or remote operation of an astronomical telescope dome. Whilst the application is specific to the hardware used for the Shared Skies Partnership at MKO and Moore Observatory, XmDome may be readily adapted to other hardware. It includes code to calculate the requisite

dome azimuth given the celestial coordinates of the telescope, for German equatorial, fork equatorial, and alt-azimuth telescope mounts.

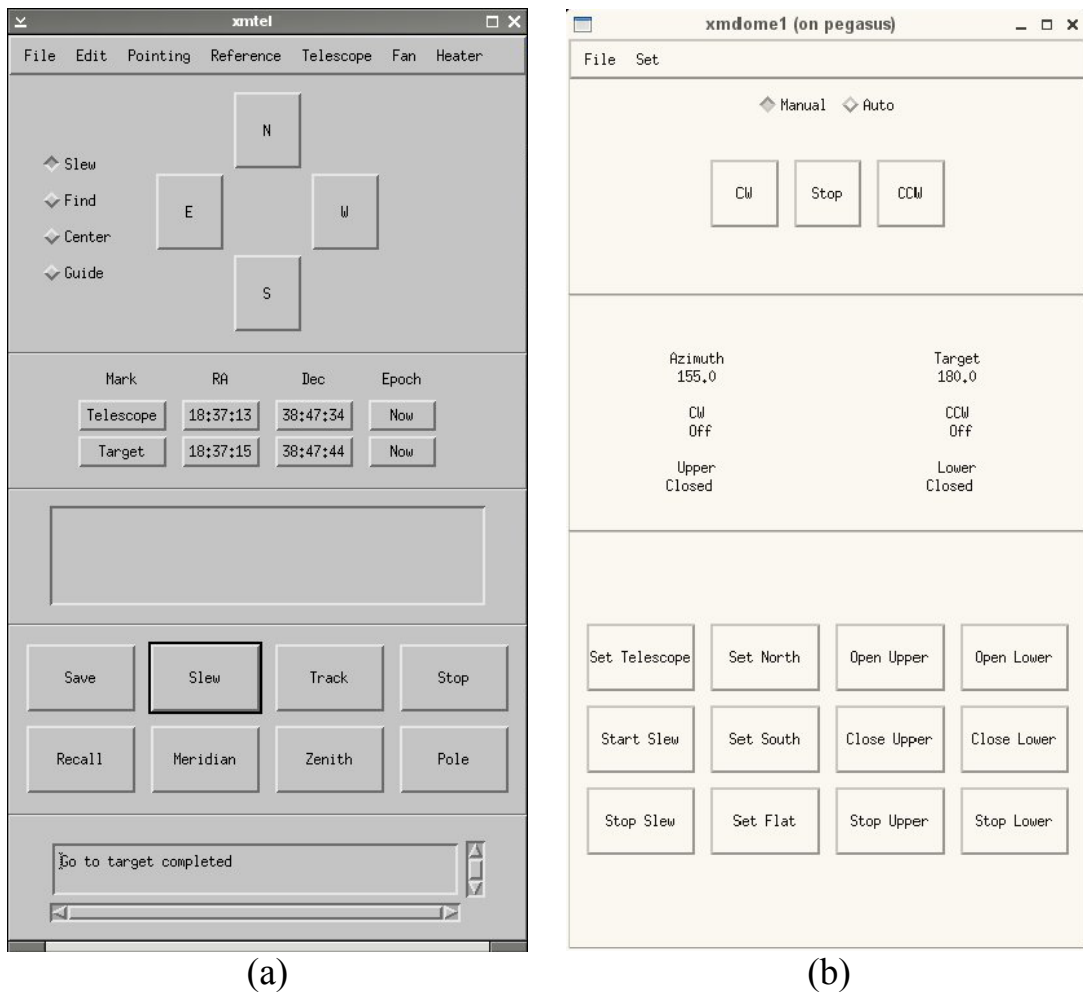


Figure 2.7 XmTel & Xmdome screen shots

(a) XmTel screen shot. Image from <http://www.astro.louisville.edu/software/xmtel/index.html>. (b) Xmdome screen shot. Image from <http://www.astro.louisville.edu/software/xmdome/index.html>.

2.3.3.5 XEphem

XEphem is a scientific-grade interactive astronomical ephemeris package. It is installed at MKO and Moore Observatory and provides a graphical interface between the user and the INDI Server. XEphem operates in parallel with the UoL applications mentioned in section 2.3.3.

XEphem can display data in configurable tabular formats in conjunction with several interactive graphical views and provides an observing logbook which is automatically filled in with observing circumstances, with a search capability on most fields. Numerous other functions are provided and can be reviewed on the [Clearskyinstitute](http://www.clearky.com) website.

Figure 2.8 shows some screen shots from the XEphem application.

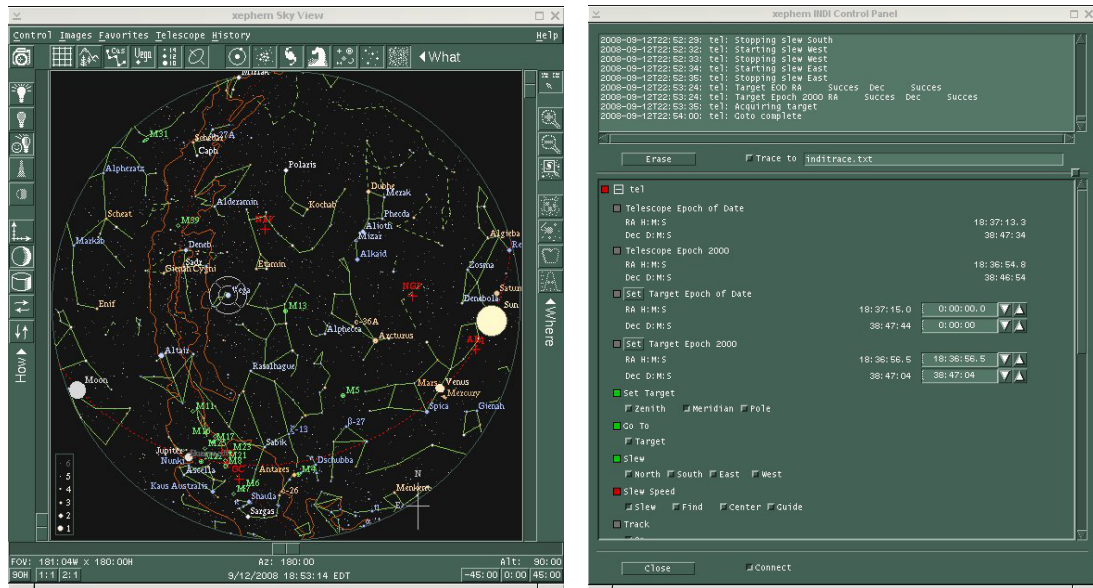


Figure 2.8 XEphem screen shots

Image from <http://www.astro.louisville.edu/software/xmtel/index.html>

2.4 Remote observing

2.4.1 Differences with traditional observing

Section 1.5.5 described the traditional observing practice whereby a user would physically visit an observatory to undertake their specific astronomical observations. Remote observing differs from the traditional method by extending the controls of the telescope to a location remote from the observatory.

This thesis makes use of the robotic telescopes at MKO and Moore Observatory to demonstrate their utility for stellar photometry in support of star spot and exoplanet research. Observational issues related to remote access to these telescopes are described in more detail in the subsequent paragraphs. These issues are expected to be common to any remote telescope and so should be considered in order to create a useable and efficient robotic telescope.

2.4.2 Internet

The use of the internet is a fundamental element in many robotic telescopes. The typical usage is to transport data to and from the telescope for the remote location. The internet is an ideal communications platform on which to design a robotic telescope due to its wide spread coverage, speed, accessibility and low cost.

The MKO and Moore Observatories make extensive use of the internet to provide communications for the control of the telescope, downloading of the raw observations and to provide digital voice and video services as required.

2.4.3 Data transfer

An important aspect of the internet, or more broadly the communications element of a robotic telescope, is the amount of data required to be transported and the bandwidth required to deliver that data within a reasonable time period.

A typical observing session involves using the telescope to take rapid cadence images of the target/s from astronomical dusk to astronomical dawn. As an example, the robotic telescope may be programmed to take 10 second exposures through many different filters on a continuous basis resulting in a single image approximately every 30 seconds. Hundreds of images may be taken over a typical observing session potentially requiring up to ~6GB of storage when using the CDK20 telescopes (image size ~12MB) or ~16GB of storage when using the RC24 (image size ~32MB). Clearly, a fast, high capacity internet connection is required to allow download of these data. In addition to the raw astronomical data, other services such as voice and video feeds also significantly contribute to the total data exchange for any given session.

An alternative to downloading large amounts of data is to store the data locally on the robotic telescope system and then physically retrieve the data at a convenient time using a portable hard drive or high capacity memory stick. This process is slower than real time download but is more practical where the download limit on an internet connection is a significant factor.

2.4.4 Unix

The robotic telescopes developed for MKO and Moore Observatory are based on open source code designed to run on unix-like platforms. Linux is the operating system of choice at the observatories and users are required to at least have a basic understanding of how to use it. Many of the applications require the user to enter command line statements to run various tasks. XmTel, XmCCD and XEphem are all examples.

Further, much of the post processing of the raw astronomical images was performed using applications designed to run under UNIX. IRAF is a well known example (section [2.7.1](#)).

Users unfamiliar with Linux typically face a steep learning curve when they first encounter the robotic systems implemented at MKO and Moore Observatory. However, as these robotic systems become more refined, the user interface between the fundamental applications and the user will likely evolve into a more graphically oriented and intuitive environment thus relying less on the user's knowledge of Linux. Such a user friendly interface is essential if a robotic telescope is to be widely adopted as may occur in an educational setting such as a university. This allows the focus to remain on the astronomy principles rather than having students spend considerable time learning about computer systems. However, an important issue that is brought to the reader's attention is the close relationship between IT and astronomy disciplines. Significant computer processing of raw astronomical data is often required in order to

extract the science, requiring researchers and students to have a solid grounding in computer science.

2.4.5 Virtual Private Network

The connection established between a remote user and the robotic telescope is implemented by way of a private network utilising the public internet to connect the parties together. Such a connection is called a Virtual Private Network (VPN) connection and allows one computer (say the remote user) to access another computer (say the local telescope control computer) via a secure communications tunnel over the internet.

A VPN connection is used to access the MKO computer from a remote location. In a similar way to use of computer operating systems, a user must also have sufficient knowledge of computer networking to create a VPN connection. This isn't always a straightforward task and can become a frustrating exercise for inexperienced users.

The generation and availability of a comprehensive user guide to a robotic telescope is an essential requirement, especially for widespread use of the system such as in a university environment. Researchers and students should be able to focus on their astronomical area of study and not have to be fluent in computer networking to use the robotic system. This is an important learning outcome from this thesis and is identified in the recommendations in Chapter 5.

2.4.6 Skype

The MKO and Moore observatories are equipped with video conferencing systems allowing researchers and students to communicate in real time in a face to face setting. Further, remote users of the system can use their own web cams and Skype software to provide video conferencing to the observatory.

Such a facility requires significant bandwidth and a minimum connection speed to provide useable video conferencing. For example, a typical video conferencing session from a remote computer using a web cam and Skype software to the observatory can require gigabytes of data exchange over the period of a few hours. Such a bandwidth requirement may not be sustainable for users with data caps on their internet plans. Based on experience using Skype video services between a remote computer in Brisbane and MKO, a typical broadband connection is sufficient to maintain a useable video conference.

2.4.7 Planning

All observation sessions need to be carefully planned prior to the observing evening so that time is not wasted. The most important aspect is to ensure that the target is visible for the required observation time. The observing undertaken for this thesis required the user to determine the target, filters, exposure times and the number and type of calibration frames required. Much of this information is able to be determined

prior to the start of observations, however exposure times are best determined after making a few test images.

The observations obtained for this thesis were made using the local telescope control computer at MKO and Moore Observatory. Full remote control from an external location is not currently available but is planned to be implemented in 2010. Once this system is commissioned, students and researchers will be able to make their observations from any remote location by establishing a VPN connection to the local telescope control computer.

2.5 Photometry

The issues involved in photometry are now discussed, in terms of sources of noise and the practicalities of reducing and analysing CCD data.

2.5.1 Shot noise

Shot noise occurs when the finite number of particles that carry energy is small enough to give rise to detectable statistical fluctuations in a measurement. In the case of shot noise associated with CCDs, the magnitude of the noise increases with the intensity of the light. However, since the magnitude of the average signal increases more rapidly than that of the shot noise, shot noise is often only a problem with low light intensities. For this reason, it is important to capture observations with a large number of photon counts without entering saturation (a condition in which either the finite charge capacity of individual photodiodes, or the maximum charge transfer capacity of the CCD, is reached).

The number of photons collected by a CCD follows a Poisson distribution. The standard deviation of the photon noise is equal to the square root of the average number of photons. The signal-to-noise ratio is then

$$\text{SNR} = \frac{N}{\sqrt{N}} = \sqrt{N}$$

where N is the average number of photons collected.

It can be seen that noise becomes more important when the number of photons collected is small.

2.5.2 Readout noise

Readout noise is introduced into a CCD image by two processes: the non perfect analogue to digital conversion and the injection of unwanted random signals by the sensor and electronics which end up being digitized along with the pixel charge. The combination of these processes results in uncertainty in the digitised output value for each pixel. Readout noise is added into every pixel every time the CCD array is read out.

2.5.3 CCD linearity

Linearity is a measure of how consistently the CCD responds to light over its well depth (the amount of charge that can be accumulated in an individual pixel). For example, if a 1 second exposure produces 1000 electrons of charge, 10 seconds should produce 10,000 electrons of charge. The deviation from this straight line function is a measure of non-linearity. In effect, any non-linearity indicates a change in the CCD's gain constant with signal level.

2.5.4 Photon transfer curve

A useful tool for characterising the performance of a CCD is the photon transfer curve. It provides a way of determining many characteristics of a CCD camera such as noise floor, full well capacity, gain and dynamic range (Kodak 2005). The photon transfer curve is a plot of the log of the standard deviation of the signal (y-axis) versus the log of the signal itself (x-axis). An example is shown in Figure 2.9 (a). The process of generating a photon transfer curve is beyond the scope of this thesis. Interested readers are referred to Kodak (2005), McLean (2008) and Gardner (nd) for more detail.

The plot in Figure 2.9 (a) has three regions:

- 1) The region in which the signal level is lowest is predominantly flat and the curve can be extended to the y-axis to give the camera's read noise floor. This parameter is often referred to as the readout noise of the CCD and can readily be found in manufacturer's datasheets. It is a random noise source generated in the CCDs output amplifier and external electronics. The readout noise for the SBIG STL-6303e CCD camera used at MKO is 13.5 electrons RMS.
- 2) The middle region of the plot has a slope of $\frac{1}{2}$ and represents the part of the camera's dynamic range over which its operation is shot-noise limited (section 2.5.1). Shot noise is caused by the random arrival of photons and is characterised by a Poisson distribution. It is a fundamental characteristic of light and is not related to the camera design.
- 3) The third region of the plot has a slope of 1 and is where the camera's operation is pattern-noise limited. Pattern noise results from differences in sensitivity between pixels and it is directly proportional to input signal strength.

The full well capacity of each pixel in the CCD array is the point on the photon transfer curve where the curve abruptly drops. This represents the maximum number of electrons that a pixel can hold without spilling over into adjacent pixel wells. Normally, a CCD camera is calibrated such that the maximum analogue-to-digital converter (ADC) output is achieved at or near the full well capacity (Gardner nd).

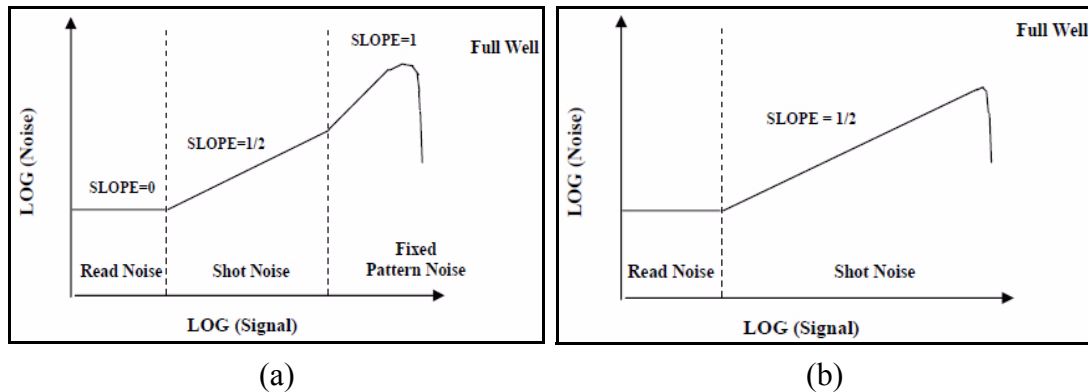


Figure 2.9 Example photon transfer curves

The full photon transfer curve shown in frame (a) illustrates the various noise regions. However, in practice, the fixed pattern noise portion of the curve is eliminated during measurement, and the shot noise region is extended to the point of full well operation. This is done to provide linearity and sensitivity data at higher illumination levels and is accomplished by subtracting two illuminated fields. Subtracting the two images eliminates fixed pattern variations since they are present in both images. With fixed pattern noise eliminated the photon transfer curve in frame (b) continues along with a slope of $\frac{1}{2}$ until full well occurs. (Gardner nd).

The photon transfer curve shown in Figure 2.9 (b) represents a typical curve used in practice. In this plot, the fixed pattern noise region is eliminated during measurement and the shot noise region is extended to the point of full well operation. This is done to provide linearity and sensitivity data at higher illumination levels (Gardner nd).

The gain of a CCD is the conversion factor between the number of electrons recorded by the CCD and the number of digital units and is typically expressed in electrons per ADC unit (ADU). It can be determined by plotting the photon transfer curve on linear axes where the inverse of the slope of the resulting curve is the gain. A lower gain is generally better, provided the full well depth can be represented, because the noise contribution from the electronics is minimised, giving better signal resolution.

Another important specification of an astronomical CCD camera is its dynamic range, which is the ability of the sensor to accurately record bright and faint light sources in the same image. It provides an indication of the minimum and maximum number of electrons that can be imaged. When the sensor is exposed to a light source, electrons are collected in each illuminated pixel and eventually the full well capacity is reached, a condition known as saturation. The SBIG datasheet states that the full well capacity of the SBIG-STL6303e is 100,000 electrons. The minimum signal that can be detected is not zero and is limited by the noise floor of the sensor. This figure can be extracted from the photon transfer curve as mentioned above and is typically a few electrons per pixel. The SBIG datasheet states that the SBIG-STL6303e read noise is 13.5 electrons per pixel. The dynamic range is often represented as a log ratio of the full well capacity to the readout noise in decibels. For example, in the case of the SBIG STL6303e CCD, with a full well capacity of 100,000 electrons and a readout noise of 13.5 electrons, the dynamic range is calculated as $20 \cdot \log_{10}(100000/13.5) = 77\text{dB}$ (Howell 2006).

2.6 Atmospherics

2.6.1 Astronomical seeing

Seeing is a measurement of atmospheric turbulence caused by anomalous refraction of a star's light in the Earth's atmosphere due to small scale fluctuations in air density usually related to temperature gradients. Seeing is often expressed in arcseconds referring to the size of a star's image on the CCD. In a practical sense, it refers to the blurring or enlargement of a star's image thus causing it to cover a larger number of pixels on the CCD. The width of the seeing disc is defined as the point where the intensity falls to half of the maximum intensity and is commonly called full width at half maximum (FWHM). Seeing varies from site to site and night to night and is one of the biggest problems with Earth-bound astronomy ([Warner 2006](#)).

2.6.2 Scintillation

Scintillation is a slightly different phenomenon to seeing and causes a star's brightness to vary rapidly (i.e. twinkle). It is caused by the same atmospheric turbulence that blurs a star's image on a CCD as described above. Small aperture telescopes are more affected by this phenomenon than larger aperture telescopes since larger telescopes are able to collect more photons thus averaging the intensity variations more so than small telescopes ([Warner 2006](#)). The effects of scintillation are much more pronounced near the horizon than near the zenith.

The noise contribution in a stellar magnitude measurement due to scintillation can be estimated using equation 3 of [Kjeldsen & Frandsen \(1992\)](#):

$$\sigma_{\text{scint}} = (0.09 \text{ mag}) \cdot D^{-2/3} \cdot \chi^{3/2} \cdot \exp(-h/8) \cdot \Delta t^{-1/2}$$

where:

D is the aperture of the telescope (cm)

χ is the air mass

h is the altitude of the observatory (km)

Δt is the exposure time (s)

For the CDK20 telescope at MKO with $D=50\text{cm}$, $\chi=1.5$, $h=0.682\text{km}$ and $t=10\text{s}$, the estimated noise due to scintillation is 3.5mmag rms per image.

2.6.3 Extinction

Extinction is the dimming of a star's light caused by going through the Earth's atmosphere. It is expressed in units of magnitudes per air mass. Even on the clearest of nights, stars are dimmed significantly by absorption and scattering of their light by the atmosphere. The degree to which a star's light is dimmed is dependent on its altitude, the wavelength of its light and the current atmospheric conditions. Shorter wavelengths are more strongly attenuated by the atmosphere than longer wavelengths

causing the observed light to be redder than expected i.e. the shorter the wavelength, the greater the extinction. This colour-dependent extinction is commonly referred to as *reddening*. Pont et al. (2006) provides an analysis of the effects of red noise in ground based transit surveys.

If the object of the photometry is to be able to compare the results to observations made by other observers using different equipment at different locations, then it is necessary to determine the above atmosphere magnitudes and colour indices. However, the use of extinction coefficients is not required if the objective of the photometry is to obtain lightcurves using differential photometry for a very small angular separation as is the case for the photometry performed for this thesis.

For completeness, a description of how extinction coefficients are determined including some rule-of-thumb practices is provided in [Appendix A](#) section [A2](#).

2.7 Data reduction

2.7.1 IRAF

The Image Reduction and Analysis Facility (IRAF) is a collection of software written at the National Optical Astronomy Observatory (NOAO) for the reduction of astronomical images. It has long been the scientific community's standard reduction software for astronomical work. IRAF is available free of charge from <http://iraf.noao.edu/>. All of the photometry results presented in this thesis have been generated using IRAF running on a Ubuntu Linux virtual machine hosted on a Windows 7[®] operating system.

2.7.2 Image calibration

A raw CCD image contains a combination of wanted signal along with some unwanted contributions such as bias voltage, dark current and non-uniform pixel sensitivity. Therefore, it is necessary to remove these unwanted contributions so that the final image only contains the desired signal. Of course, the calibration process is not 100% efficient, however with a robust calibration process, these effects can be managed.

The calibration process involves taking additional images during the observing run that are later used to subtract the additive values and divide out the multiplicative factors ([Henden & Kaitchuck 1990](#)).

2.7.2.1 Dark current

The thermal agitation of atoms in the silicon substrate of a CCD frees electrons. This process occurs even when the CCD is in total darkness. The resulting steady creation of free thermal electrons is called dark current ([Berry & Burnell 2009](#)). At room temperature, the noise performance of a CCD can be as much as thousands of

electrons per pixel per second causing the pixel well to saturate within a few seconds of being exposed to light. The rate at which electrons are freed is constant for any given temperature, however for every 6°C increase in temperature the dark current approximately doubles. Stated another way, reducing the temperature by 10°C increases the CCDs sensitivity by one stellar magnitude. At -100°C, the dark current becomes almost negligible (Buil 1991). The noise introduced by thermal electrons has a Poisson distribution hence it is proportional to the square root of the dark current (Howell 2006).

Typical dark current values for cooled CCD cameras range from 2 electrons per second per pixel down to 0.04 electrons per second per pixel. The dark current specification for the SBIG STL-6303e CCD used at MKO is 0.3 electrons per pixel per second at 0°C. The actual operating temperature of the CCD was -15°C when making the observations for this thesis.

When undertaking an observing run, it is normal practice to generate a series of dark frames so that the effect of the dark current in the science frames can be calibrated out.

2.7.2.2 Dark frames

A dark frame captures a sample of the dark current and is made by taking images at the same exposure time as the science frames but with the camera shutter closed.

There are two methods of generating master dark frames. The first is called the standard method and is what is used in this thesis. The second method generates scalable dark frames that are more flexible than the standard method dark frames but require the use of bias frames. A scalable master dark frame is made by taking multiple exposures longer than the longest exposure time used in any of the science frames. However, to allow the master frame to be scalable to any exposure time, the bias signal must first be subtracted. The master bias frame is a combination of multiple images taken with zero exposure time.

The goal is to create a dark frame that is sufficiently accurate that subtracting it from the science frame will not significantly increase the noise in the calibrated image. To achieve this, a master dark frame is created by combining individual dark frames. As a general rule, the total exposure time of the dark frames should be at least 5 times longer than the individual science frames. This will reduce the noise contribution caused by the dark subtraction to an addition of 10% which is generally considered acceptable (Berry & Burnell 2009). The master dark frame is created by median combining the individual dark frames. This process rejects extreme pixel values such as those arising from cosmic ray hits.

2.7.2.3 Flat frames

The pixels of a CCD sensor are not all created with the same sensitivity, some pixels are more sensitive than the average, some less. The flat field calibration is designed to account for these variations. In addition to the individual pixel variations, the flat field

image records the response of the entire optical system comprising the telescope, filters, window and cover glass. The resulting variations in the flat field may be caused by any of these factors in isolation or in combination. Because different filters will be used during the observing run, it is then necessary to create a master flat field image for each filter. Flat fielding has its limitations such as opaque spots on the chip or effects from external sources such as scattered or reflected light hitting the primary mirror.

There are 4 methods for taking flat field images: 1) Light box flats, 2) dome flats, 3) twilight flats, and 4) sky flats. Light box flats are taken by placing a light box in front of the telescope. Dome flats are taken of an evenly illuminated portion of the inside of the dome. Twilight flats are taken by pointing the telescope near the zenith at dawn or dusk when it is dark enough not to saturate the CCD but light enough that very few, if any, stars are visible. Normally the telescope is moved slightly between each image so that any stars that may appear can be eliminated during the combining process. Sky flats are taken by taking the median of a large number of images of the night sky. At MKO, dome flats are used where a dedicated portion of the dome is evenly illuminated. This method has the advantage of being available at any time and the process can take as long as required. This contrasts with twilight flats where there is only a very brief period of time available to take all the required flat field images.

In general, a flat field image should fill the charge wells of the CCD sensor to roughly half capacity and, if using an artificial source as is the case at MKO the light intensity should be set so that exposure times are between 2 and 10 seconds (Berry & Burnell 2009). Because dark current effects are also present in all of the flat field images, it is necessary to take flat dark field images of the same exposure. The master flat field is created by subtracting the master dark frame from each of the individual flat frames and then median combining the individual flat frames.

It is important to recognise that the master flat is only valid for the optical configuration used to take the individual calibration frames for the specific filter. If the camera is rotated or the focus is changed or a new filter is used or the dust on the various optical surfaces changes, a new master flat will be required.

2.8 Observing procedures

2.8.1 Target selection

Prior to any observing session, the targets are determined well ahead of time. This involves determining which targets will be visible and the times at which they are best observed. The target coordinates and times are recorded in preparation for the observation run.

To demonstrate the photometric performance of the telescopes used for this thesis, three types of photometry targets were selected for rapid cadence photometry:

- 1) Photometric standard stars. These stars have had their intensity carefully measured through various photometric filters and are accepted standards in the scientific community against which other stars can be compared. Standards often used are the Harvard E-region stars, which are centered around declination -45° . The standards chosen for this thesis are a selection of stars from Graham's E2-Region of the Harvard E-Regions ([Graham 1982](#)).
- 2) Spotted stars. In star spots, the intense magnetic fields can suppress the convection of heat to the surface, and hence, that area will radiate less light, causing a dark area on the stellar surface ([Rabus et al. 2009](#)). Star spots are temporary phenomena on time scales of weeks to months. The interested reader is referred to [Eker \(1999\)](#) in which he discusses star spot photometry, associated techniques and problems. HIP71933 and HIP93378 were the chosen spotted stars used in this thesis. These stars are targets for ZDI research being conducted at USQ.
- 3) An exoplanet transit. When a planet crosses in front of its host star as observed from Earth, the brightness of the host star drops by a small amount. This is known as an exoplanet transit event. Exoplanet WASP12b was observed for this thesis.

The spotted stars HIP71933 and HIP93378 were chosen because they are a good example of active young stars with high rotation rates. Photometry of these stars is therefore useful for determining the rotation period to improve the mapping of star spots for ZDI research. The exoplanet transit of WASP12b was chosen because it is known to have a short duration and the transits are readily observable. Overall, the choice of targets was dictated by the need for timely collection of data and the star's visibility from MKO and Moore Observatory. Taken together, these three types of observations serve to illustrate the capability of the telescopes for scientific research.

2.8.2 Capturing bias, dark & flat frames

Prior to observing any of the targets, it is necessary to take a series of calibration frames known as flat fields. These are used during the data reduction process to improve the quality of the final science frames by removing pixel-to-pixel variations across the CCD sensor. At least 20 flat field images and flat dark images are taken through each of the photometric filters during this process that are later combined into a master flat field frame for each filter. Refer to section [2.7.2](#) for more details about the calibration process.

Once the flat fields images have been taken, the telescope's coordinates are then setup by pointing the telescope at a known bright star. XEphem is used as the primary control interface for the telescope mount and camera. Many astronomical catalogues provide epoch 2000 coordinates that must be converted to present day coordinates to account for earth's precession. The telescope is then slewed to centre the bright target and XEphem records the offsets required to centre the star. At the end of this process, celestial coordinates are able to be entered into XEphem and it can then accurately control the telescope mount to point at the target.

2.8.3 Exposure time

The next step is the determination of an appropriate exposure time. In general, the ADU count for the target CCD pixels should be kept well below the maximum achievable count due to potential non-linearity in the CCD near the maximum and to avoid saturation. Further, the exposure time needs to be long enough to achieve a good signal to noise ratio. The datasheet for the CCD sensor used in the SBIG STL6303e camera states that the output is linear within 2% from 1% to 90% of the output saturation voltage. Therefore, a good target value to use is around 50% of maximum ADC output whilst ensuring that it does not exceed 80%. Thus, an ADC output of around 50,000 ADU was considered to be the maximum useable value with a good target value being about 32,000 ADU. Test images were taken to determine the best exposure time to achieve the target value of 32,000 ADU for all the targets selected for this thesis.

2.8.4 Observing run

Once the exposure time is determined, the observations can begin. In order to minimise the colour-dependent effect air mass has on attenuating starlight (red light is scattered less by the atmosphere relative to blue light), observations are typically made well above 30deg altitude. For the MKO setup, a set of 10 images is taken through each filter and the process is then repeated until the desired number of science frames have been captured.

Bias frames are taken and subtracted from other frames, and dark frames are taken at some convenient point during the observation run. These dark frames are calibration frames taken with the same exposure time as the science images but with the shutter closed. If more than one exposure time has been used during the observation run then at least 10 dark frames are taken at each of the times used. These dark frames are later combined into a master dark frame for the specific exposure time or times.

2.9 Calibration of Graham's E2-Region

To illustrate the calibration procedure further, this section outlines the calibration technique that was applied to Graham's E2 Region science frames for this thesis. [Figure 2.10](#) shows the master dark frame and the master flat frame used in the processing of Graham's E2 Region science frames.

The master frames were created by median combining as described in sections [2.7.2.2](#) and [2.7.2.3](#) so that the resulting master frame has less random noise than any single frame. In the examples shown in [Figure 2.10](#), approximately 10-20 individual calibration frames were median combined to produce the master frames.

[Figure 2.11](#) shows the difference between a raw (un-calibrated) image and one that has had the effects of dark current removed and has been flat fielded. Calibration of the science frames is essential when trying to achieve milli-magnitude photometric precision.

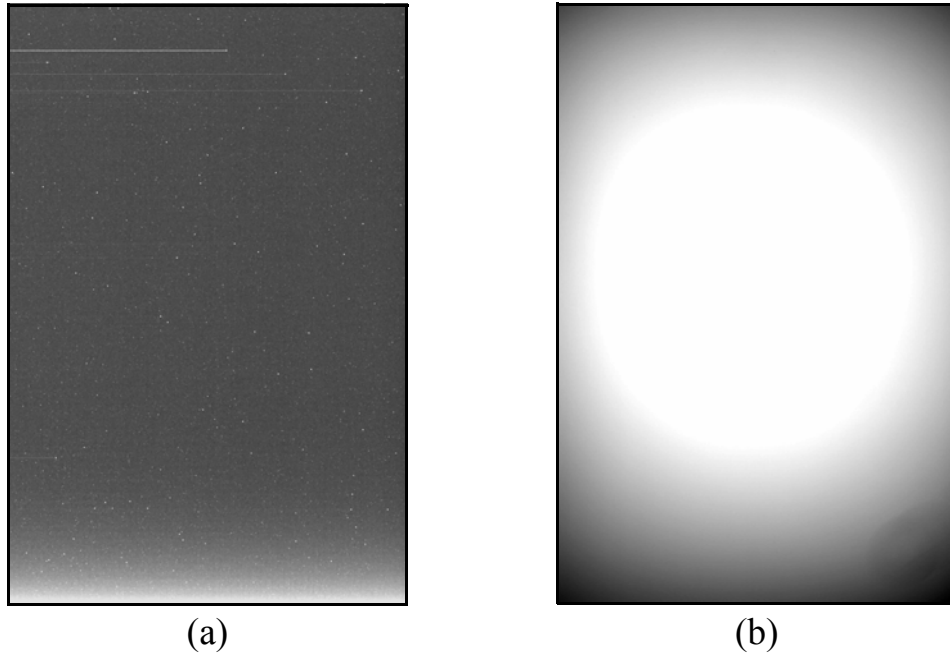


Figure 2.10 Example calibration images

(a) Master dark frame. (b) Master flat frame. Not shown in this figure is an example of a bias frame. A bias frame can be thought of as a zero exposure time dark frame. As such, a bias frame typically looks similar to the dark frame but has a much lower ADU count per pixel than a typical dark frame.

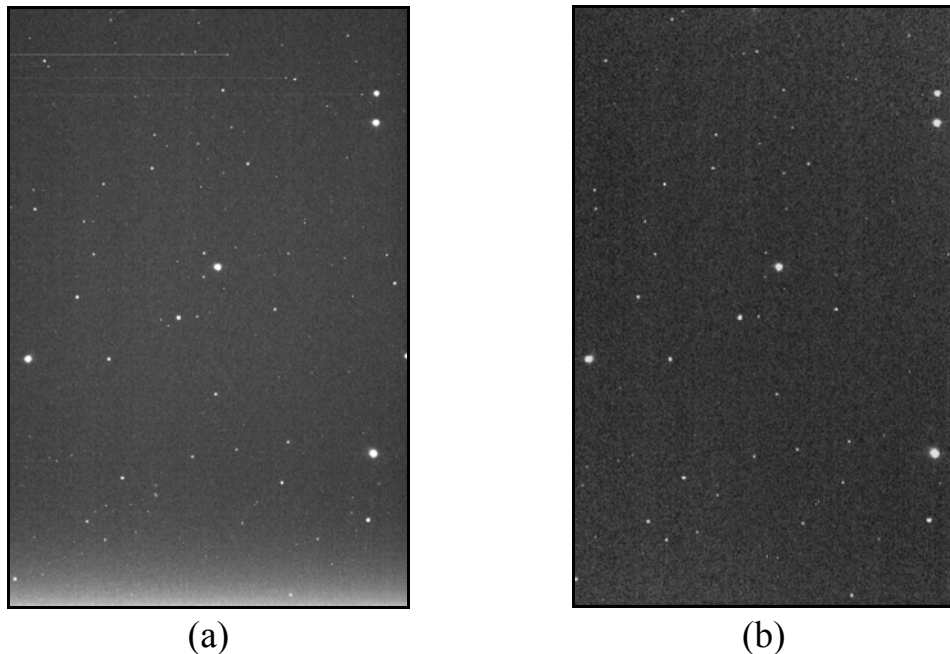


Figure 2.11 Pre and post image calibration frames of Graham's E2 Region

(a) Raw science image prior to calibration. Note the hot region along the bottom edge (due to the way in which the CCD is readout) and the rows of hot pixels along the top (typically due to manufacturing defects). These issues can be significantly reduced through the careful application of calibration frames. (b) The same image post calibration. Note that the background intensity is far more uniform and the rows of hot pixel have been eliminated.

2.9.1 Photometry techniques

2.9.1.1 Aperture photometry

Aperture photometry involves defining a set of concentric regions (usually circular) centred on the target star. [Figure 2.12](#) shows the configuration of these concentric regions. The image of the star is contained within the central aperture and contains light from the target as well as background sky and other starlight. To extract the brightness of the target star from the image, all of the pixels values in the central aperture are added and then an estimate of the sky background is subtracted from it. The sky background estimate is determined by taking the mode of all the pixel values in the region between the inner annulus and outer annulus.

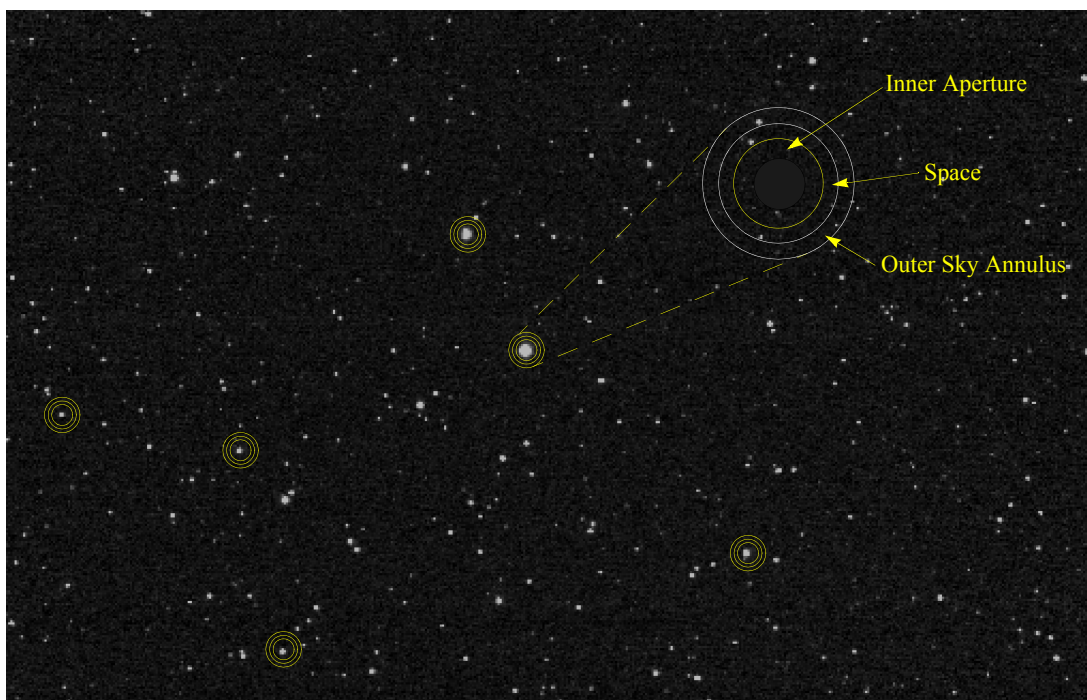


Figure 2.12 Aperture photometry

The brightness of a star is determined by summing the pixel values within the central aperture (shown in yellow) which includes skylight and starlight from the background as well as the target. An estimate of the sky brightness is then made by taking the mode of the pixel values between the inner annulus and outer annulus (shown in white). This value is then subtracted from the total aperture value to determine the star brightness.

The advantage of this technique is that it is simple and does not require well sampled images. In order to sufficiently measure the total flux for under-sampled pixels, the aperture must be rather large thus adding error due to the sky background. For brighter stars, where the sky background is much less significant, aperture photometry can perform as well as precise Point Spread Function (PSF) fitting ([Kjeldsen & Frandsen 1992](#)). The main disadvantage of aperture photometry is that star images can be spread over a large number of pixels requiring a relatively large aperture that may include other nearby stars, especially in crowded star fields. Aperture photometry has been exclusively used for the data analysis performed for this thesis.

2.9.1.2 Point spread function photometry

When doing photometry on crowded star fields, such as globular clusters or open clusters, aperture photometry will not yield reliable results. In this case, it is better to use the PSF technique.

PSF photometry involves a gaussian curve that can be fitted to all of the stars in the field in order to find their magnitudes and requires well sampled stellar images. If the images are severely undersampled, significant errors will arise due to an inability to match the real PSF to the model PSF (Kjeldsen & Frandsen 1992).

2.9.2 Differential photometry

Differential photometry is the most accurate technique for measuring small variations in brightness. It relies on having a comparison star against which the target star is measured, hence the result is a relative measurement. This type of photometry can achieve milli-magnitude accuracy photometry if appropriate care is taken in calibrating and measuring the images. Two types of measurements can be made:

- 1) Magnitude measurements: a direct measure of the star's brightness through any given filter.
- 2) Colour Index measurements: a difference in the magnitude measured through 2 different filters. Colour indices allow corrections to be made that remove the effects of extinction. The $(V - I)$ colour index is particularly useful as it provides a very good temperature indicator for all stars (Barnes et al. 1978 and Berry & Burnell 2009).

The other main type of photometry is known as All Sky Photometry in which the absolute brightness of a celestial object is measured. The photometry work presented in this thesis is based on differential techniques where the magnitude of the target star was compared to a comparably bright comparison star in the same frame. The comparison star was typically chosen to be close to the target star in location and spectral type to minimise the impact of flat fielding imperfections and extinction on the photometric results (atmospheric extinction causes changes in both magnitude and colour index but the differential effect is minimised when two stars have similar altitudes). Generally, if the target and comparison stars are in the same frame then the extinction can be ignored (Henden & Kaitchuck 1990) provided the stars are approximately the same colour. If this is not the case then the results must be corrected to account for this. Section 2.6.3 explains extinction and its effect in more detail. The effects of extinction and colour difference have been mitigated by judicious selection of comparison stars.

The counts from ~5-10 other stars in the same frame were then used to generate a synthetic check star as most of the stars in the target frame are fainter than the target. Using the combined counts thus had the effect of increasing the signal to noise ratio of the check star. The variability of the comparison was then tested against the synthetic check star.

2.10 Data interpretation

2.10.1 Use of photometry to support DI

As mentioned in section 1.3, photometry is used in DI research to provide the rotation period of the target star and to significantly improve the mid latitude star spot features by providing both the unspotted V magnitude and the photospheric and spot temperatures. Neither of these can be constrained without the incorporation of multi-colour photometry into the DI data set (Marsden 2005).

2.10.2 Transit light curves for exoplanet studies

There are five primary features of a light curve that can be used to identify an exoplanet transit. These features are explained in detail in Hamacher (2008) and briefly outlined in the following paragraphs.

2.10.2.1 Period

The duration of an exoplanet transit depends on the period of the orbit and the inclination angle of the transit, with 90 degrees being directly across the centre of the disk. Hamacher's thesis reported the longest period exoplanet at the time was HD17156b at just over 21 days. Since 2008, numerous longer period planets have been discovered by transit detection with the largest being HD187123c with a period of about 10 years (Wright et al. 2009). Similarly, the shortest period exoplanet is currently WASP19b with a period of 0.789 days. Photometry results for WASP12b are presented in section 3.7.

2.10.2.2 Transit depth

The depth of an exoplanet transit can be described in terms of the planet's radius and host star's radius. If it is assumed that a Hot Jupiter could be a maximum of twice the size of Jupiter, the largest star for which a transit could be detected with a photometric precision of ~3-5 mmag would be twice the size of the Sun, roughly corresponding to a late A-star. Therefore, stars from spectral types A-K are considered possible exoplanet transit hosts, though it is expected to have many more G-K type stars in any given field since K-stars are ~10 times more abundant than A-stars, while G-stars are ~5 times more abundant (Hamacher 2008).

An exoplanet can effectively be considered a "dark" body due to the very large luminosity ratio between the host star and the exoplanet. Therefore an exoplanet transit is only very slightly colour-dependent meaning there will be very little difference in transit depth when observed in different colour filters.

2.10.2.3 Transit duration

For transits across the centre of the star, the transit duration can provide information on the orbital semi-major axis of the planet, as given by the following equation (Hamacher 2008):

$$\tau_c = 13 \cdot d^* \cdot \sqrt{\frac{a}{M^*}} \cong 13 \cdot \sqrt{a} \text{ hrs}$$

where:

d^* is the stellar diameter in solar diameters

a is the orbital semi-major axis in AU

M^* is the stellar mass in solar masses

The transit duration also provides information about the relative size of the planet.

2.10.2.4 Transit shape

Planets that fully superimpose their host stars during transit will have a distinctive flat or slightly rounded bottom to the transit, depending on stellar limb-darkening. They will also have distinctive ingress and egress events. There is a colour-dependent change in the shape of the transit during ingress and egress, caused by the limb-darkening of the star during the planet transit (Tingley 2004).

2.10.2.5 Out-of-transit features

The out-of-transit light curve of a planet should be flat with no features, such as secondary transits. A secondary transit occurs when the smaller (or fainter) object, be it a planet or a star, is eclipsed by the larger object (Figure 2.13). While a very large, hot planet transiting a cool dwarf star can produce a measurable secondary transit, the photometric precision required to detect a secondary transit is generally sub milli-magnitude.

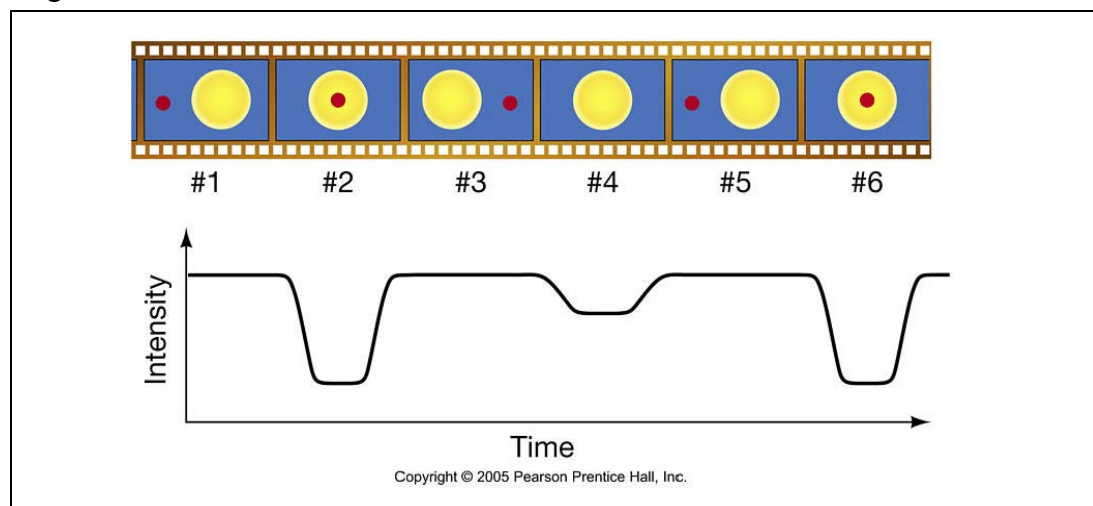


Figure 2.13 Exoplanet light curve

The primary transit is defined as when the planet transits the host star (#2), causing the deeper transit. When the planet is occulted by the host star, a shallower secondary transit is visible (#4). Image from http://physics.uoregon.edu/~jimbrau/BrauImNew/Chap17/FG17_21.jpg.

2.10.3 Photometry for the MicroFUN microlensing network

As mentioned in section [1.4.5.2](#), the MicroFUN microlensing network uses follow-up photometry measurements of detected lensing events to search for brightness variations that betray the presence of an exoplanet orbiting a lensing star. Once a lensing event has been confirmed, the network is able to quickly inform the participants so that many independent observations can be made. The MicroFUN network then collects and combines the data from the individual collaborating members making the findings available on their website.

Chapter 3: Results

3.1 Introduction

This chapter presents all of the photometry results obtained for this thesis. An observing log has been provided in [Table 3.1](#) and a summary of the photometry targets has been provided in [Table 3.2](#). The observations were generally made by others and provided to the author for processing. The following sections acknowledge the specific observers.

3.2 Observing log

Table 3.1 Journal of photometric observations

Date	HJD (start time)	Observatory/ Telescope	Target	T_{exp} (s)
25 Mar 2009	2454916.04017975	MKO/CDK20	HIP71933	10-30
27 Mar 2009	2454917.99822239	MKO/CDK20	HIP71933	10-30
04 Dec 2009	2455193.79738318	MKO/CDK20	E2-Region	10
14 Jan 2010	2455210.63971716	Moore/RC24	WASP12b	100
14 Jan 2010	2455210.66424190	Moore/CDK20	WASP12b	100
27 Jun 2010	2455374.95224700	MKO/CDK20	HIP93378	10-30
03 Jul 2010	2455380.92166700	MKO/CDK20	HIP93378	10-30

3.3 Summary of results

Table 3.2 Photometry target summary

	E2-Region	HIP71933	HIP93378	WASP12b	
Observatory	MKO	MKO	MKO	Moore	
Telescope	CDK20	CDK20	CDK20	CDK20	RC24
Filter	B	V	V	R	
Target Magnitude	~7.8 - 15.3	~8.5	~8.5	~11.6	
Calibration frames	Darks/Flats	Darks/Flats	Darks/Flats	Bias/Darks	
Photometry processing package	IRAF	IRAF	IRAF	IRAF	
Results cross reference	3.4	3.5	3.6	3.7	

3.4 Graham's E2-Region photometric standards

Observations of standard stars in Graham's E2-Region (Graham 1982) were made to assess the photometric precision of the CDK20 telescopes. The observations were made using the MKO CDK20 by Dr Rhodes Hart with the assistance of the author. Table 3.3 provides a list of the E2-Region stars that were observed.

Table 3.3 Graham's E2-Region targets

Star	V	B	B-V	V-R	R-I
E2:C	7.638	7.815	0.177	0.087	0.089
E2:F	8.19	8.317	0.127	0.061	0.067
E2:N	8.478	9.205	0.727	0.409	0.392
E2:Q	8.771	9.778	1.007	0.543	0.488
E2:S	9.502	10.089	0.587	0.328	0.313
E2:b	11.577	12.106	0.529	0.306	0.297
E2:l	12.98	13.607	0.627	0.353	0.358
E2:m	13.097	13.903	0.806	0.439	0.384
E2:o	14.09	14.66	0.57	0.312	0.326
E2:s	14.596	15.323	0.727	0.372	0.341

The target stars range in magnitude from 7.638 to 14.596 in the visual band. All targets are visible in a single frame (Figure 3.1) taken with the SBIG-STL6303e CCD camera fitted to the CDK20s telescope at MKO.

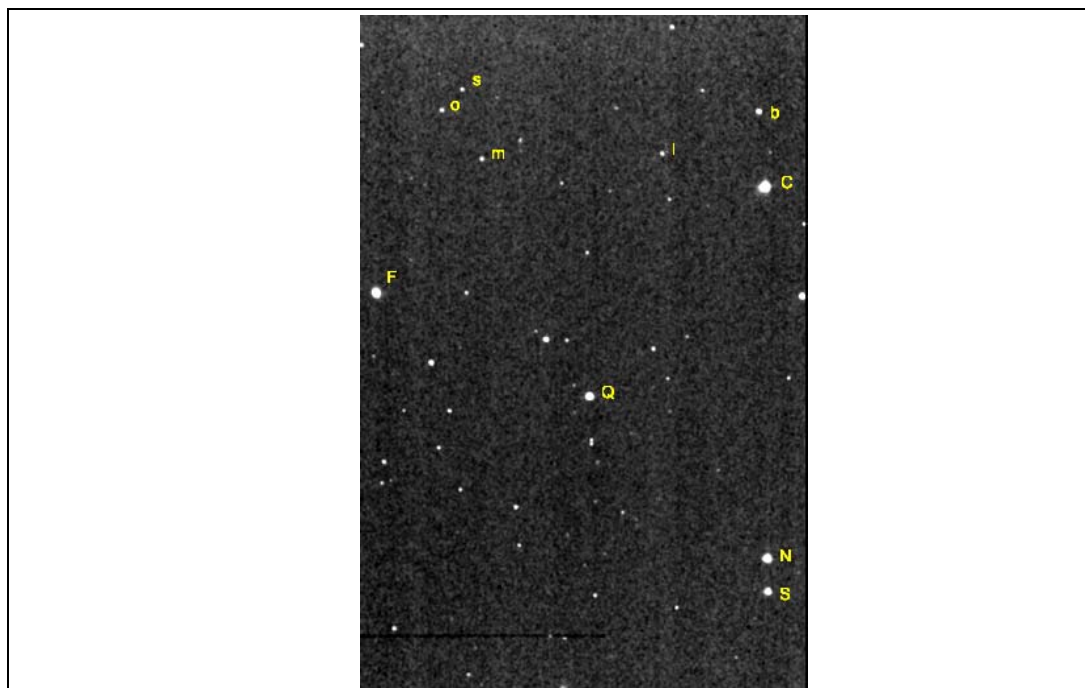


Figure 3.1 Graham's E2-Region star identification frame

For each star listed in Table 3.3, a comparison and check star were used to perform differential photometry. The comparison star chosen was the brightest star available

from the other E2 stars listed in the table. The check star was a synthetic star generated by combining the remaining E2 stars in the table with the exception of E2:s as it was considered too faint.

Figure 3.2 shows the light curve for star E2:C which was the brightest standard star studied in the region at magnitude 7.638 resulting in an ADU count of approximately 35,000. It shows a consistent straight line with a standard deviation of 0.004 indicating that the telescope system is capable of milli-magnitude photometry. This level of accuracy would enable the telescope system to be used for exoplanet transit searches.

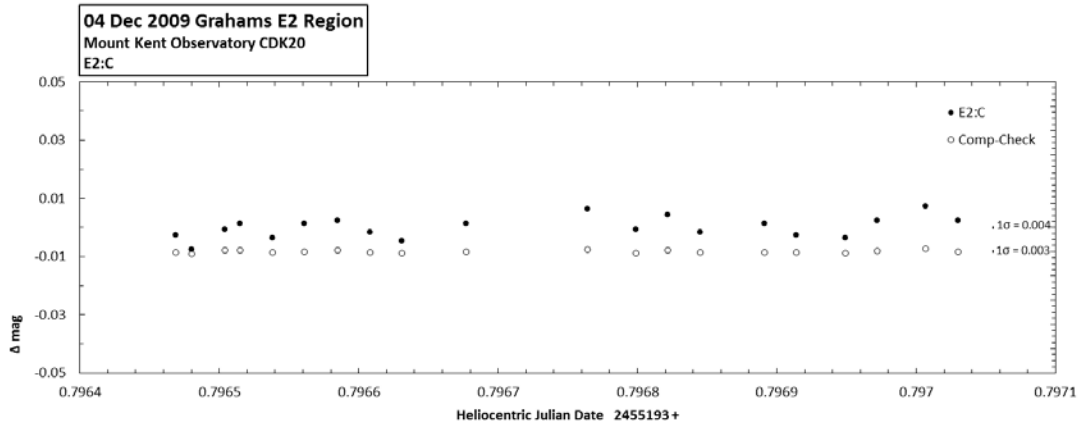


Figure 3.2 Graham’s E2:C standard star light curve

The exposure time for the field was set to ensure that this star (the brightest standard in the field) did not saturate the CCD. Thus, the ADU count for this target was relatively high at approximately 35,000. With this high count, the resulting standard deviation of the light curve was 0.004mag indicating that the CDK20 could potentially be used to observe at least magnitude 7.6 or brighter targets.

Figure 3.3 shows the light curve of star E2:s which was the faintest standard star studied in the region at magnitude 14.596 resulting in an ADU count of approximately 60. Practical photometry cannot be performed with such low ADU counts due to the significantly larger proportion of noise associated with the observation. These data have been provided in this thesis to gauge the degradation in performance of the CDK20 for fainter targets with all other parameters remaining constant. The result demonstrates the need to attain a relatively high ADU count in order to achieve milli-magnitude photometric performance. The standard deviation of all the sample points for the light curve was 0.113 magnitude which is unsatisfactory for exoplanet detections.

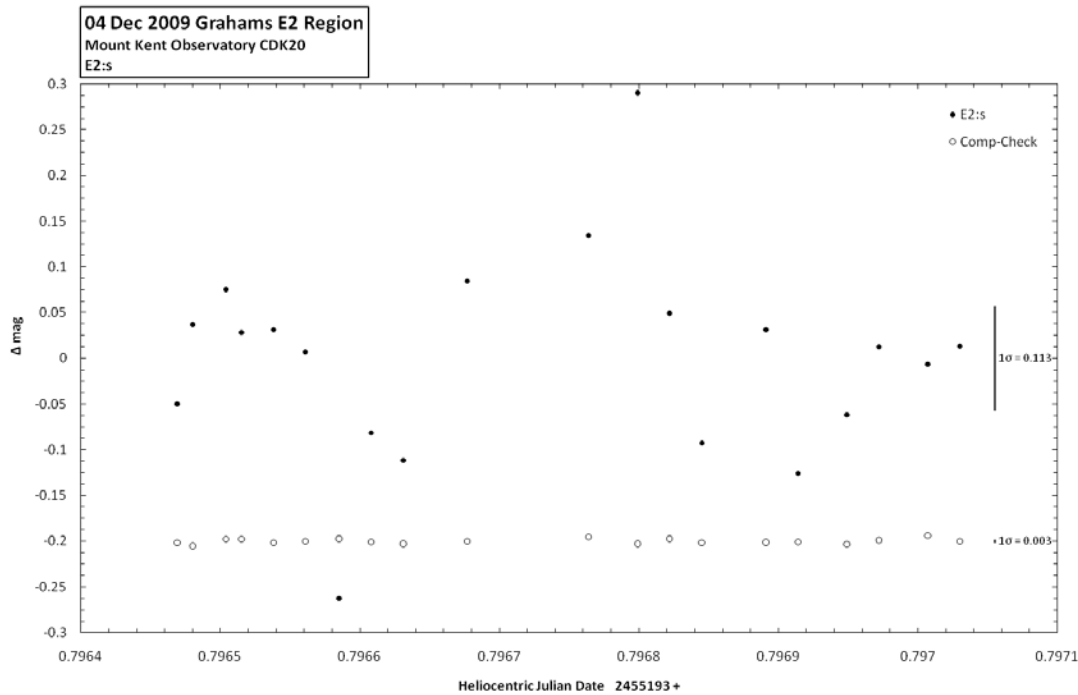


Figure 3.3 Graham’s E2:s standard star light curve

As expected, this light curve shows that the photometric accuracy has significantly degraded compared with the brighter targets thus demonstrating the need to ensure observations are made with relatively high ADU counts.

The results for all of the Graham E2-Region standard stars observed are provided in [Appendix B](#).

3.4.1 Photometric precision

The relationship between stellar magnitude and the standard deviation in the photometric measurements for a fixed exposure time is shown in [Figure 3.4](#). It is evident that the accuracy of the photometric system degrades with increasing magnitude.

The reason for the degradation in photometric accuracy is the reduction in the signal to noise ratio of higher magnitude targets for any given exposure time. Specifically, the exposure time was identical for both light curves shown in [Figure 3.2](#) and [Figure 3.3](#) because both stars are present in a single observation. The exposure time was chosen so that the brightest star would not saturate the CCD. If the target of interest is a fainter star such as the 15th magnitude E2:s shown above, then the exposure time

could be increased so that the signal to noise ratio is increased thus improving the accuracy.

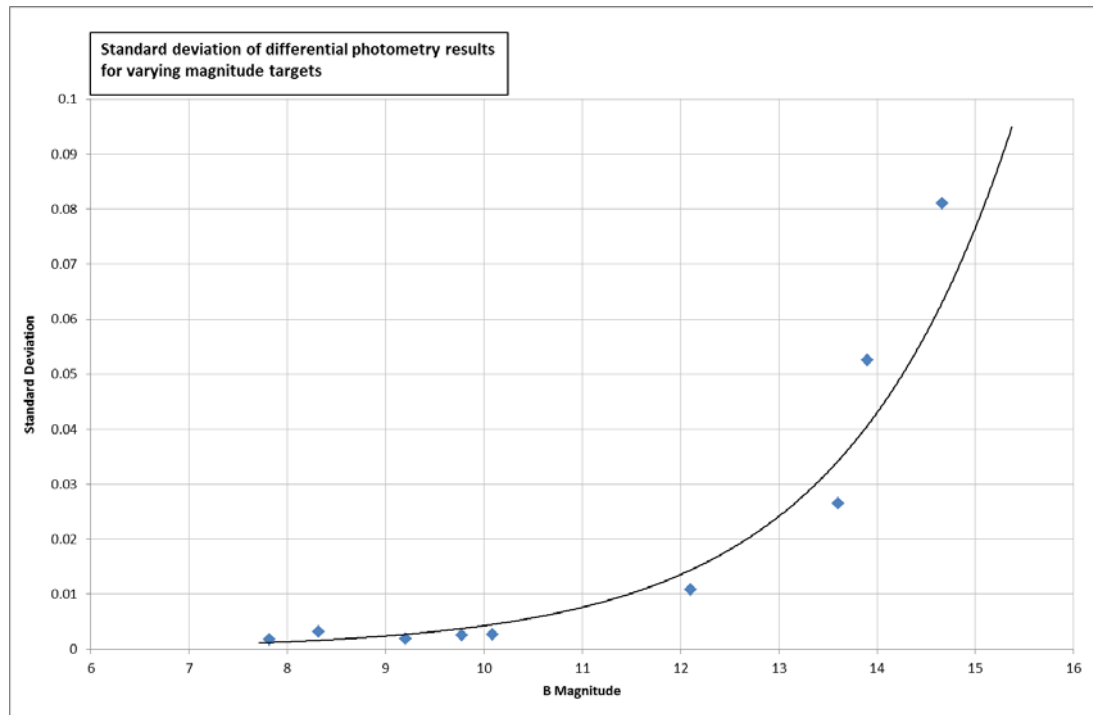


Figure 3.4 Differential photometry accuracy as a function of magnitude

This plot shows the standard deviation in the differential photometry measurements as a function of stellar B magnitude for a given exposure time.

3.5 Spotted star HIP71933

The second target used to assess the photometric performance of the CDK20 telescope was spotted star HIP71933, magnitude 8.5 (V) and spectral type F8V. This pre-main sequence star was chosen for observation because its rotation period is a required input for the ZDI research being conducted by Ian Waite at USQ. The observations were made using the MKO CDK20 by Ian Waite and provided to the author for analysis.

Table 3.4 provides colour and magnitude data for the target, comparison and check stars used in the photometry analysis. The check stars listed in the table were combined into a new synthetic check star. The average ADU count achieved for the target was $\sim 30,000$.

Table 3.4 HIP71933 comparison and check stars

Star	Type	B-V	Magnitude
1	Target	0.6	8.5
2	Comparison	0.07	9.2
3	Check	1.39	12.9

Table 3.4 HIP71933 comparison and check stars

Star	Type	B-V	Magnitude
4	Check	1.58	10.8
5	Check	0.92	10.8
6	Check	1.01	11.4
7	Check	1.11	11.2
8	Check	1.14	11.4

Figure 3.5 shows the relative positions of these stars.

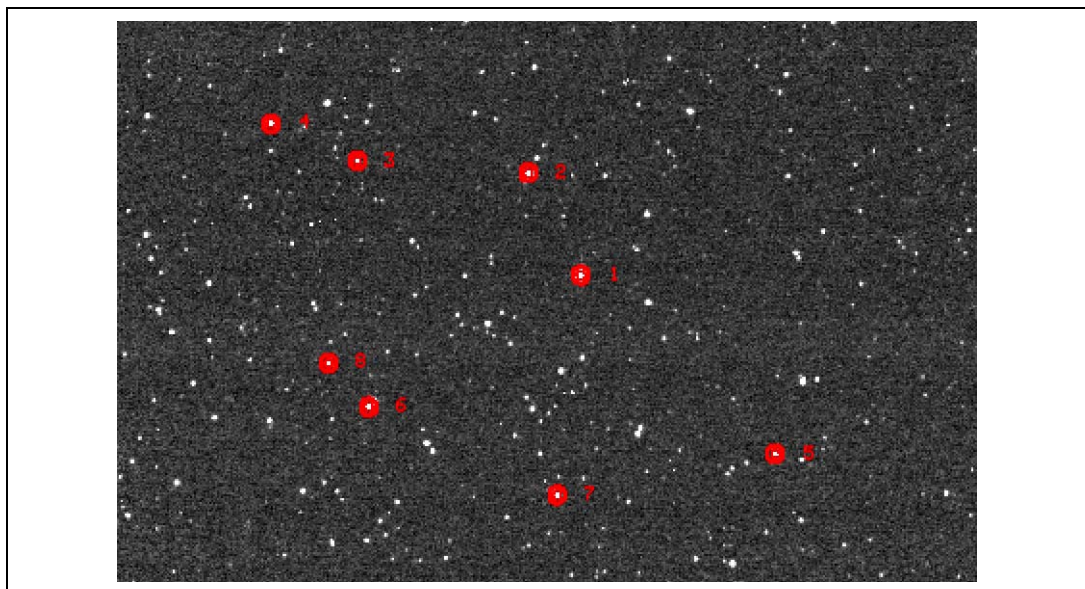


Figure 3.5 HIP71933 star identification frame

This frame shows the target HIP71933 labelled (1), the comparison star labelled (2) and the check stars (remaining numbered stars) used for the analysis.

The objective of observing this star was to demonstrate that the CDK20 telescope is capable of detecting the intensity variation caused by the presence of star spots on a rapidly rotating target. Observations were made over two nights and the resulting light curves are shown in [Figure 3.6](#) and [Figure 3.7](#). On both nights, a partial light curve was evident in the analysed data showing that the star's brightness variation is at least 0.04 magnitudes. There were insufficient observations to plot an entire cycle of the variation or for the IRAF Phase Dispersion Minimisation tool to extract a rotation period for the star. The [Hipparcos Epoch Photometry Search Facility](#) was used to view the photometry data collected by the Hipparcos Mission. Whilst some photometry data were available, not enough data points were present to determine a period. Further observations of this target are required to determine a robust period estimate.

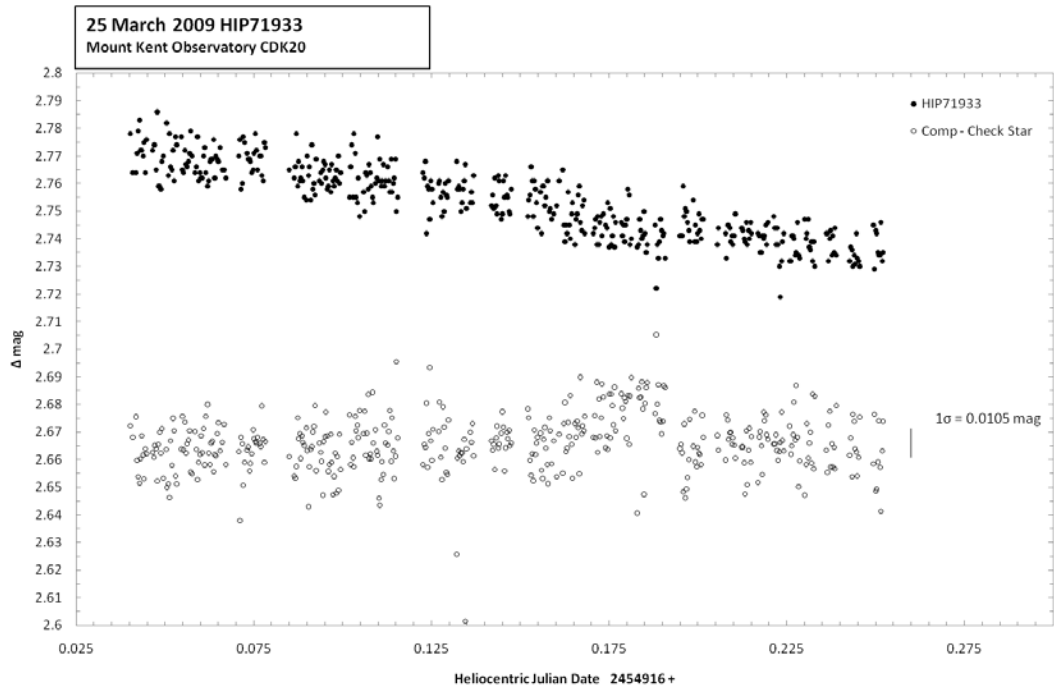


Figure 3.6 Spotted star HIP71933 - 25 March 2009

This light curve was derived from observation made using the MKO CDK20 telescope on 25 March 2009.

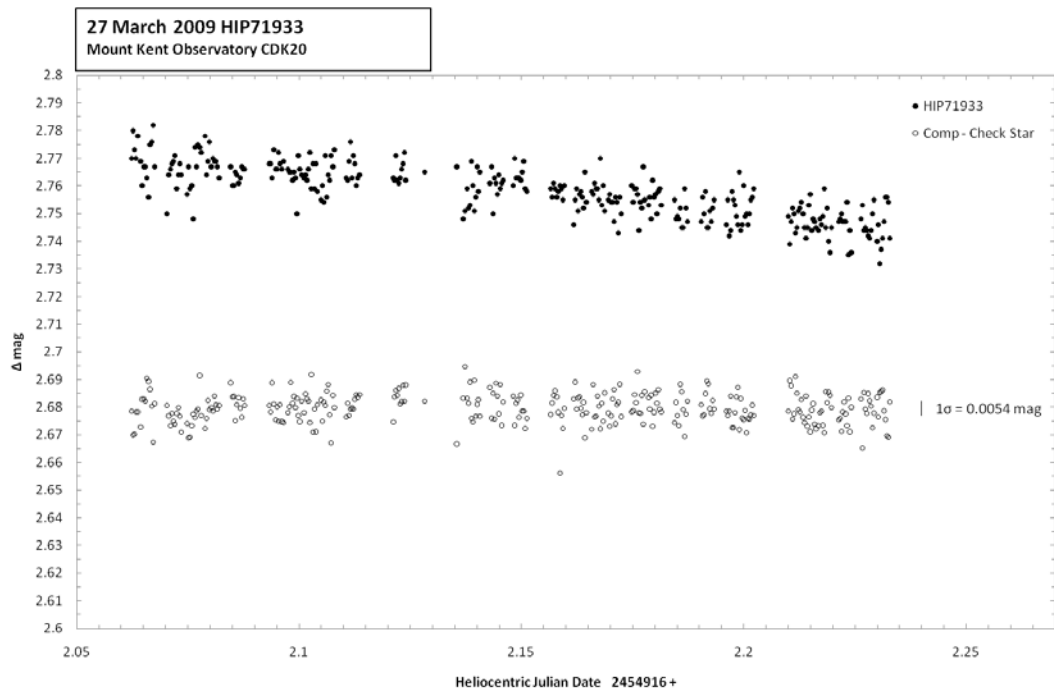


Figure 3.7 Spotted star HIP71933 - 27 March 2009

This light curve was derived from observation made using the MKO CDK20 telescope on 27 March 2009.

3.6 Spotted star HIP93378

The third target used to assess the photometric performance of the CDK20 telescope was spotted star HIP93378, magnitude 8.5 (V) and spectral type G5V. As per the previous star spotted target, HIP71933, this pre-main sequence star was chosen for observation because its rotation period is a required input for the ZDI research being conducted by Ian Waite and others at USQ. The observations were made using the MKO CDK20 by the author (3 July 2010) and Dr Rhodes Hart (27 June 2010).

Table 3.5 provides colour and magnitude data for the target, comparison and check stars used in the photometry analysis. The check stars listed in the table were combined into a new synthetic check star. The average ADU count achieved for the target was ~30,000.

Table 3.5 HIP93378 comparison and check stars

Star	Type	B-V	Magnitude
1	Target	0.63	8.5
2	Check	0.63	11.2
3	Check	0.85	11.4
4	Check	0.82	11.35
5	Check	0.60	10.75
6	Comparison	0.57	9.1

Figure 3.8 shows the relative positions of these stars.

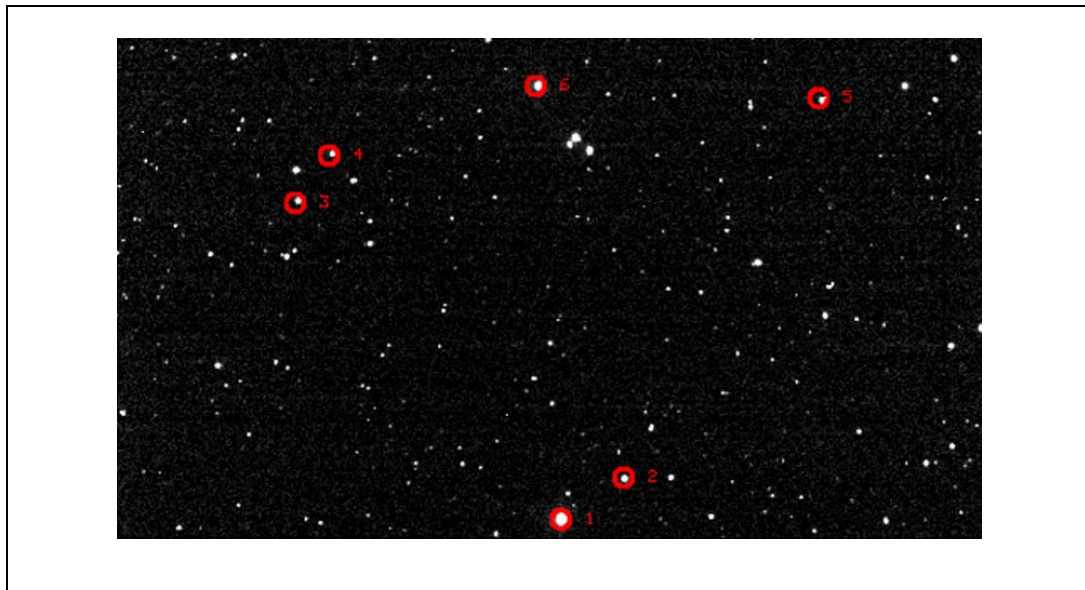


Figure 3.8 HIP93378 star identification frame

This frame shows the target HIP93378 labelled (1), the comparison star labelled (6) and the check stars (remaining numbered stars) used for the analysis.

The objective of observing this star was to demonstrate that the CDK20 telescope is capable of detecting the intensity variation caused by the presence of star spots on a rapidly rotating target. Observations were made over two nights and the resulting light curves are shown in [Figure 3.9](#) and [Figure 3.10](#). Unfortunately, the nights were not consecutive due to poor weather conditions. For both nights, a partial light curve was evident in the analysed data showing that the star's brightness variation is at least 0.04 magnitudes. There were insufficient observations to plot an entire cycle of the variation or for the IRAF Phase Dispersion Minimisation tool to extract a rotation period for the star. Again, the [Hipparcos Epoch Photometry Search Facility](#) was used to view the photometry data collected by the Hipparcos Mission for this target. Whilst some photometry data were available, not enough data points were present to determine a period. Further observations of this target are required to determine a robust period estimate.

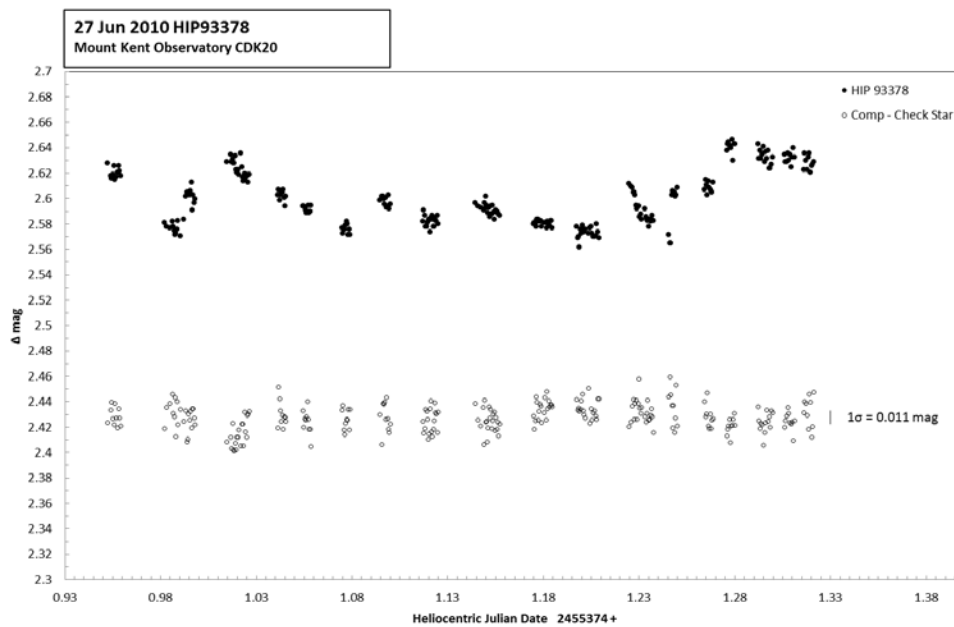


Figure 3.9 Spotted star HIP93378 - 27 June 2010

This light curve was derived from observation made using the MKO CDK20 telescope on 27 June 2010.

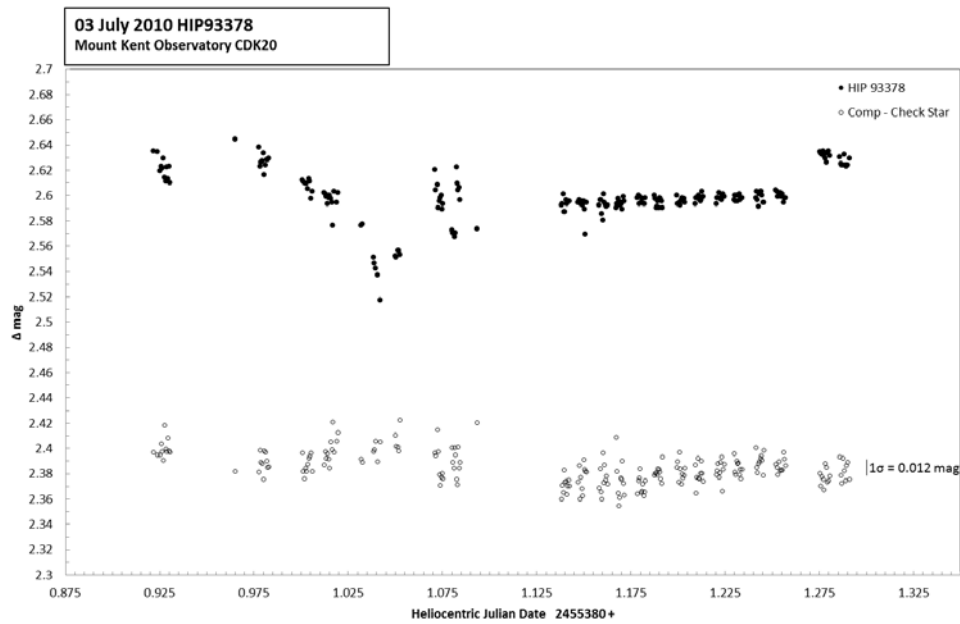


Figure 3.10 Spotted star HIP93378 - 03 July 2010
This light curve was derived from observation made using the MKO CDK20 telescope on 03 July 2010.

3.7 WASP 12b exoplanet transit

The fourth target observed was exoplanet WASP12b which has a known transit depth of 14mmag (Hebb et al. 2009) providing an opportunity to demonstrate the photometric performance of the CDK20 telescope through detection of such a small magnitude variation.

This exoplanet was discovered by the Wide Angle Search for Planets (WASP) team and has a known orbital period of 1.091 days and a mass 1.4 times that of Jupiter. It orbits WASP12, a magnitude 11 yellow dwarf star located approximately 600 light years away in the constellation Auriga. WASP12 has a mass and radius similar to the Sun.

The ephemeris data shown in Table 3.6 below provides the expected transit start time, mid transit time and transit end time for WASP12b on the evening of 14 January 2010 (Transitsearch.org). All times in the following table are coordinated universal times (UT).

Table 3.6 WASP12b transit ephemeris data

Event	HJD	Year	Month	Day	Hrs	Min
Start Transit	2455210.70	2010	01	14	04	45
Mid Transit	2455210.76	2010	01	14	06	15
End Transit	2455210.82	2010	01	14	07	46

The observations were made by Professor John Kielkopf and Karen Collins at Moore Observatory Kentucky USA on behalf of the author. The Moore CDK20 telescope and the RC24 telescope were both used to observe the transit on the night of 14 January 2010. The aim of using two telescopes was to allow a comparative analysis to be made between the 50cm CDK20 and the larger 60cm RC24. The identification frame in [Figure 3.11](#) show the target, comparison and check stars used in the analysis.

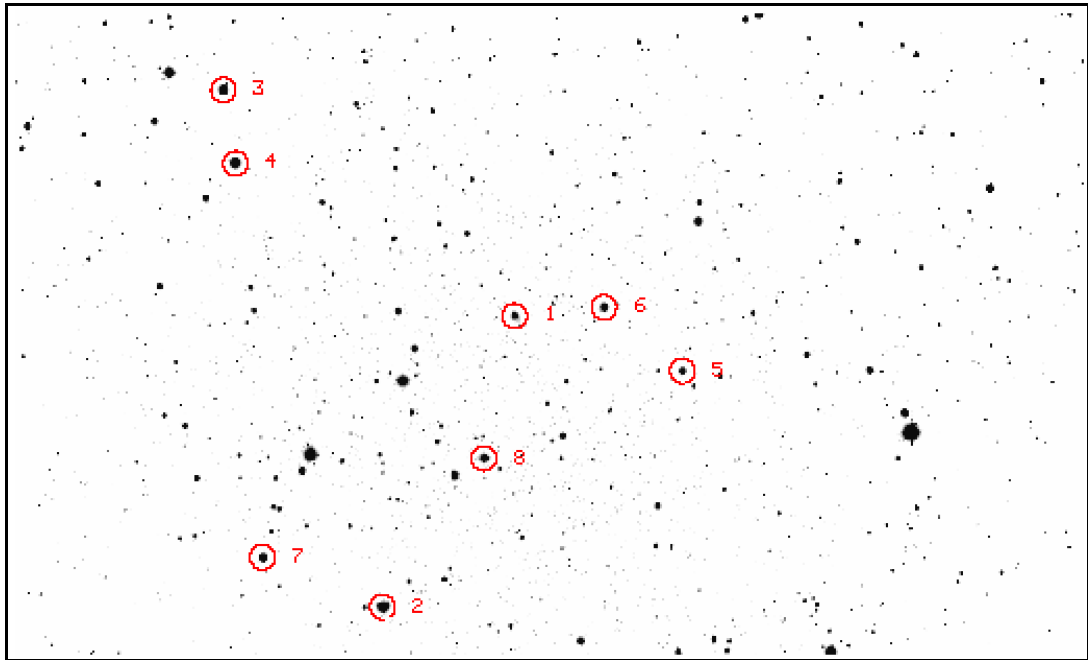


Figure 3.11 WASP12 star identification frame

This figure shows the identification frame from the CDK20 telescope. The target, WASP12, is labelled (1), the comparison star is labelled (4) and the remaining numbered stars were the check stars used for the analysis. A similar frame was produced for the RC24 telescope data.

[Table 3.7](#) provides data on the comparison and check stars used. The check stars listed in the table were combined into a new synthetic check star.

Table 3.7 WASP12 comparison and check stars

Star	Type	B-V	Magnitude
1	Target	0.54	11.6
2	Check	1.39	10.6
3	Check	0.98	10.5
4	Comparison	1.36	10.5
5	Check	1.17	11.5
6	Check	0.13	11.5
7	Check	0.29	12.9
8	Check	0.44	11.7

A slightly different image calibration procedure was used for processing the WASP12b data from the CDK20n and RC24 compared to the E2-Region and HIP71933 data analysis. For the WASP12b observations, a set of bias frames and dark frames were taken but no flat fields were recorded. The ADU count achieved for the WASP12b observations was generally around 15,000.

The resulting light curve for the WASP12b transit using the CDK20n telescope is shown in [Figure 3.12](#). It should be noted that during the time period between HJD 2455210 $\sim +0.72$ and $\sim +0.76$ no images were collected due to the telescope mount requiring a meridian flip. Also of note is an upward trend for both the (target-comparison) and (comparison-check) data. Although a possible explanation for this trend is non-linearity in the CCD, a correction can be applied in order to match the pre and post transit stellar brightness by fitting a trendline.

A second plot of the data was thus produced in which the general positive trend was removed. This was achieved by fitting a straight line to the pre and post transit data ([Figure 3.12](#)) to determine a gradient which was then used to correct the light curve ([Figure 3.13](#)).

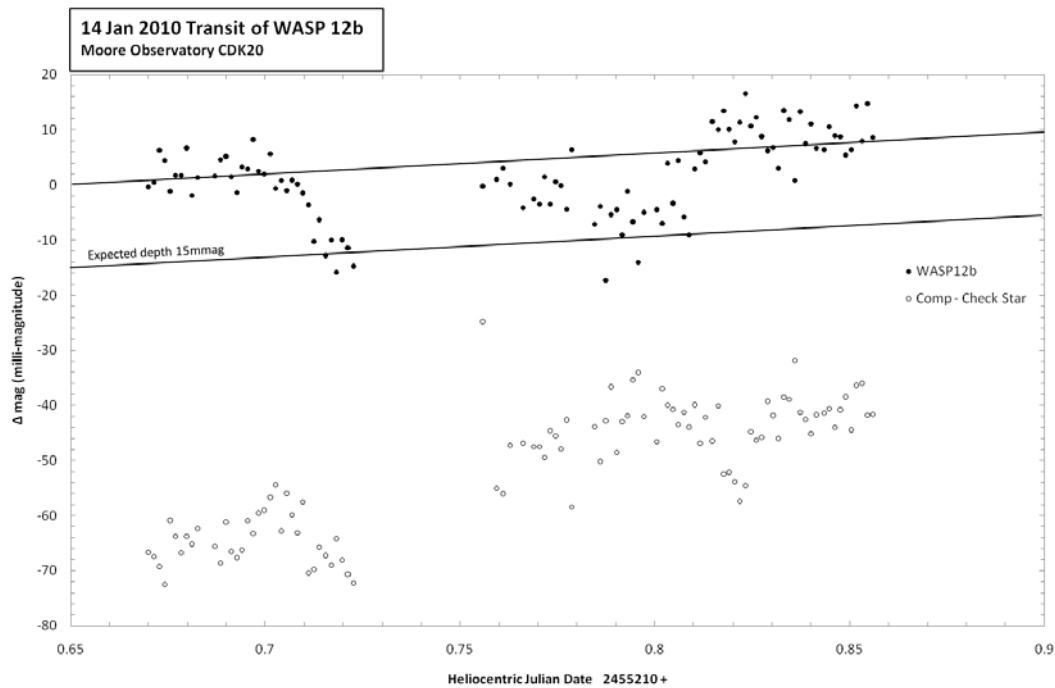


Figure 3.12 Raw WASP12b transit light curve (CDK20n)
This light curve was derived from observations from the Moore Observatory CDK20 telescope.

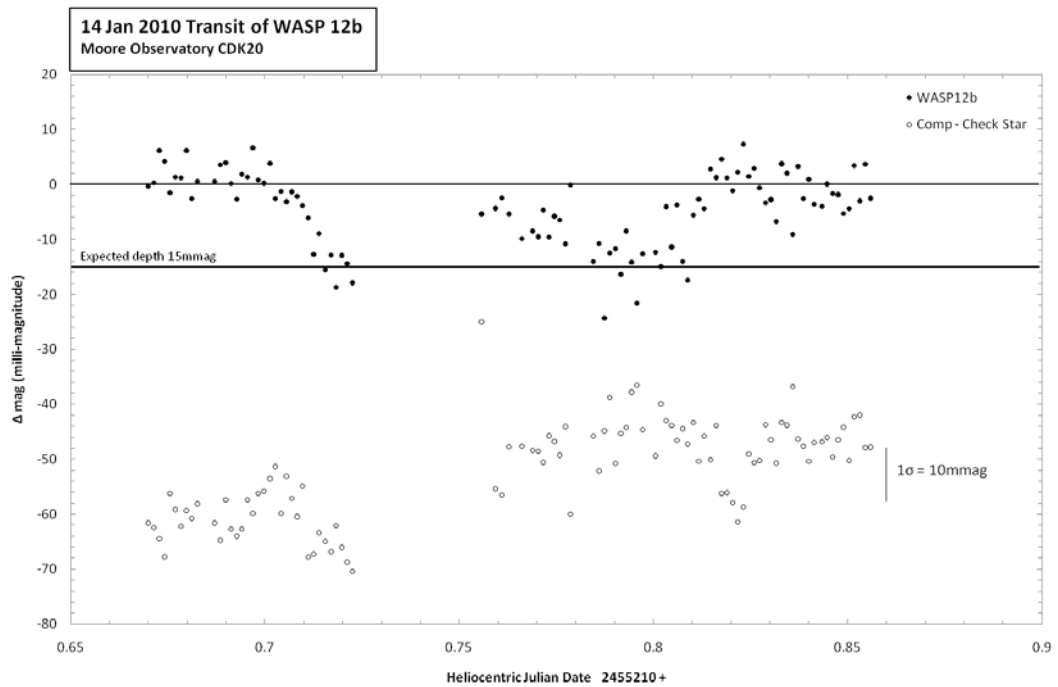


Figure 3.13 Corrected WASP12b transit light curve (CDK20n)

This light curve has been corrected to remove a trend between pre and post transit stellar brightness.

Examination of the plot reveals the presence of a transit event with a depth and duration corresponding with the ephemeris data for WASP12b provided in [Table 3.6](#).

For comparative purposes, the same transit event was observed in parallel with the Moore Observatory RC24 telescope. The resulting light curve, shown in [Figure 3.14](#), did not display the same upward trend that was observed in the CDK20n data. The transit depth and duration again correlate well with the predicted ephemeris and the noise is significantly less in the RC24 data compared to the CDK20n data. Of note is the improved consistency between the CDK20n and RC24 observations prior to the meridian flip that was required for the CDK20n telescope. [Figure 3.15](#) compares the light curve for the transit from RC24 and CDK20n telescopes, and indicates the improved results from the RC24 compared to the CDK20n, despite the fact that the signal to noise ratio obtained using these telescopes is similar. In particular the bump seen in the CDK20 data but not in the RC24 data is almost certainly due to a meridian flip, a shift in the star's position on the CCD, and the resultant effects on images that have not had the benefit of flat field calibration.

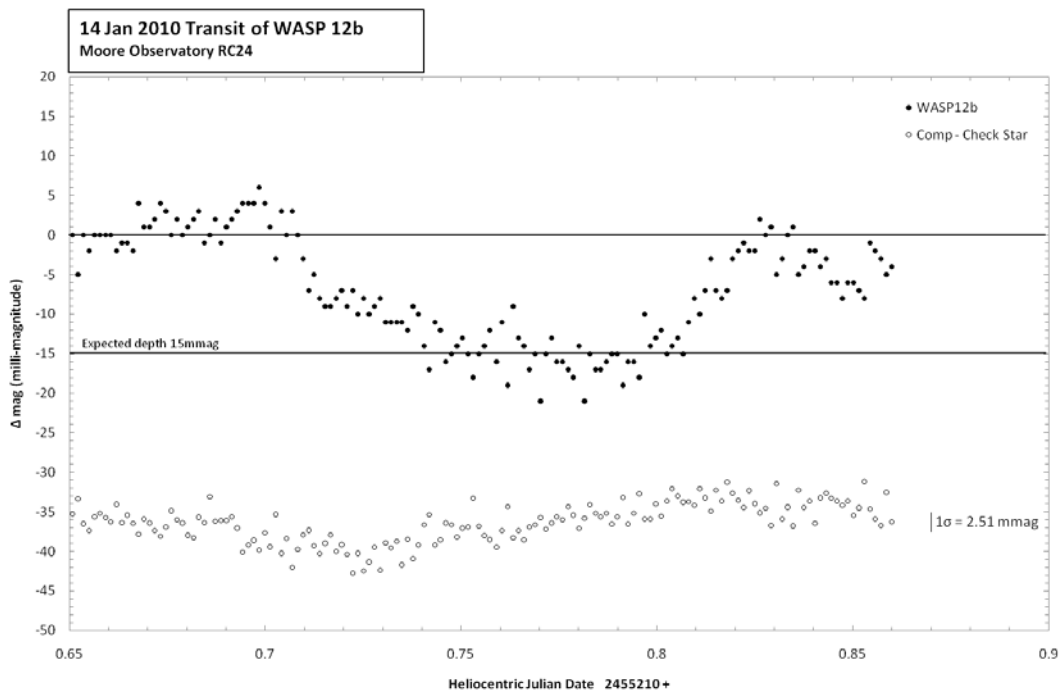


Figure 3.14 Exoplanet transit light curve of WASP12b (RC24)
This light curve was derived from observation from the Moore Observatory RC24 telescope.

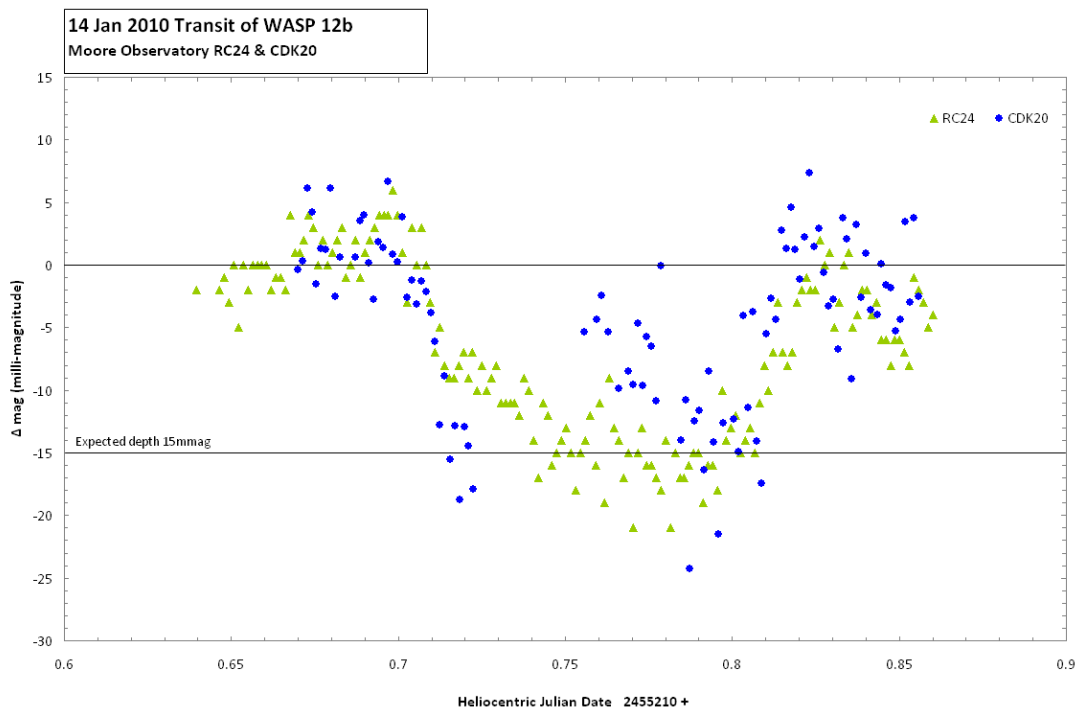


Figure 3.15 Exoplanet transit light curve of WASP12b (RC24 & CDK20n)
This light curve compares observations of the WASP12b transit from Moore Observatory's RC24 and CDK20n telescopes. A common scale was established using the pre transit observations.

Chapter 4: Discussion

4.1 Introduction

This chapter provides an interpretation of the light curves and other results that were presented in the preceding chapter and discusses use of the telescopes for star spot photometry and exoplanet transit work.

4.2 Requirements for star spot imaging

A key requirement for star spot imaging is the ability to monitor a star throughout the night for many nights. This means that the telescope needs to be scheduled for dedicated observation of a target and its comparison and check stars for as long as necessary to obtain complete rotational phase coverage of a spotted star to determine its rotation period. Additionally, long term monitoring of a target opens up the possibility of studying differential rotation and active longitudes on stars. Examples of spot monitoring programs are those of [Rodono et al. \(1995\)](#), [Henry et al. \(1995\)](#) and [Strassmeier et al. \(2010\)](#). On the assumption that the CDK20 telescopes can operate robotically over long time periods (weeks to months), there appears to be no reason why these telescopes cannot be of particular use for such studies.

The use of telescopes at different locations (e.g. CDK20n and s) gives an observer the opportunity to take advantage of the longitude difference to monitor star spot activity and measure the period of spotted stars at low or modest declinations, including the study of stars with rotation periods close to one day, as is possibly the case for HIP71933 and HIP93378. Coordinated use of the CDK20 telescopes thus should find use in these respects.

Photometric precision is the other key requirement for successful star spot photometry. Although many active stars undergo spot modulation of ~ 0.1 magnitude, it is still important to achieve the highest precision possible to accurately measure rotation periods and to maximise the improvement of Doppler imaging maps of mid and low latitude spot features. A precision of a few percent of a magnitude is required for this type of work.

4.3 Requirements for exoplanet transit studies

The photometric precision required for exoplanet work is characteristically much more stringent than for star spot studies. Practitioners in the field of exoplanet photometry typically deliver milli-magnitude precision and a review of the [Transitsearch.org](#) candidate page indicates that a precision of $\sim 3-5$ mmag is required for exoplanet transit work.

The temporal coverage for a transit can vary, but at least some targets of interest can have their transit measured in one night. The use of two telescopes at different longitudes (e.g. CDK20n and s) opens up the possibility of monitoring transit events for equatorial stars that last more than one night and allows for independent checks on the reality of features.

In terms of scheduling, it is vital that the chosen robotic telescope be brought to bear on the target as required and to cover the complete transit event including the ingress, egress and out-of-transit times in order to calibrate the light curve properly.

4.4 Performance of the RC24 telescope

The light curve shown in [Figure 3.14](#) demonstrates that the RC24 telescope at Moore Observatory is capable of exoplanet studies. Thus this telescope should be made available for further transit studies as soon as possible, ideally as a remotely operable robotic telescope.

The results presented in this thesis also suggest that the RC24 performance can be enhanced if close attention is paid to flat fielding issues.

4.5 Performance of the CDK20 telescopes

The CDK20n data demonstrates this telescope's usefulness in detecting exoplanet transits. However, at present the telescope is likely to be limited by a combination of tracking imperfections, the necessity to manage meridian flips, and a paucity of flat field calibration frames. It is also worth noting that the choice of star and sky apertures can influence the precision of the resulting light curve.

Nevertheless, the CDK20n telescope appears more than adequate for some types of star spot work, especially the determination of rotation periods for potential ZDI targets where this information is currently lacking.

As demonstrated in [Chapter 3](#), the CDK20s telescope appears capable of star spot photometry.

The E-Region observations presented in this thesis indicate that differential photometry with a standard deviation of 4 mmag can be achieved on a single night for a 7th magnitude star with 10s exposures. Although such precision cannot be expected across a series of nights, this suggests that useful star spot photometry with a precision of a few percent can be performed for ZDI targets if due attention is paid to calibration of the observations. While presently limited by the lack of data, the light curve results for HIP71933 and HIP93378 further suggests that star spot photometry can be performed with this telescope.

Given that the CDK20n and CDK20s telescopes are functionally identical, and given the encouraging results for the transit of WASP12b with the CDK20n telescope, it is reasonable to expect the CDK20s to be useful for exoplanet transit work, especially if close attention is paid to tracking, flat fielding and signal to noise issues, and recovery from meridian flips is made as fast and as accurately as possible in terms of placing the target star image back on the same set of CCD pixels.

4.6 Prospects for the CDK700 telescope

The CDK700 due for commissioning at MKO later in 2010 offers several potential advantages for precision stellar photometry:

- 1) An alt-azimuth design with an image de-rotator, the CDK700 will not suffer a meridian flip problem, though care will be required to avoid observing targets at the zenith due to the singularity present in the telescope's motion.
- 2) The 0.7m aperture of the telescope combined with a high efficiency Apogee U9000 CCD should deliver photon counts comparable to the RC24. Thus it is reasonable to expect the photometric performance of the CDK700 to be potentially as good as, if not better than, the RC24.
- 3) The new telescope will have a control system which allows considerable flexibility in operation thanks to the use of an open-source software approach. When coupled with the software being developed for the robotic operation of the CDK20 telescopes, it is expected that the CDK700 will operate as a robotic photometry telescope leveraging off the software development currently underway for the CDK20 telescopes.
- 4) Finally, it is noted that the dual Nasmyth focus provided by the CDK700 allows for convenient coupling of the telescope with a fibre fed spectrograph. Such a spectrograph has been developed by the UoL and may one day offer the possibility of robotic spectroscopy in addition to robotic photometry.

4.7 O'Mara robotic telescope

Consideration of the O'Mara telescope at MKO is beyond the scope of this thesis, and forms the basis of a Masters thesis study by Scott Sinclair. However, it should be noted that in its present form the O'Mara telescope's 0.3m aperture provides a significant limitation on the faintest targets that can be observed for star spot and exoplanet studies. The O'Mara telescope is also based partly on commercial software, as opposed to the open-source approach taken for the Shared Skies Partnership. Thus the O'Mara telescope's design and operation is currently dedicated to routine undergraduate imaging studies rather than post graduate research projects which may require software modifications to meet specific requirements.

4.8 Photometric precision of the MKO & Moore telescopes

Overall, the photometry results indicate that the MKO and Moore Observatory telescopes are capable of achieving precision photometric performance suited to scientific research. However, the quality of the results depends strongly on how the observations are made. Specifically, it is important to:

- 1) Obtain good quality calibration frames including bias, darks (or combined bias and dark frames) and flat field frames. Bias frames should have a very low noise; this is achieved by combining many frames. Dark frames are important if there is a significant source of thermally generated electrons, as can be the case for thermoelectrically cooled CCDs used with robotic telescopes. Flat field frames should have a extremely high signal to noise ratio because the target frames are divided by them.
- 2) Use an appropriate exposure time to ensure the target creates a high photon count without causing saturation. The optimal exposure time represents a balance between achieving a high signal to noise ratio and, at the same time, staying within the linear range of the CCD.
- 3) Make many observations to combat shot noise and obtain appropriate temporal coverage as needed. When frames are combined, the signal to noise ratio will rise by the square root of the number of frames, due to shot noise.

For more references on the complexities of CCD photometry and noise reduction, the reader is referred to [McLean \(2008\)](#).

A full set of calibration frames were obtained for all of the MKO observations made for this thesis. The subsequent processing of these frames using IRAF revealed patterns in the bias frames and unwanted hot pixels and columns in the dark frames which were subsequently removed from the science frames thus improving the precision of the final photometric measurements. Similarly, the flat field frames were used to remove the effects of dust and other obstructions in the optical path of the telescope that leave unwanted aberrations in the science frames if not addressed.

The photometric results for Graham's E2-Region indicate the importance of achieving a high ADU count for the target to ensure that the best possible signal to noise ratio is obtained. [Figure 3.4](#) demonstrates that the error builds exponentially with increasing magnitude for a constant ADU count. Applying this knowledge to the WASP12b data obtained from the Moore Observatory CDK20 in which an ADU count was only $\sim 15,000$, better photometric precision would have been obtained if the exposure time had been increased to achieve a higher ADU count for the target. If the ADU count was increased to $\sim 40,000$ by increasing the exposure time, it is estimated that the photometric precision would appreciably increase making the resulting light curve less noisy and more like that achieved for the RC24 telescope as shown in [Figure 3.14](#). In a similar manner, the ADU count of the WASP12 target using the RC24 telescope was also only $\sim 15,000$. Again, the photometric precision would increase if the ADU count were increased.

4.9 Data quantity & processing

Numerous observations were made during each observation night which, when taken as a set, reduce the noise in the resulting light curve. On a typical observation night, between 100 and 500 science frames were taken requiring up to 6GB of storage. These data were transferred using a number of methods including electronic file transfer via the internet; copying the data to a USB drive and physically posting the drive; and by recording the data to DVDs and physically posting the DVDs. Whilst the electronic file transfer was convenient and relatively fast, it required a significant amount of bandwidth as mentioned in section 2.4.3. On the other hand, physically copying the data to a USB or DVD and mailing it was a slow and more labour intensive activity.

Based on the experience gained in collecting the observations for this thesis, the use of the Internet for both controlling the telescope and subsequently accessing the large quantity of observations is the most viable and efficient method available.

IRAF was used to perform all of the image processing and for making the photometry measurements. Microsoft Excel[®] was used to process the photometry measurements and generate the light curve plots. IRAF is a well known and trusted application in the astronomical community but it is a difficult application to install and use effectively, especially for a student or researcher without prior experience. However, once the basic operations are learned and the user becomes familiar with the general philosophy behind the interface and the various tasks, IRAF becomes a powerful and robust tool.

This page is intentionally blank.

Chapter 5: Conclusions

5.1 Introduction

This thesis has demonstrated the effectiveness of stellar photometry using telescopes at MKO and Moore Observatory. As a pair of identical telescopes separated in longitude, the Corrected Dall-Kirkham 50cm/20-inch telescopes installed at MKO and Moore Observatory as part of the Digital Science Partnership offer observing projects that require all-sky access and continuous observing for many hours. The RC24 at Moore Observatory and the forthcoming CDK700 for MKO additionally provide instruments for more challenging stellar photometry projects.

The results of this thesis suggest that the telescopes at MKO and Moore Observatory can be used for star spot studies in support of ZDI research or more generally in cool-star studies. Depending on the target to be studied, the level of precision required and the location of the star in the sky, the combination of the two observatories offers a choice of telescope in aid of this work.

The RC24 data from Moore Observatory demonstrate that the milli-magnitude photometry of exoplanet transits can now be performed for the Shared Skies Partnership. The CDK20n data are encouraging in this respect but in future it will be important to address issues such as telescope tracking, data loss due to meridian flip, flat fielding and aperture photometry procedures in order to maximise the usefulness of the observations. By the same token, success with the CDK20n should readily translate to the CDK20s telescope, suggesting the CDK20s at MKO can be used for exoplanet transit studies on a regular basis if the telescope is operated robotically. In particular, the standard star data obtained with the CDK20s telescope suggest that photon limited performance is a realistic aim.

The forthcoming CDK700 offers the prospect of precision robotic photometry of spotted stars and exoplanet transits, making use of its substantial aperture and research grade Apogee CCD camera. By incorporating the robotic telescope software being developed for the CDK20 telescopes into the CDK700 system, it should be possible to regularly deliver precision robotic photometry of spotted stars and exoplanet transits for a range of postgraduate student and staff research projects.

It is concluded that publishable scientific stellar photometry results can be obtained using the existing and future telescopes at MKO, as well as from Moore Observatory. However, general use must wait until the implementation of robotic telescope operation including development of a user friendly remote interface to the telescopes for research students and others and the ability to automatically process and archive the raw observations at the observatory to avoid any requirement to download large amounts of raw data over the internet.

5.2 Recommendations

5.2.1 Remote telescope operation

A well recognised rule relating effort to results is commonly known as the 80/20 rule or more formerly as the Pareto Principle after the Italian economist Vilfredo Pareto. He observed that in most activities, a small fraction (20 percent) of the total activity accounts for a large fraction (80 percent) of the results. This rule relates to robotics in which the automation can handle the 80% of the task that is easy, and human intervention can cover the remaining 20% that is difficult (Stentz 2001). This rule would appear to find application with robotic telescopes, where the majority of the task is in making the observations (which is relatively easily automated), but with the remaining work (the data processing including activities such as field identification), being difficult to automate.

From a student and researcher's perspective, the following aspects should be noted prior to undertaking remote observations:

- 1) At the time of writing this thesis, the MKO and Moore Observatory CDK20 installations did not have the capability to automatically process any of the raw observations. Hence, the user is required to download the data and undertake the processing off-site. To achieve this in the most time efficient manner, the user is required to have a broadband internet connection. The exact quota required depends on the number of observations planned and the frequency of observing sessions.
- 2) The results of this thesis highlight the need to obtain a high photon count and hence high signal to noise ratio for the target star, whilst ensuring that the CCD is not saturated. Noise from the sky background, dark current and CCD readout process should be minimised by using calibration frames so that the most significant noise contribution comes from the source itself (shot noise). When this is achieved, the signal to noise ratio can be approximated as the square root of N , where N is the photon count. The observations made for this thesis achieved ADU counts of about 40,000. Multiplying this by the gain of the CCD and adjusting for the quantum efficiency of the detector results in a photon count of about 112,000. The signal to noise ratio, being the square root of this figure comes to over 300, which is considered very good (Howell 2006).
- 3) Calibration frames should be made for every observation night to help reduce the noise in the final photometry results. As a minimum, it is recommended that bias and dark frames (either separate or combined) should be made and flat field frames taken. The time taken to make these observations will be well spent, especially when undertaking exoplanet transit work.
- 4) Use of the RC24 telescope at Moore Observatory for transit studies is to be encouraged, especially as a remotely operable robotic telescope.

5.2.2 Future development & work activities

It is recommended that:

- 1) The Shared Skies Partnership focus on web-based delivery of imaging and data analysis as the way to most readily share all aspects of the observing and data reduction process.
- 2) The MKO and Moore Observatory CDK20 telescopes be further developed to full robotic capability to allow distance education students and researchers access to the facilities without any requirement for human intervention at the telescopes.
- 3) Consideration be given to use of the CDK20 telescopes under the MicroFUN project.
- 4) USQ and UoL prepare a standard software suite for astronomy students and researchers. Such a suite would include an IRAF installation CD including installation instructions, an open source planetarium application and specific photometry resources. Alternatively, the software suite could be made available on a university server so that students can remotely access the server and run the applications. The software suite would allow students and researchers to spend more time focusing on the astronomy and less time on the IT aspects. It is recognised that any such software suite would still require the end-user to have a linux distribution installed.
- 5) A data processing capability be developed to process the raw stellar observations collected on a given evening. Such processing would be specified by the user and include:
 - a) Generation and retrieval of a master bias frame.
 - b) Generation and retrieval of a master dark frame.
 - c) Generation and retrieval of a master flat frame for each filter.
 - d) Application of the master frames to the science frames.
 - e) Updating of the science frame headers to record user specified keywords such as UT, HJD and AIRMASS.
 - f) Rotation of the science frames for observations made after a meridian flip.
 - g) Alignment of all the science frames such that the x,y position of any given star is the same for all science frames collected on that evening.
 - h) Inclusion of a world coordinate system into each science frame.
 - i) Identification of target, comparison and check stars. The 80/20 rule has application here and should be carefully considered (Refer section [5.2.1](#)).
 - j) Aperture photometry measurements of selected stars.

- k) Generation and retrieval of a light curve using the current evening results.
- l) Combining of the data with results from previous evenings.
- m) Generation and retrieval of a combined data light curve.

5.3 Thesis summary

It is a long road between the concept of robotic photometry and its fruition. This thesis confirms the capability of MKO and Moore Observatory telescopes for precision stellar photometry. The implementation of fully robotic operation of these telescopes is the next significant activity to be undertaken so that postgraduate students and others working remotely can realise the full potential of these telescopes.

Appendix A Differential photometry

A1 Introduction

Although the photometry performed for this thesis is single colour work, star spot and other photometry is sometimes performed using multiple colours. Hence the following procedure for doing photometry with multiple colours has been included. The material presented in this Appendix has been derived from [Henden & Kaitchuck \(1990\)](#).

A2 First order extinction

To properly cater for the atmospheric effects, it is necessary to correct the measured magnitudes and colour indices to a location above the Earth's atmosphere by determining and applying extinction coefficients. It is worth noting here that if All Sky Photometry is to be performed, then another correction, in addition to the extinction correction, would need to be applied to take the above atmosphere values to a standard system.

Traditionally, extinction coefficients are determined for every observation run (being a single night of observation). The process for determining the coefficients is to observe standard stars in various colours and to then plot the known colour index against the measured colour index to obtain a straight line curve, the slope of which is used to calculate the extinction coefficient for a particular filter. This can be very time consuming and can easily rob the observer of valuable time that could be spent measuring the target.

However, it is possible to obtain accuracies in the order of 5 mmag by using assumed values for extinction ([Warner 2006](#)). For sites at an elevation of 1500ft (457m) above mean sea level or higher such as MKO, a good assumed value for the V coefficient is 0.3. For sites lower than this a good value is between 0.35 and 0.4 and for high altitude and dry sites a good value would be 0.2. The extinction coefficients for colours other than V are offsets from the V coefficient. For the B filter, the extinction coefficient is 0.13 higher than V and for the I band, the coefficient is 0.08 lower than V ([Berry & Burnell 2009](#)). [Table 5.1](#) provides a summary of these coefficient estimates.

Table 5.1 Approximations for extinction coefficients

Location	V	B	I
Sea level	0.35 - 0.40	0.48 - 0.53	0.27 - 0.32
<1500ft	0.30	0.43	0.22
High & Dry	0.20	0.33	0.12

If accuracies in the order of 0.005 magnitudes are sought, then observations should be made no lower than 50° elevation when using assumed extinction coefficients (Warner 2006). This allows for a tolerance on the assumed extinction coefficient of approximately 0.5. For comparison, if accuracies in the order of 0.01 magnitudes are sought, then observations should be made no lower than 40° elevation.

The following procedure is used to determine the extinction coefficient:

- 1) Observe any stars over a large range of air masses (for example, $X=1$ to $X>2$). Preference should be given to observing Landolt standards with small (B–V). Observe through UBVRI filters.
- 2) Calculate the instrumental magnitudes for each filter using the following equations:

$$v = -2.5 \log (d_v) \quad \text{Equ (1)}$$

$$b = -2.5 \log (d_b) \quad \text{Equ (2)}$$

$$u = -2.5 \log (d_u) \quad \text{Equ (3)}$$

$$r = -2.5 \log (d_r) \quad \text{Equ (4)}$$

$$i = -2.5 \log (d_i) \quad \text{Equ (5)}$$

where $d_v = (\text{counts/sec} - \text{sky background})$ for the V filter.

- 3) The 1st order extinction coefficients may be determined by plotting the following parameters then fitting a straight line least squares fit to the data:

$$v \text{ versus } X \quad \text{The slope} = k_v'$$

$$b \text{ versus } X \quad \text{The slope} = k_b'$$

$$u \text{ versus } X \quad \text{The slope} = k_u'$$

$$r \text{ versus } X \quad \text{The slope} = k_r'$$

$$i \text{ versus } X \quad \text{The slope} = k_i'$$

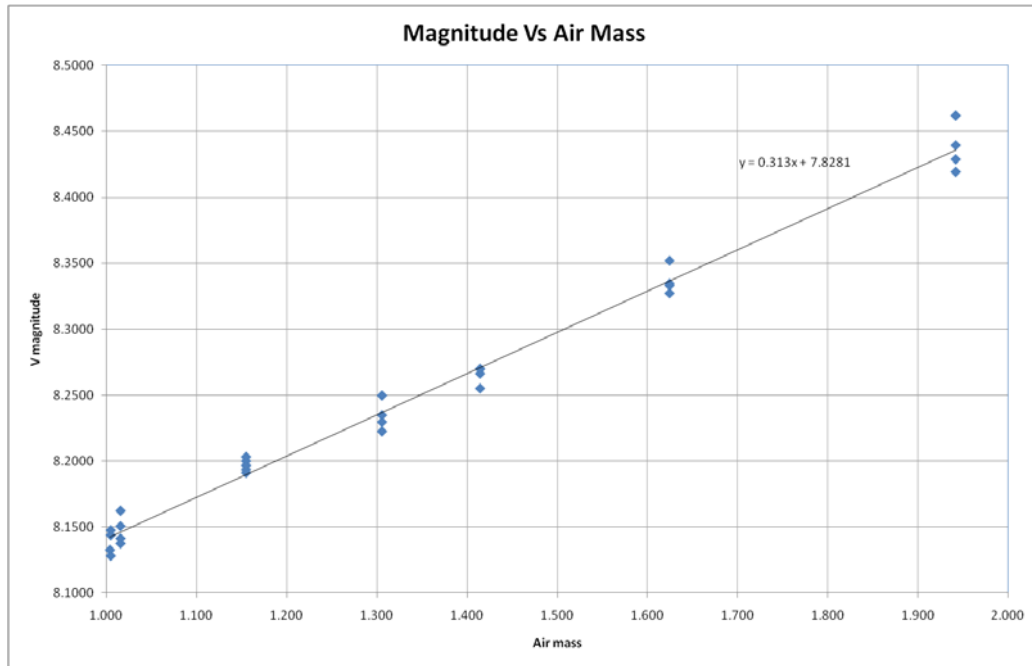


Figure A2.1 Example Magnitude Vs Air Mass plot

When the sky is transparent and colour-free, atmospheric extinction depends linearly on X , the air mass. The slope (or gradient) is used to determine the extinction co-efficients.

- 4) Once the extinction coefficients have been determined they may be used to correct the instrumental magnitudes for atmospheric absorption using the following equations:

$$v_o = v - k_v' \cdot X \quad \text{Equ (6)}$$

$$b_o = b - k_b' \cdot X \quad \text{Equ (7)}$$

$$u_o = u - k_u' \cdot X \quad \text{Equ (8)}$$

$$r_o = r - k_r' \cdot X \quad \text{Equ (9)}$$

$$i_o = i - k_i' \cdot X \quad \text{Equ (10)}$$

where:

v_o = instrumental magnitude through the V filter corrected for extinction (i.e. above atmosphere magnitude).

k' = principal (or 1st order) extinction coefficient.

X = air mass.

A3 Second order extinction

- 1) Observe a closely spaced red blue pair over a large air mass. i.e. very small air mass difference between the red and blue star. Warner (2006) defines a red star as

$(B-V) > 0.8$ and a blue star as $(B-V) < 0.1$. This need only be done yearly or when the system changes.

- 2) Calculate the difference in colour indices:

$$\Delta(b-v)_0 = \Delta(b-v) - k_{bv}' \cdot X \quad \Delta(b-v) - k_{bv}' \cdot (X_x - X_c)$$

where $(b-v) = -2.5 \log(C_b / C_r)$

C_b = Counts/s for blue star. Similarly for red star.

The term $[-k_{bv}' \cdot (X_x - X_c)]$ is dropped because it is assumed that the $(X_x - X_c)$ is 0.

- 3) Calculate coefficient by plotting:

$$\Delta(b-v)_0 \quad \text{Vs} \quad X \cdot \Delta(b-v) \quad \text{The slope is } k_{bv}'$$

A4 Transformation coefficients

- 1) Observe a set of standard stars in a cluster or Landolt field that is close to zenith. Use all filters. Observe at least 10 stars.

- 2) Calculate atmospheric instrumental magnitudes using:

$$v = -2.5 \log(C_v)$$

$$(b-v) = -2.5 \log(C_b / C_v)$$

$$(u-b) = -2.5 \log(C_u / C_b)$$

$$(v-r) = -2.5 \log(C_v / C_r)$$

$$(r-i) = -2.5 \log(C_r / C_i)$$

- 3) The magnitudes and colours are now corrected for extinction using:

$$v_0 = v - k_v' \cdot X$$

$$(b-v)_0 = (b-v) \cdot (1 - k_{bv}'' \cdot X) - k_{bv}' \cdot X$$

$$(u-b)_0 = (u-b) - k_{ub}' \cdot X$$

$$(v-r)_0 = (v-r) - k_{vr}' \cdot X$$

$$(r-i)_0 = (r-i) - k_{ri}' \cdot X$$

Note: $k_{bv}' = k_b' - k_v'$ etc.

- 4) Determine ε (transformation coefficient for v mag) and ζ_v (v filter nightly zero point):

$$V - v_0 = \varepsilon (B - V) + \zeta_v$$

$$\text{Plot } (V - v_0) \text{ Vs } (B - V)$$

$$\text{Slope} = \varepsilon$$

$$\text{Intercept} = \zeta_v$$

- 5) Determine μ (transformation coefficient for (b-v) colour index) and ζ_{bv} (zero point for (b-v) colour index):

$$(B - V) - (b - v)_0 = (1 - 1/\varepsilon).(B - V) + \zeta_{bv} / \mu$$

$$\text{Plot } (B - V) - (b - v)_0 \text{ Vs } (B - V)$$

$$\text{Slope} = 1 - 1/\mu$$

$$\text{Intercept} = \zeta_{bv} / \mu$$

i.e. $\mu = 1 / (1 - \text{slope})$

$$\zeta_{bv} = \mu \cdot \text{Intercept}$$

- 6) In a similar fashion, the remaining transformation coefficients can be found using:

$$(U - B) - (u - b)_0 = (1 - 1/\psi).(U - B) + \zeta_{ub} / \psi$$

$$(V - R) - (v - r)_0 = (1 - 1/T_{vr}).(V - R) + \zeta_{vr} / T_{vr}$$

$$(R - I) - (r - i)_0 = (1 - 1/T_{ri}).(R - I) + \zeta_{ri} / T_{ri}$$

Plots give transformation coefficients and intercepts (nightly zero points).

A5 Perform differential photometry

Normally differential photometry ends once Δv , Δb etc. have been calculated. These are the atmospheric instrumental magnitude differences. However, if the target and the comparison are separated by more than 1 deg then calculate the angular separation at which differential extinction effects start to interfere with the required precision. The results are the above atmosphere instrumental magnitude differences $(\Delta v)_0$, $(\Delta b)_0$ etc.

- 1) The magnitude difference between the target and the comparison star is corrected for extinction using:

$$\Delta v = -2.5 \log (d_{vx} / d_{vc})$$

$$\Delta b = -2.5 \log (d_{bx} / d_{bc})$$

$$\Delta u = -2.5 \log (d_{ux} / d_{uc})$$

$$\Delta r = -2.5 \log (d_{rx} / d_{rc})$$

$$\Delta i = -2.5 \log (d_{ix} / d_{ic})$$

Where d_{vx} = Target (counts/s – sky background)

d_{vc} = Comparison

Now:

$$(\Delta v)_0 = \Delta v - k_v' \cdot (X_x - X_c)$$

$$(\Delta b)_0 = \Delta b - k_b' \cdot (X_x - X_c)$$

$$(\Delta u)_0 = \Delta u - k_u' \cdot (X_x - X_c)$$

$$(\Delta r)_0 = \Delta r - k_r' \cdot (X_x - X_c)$$

$$(\Delta i)_0 = \Delta i - k_i' \cdot (X_x - X_c)$$

- 2) Calculate the colour index differences using:

$$\Delta(b - v)_0 = \Delta(b - v) - k_{bv}' \cdot (X_x - X_c) - k_{bv}'' \cdot \Delta(b - v) \cdot X$$

$$\Delta(u - b)_0 = \Delta(u - b) - k_{ub}' \cdot (X_x - X_c)$$

$$\Delta(v - r)_0 = \Delta(v - r) - k_{vr}' \cdot (X_x - X_c)$$

$$\Delta(r - i)_0 = \Delta(r - i) - k_{ri}' \cdot (X_x - X_c)$$

Where $k_{bv}' = k_b' - k_v'$ i.e. 1st order extinction coefficients. Similarly for others.

$k_{bv}'' = 2\text{nd order extinction}$

$k_{ub}'' = 0$ by definition¹

$k_{vr}'' = k_{ri}'' = 0$ assumed to be negligible

$X = \text{Average air mass}$

$$\Delta(b - v) = \Delta b - \Delta v$$

1. For a discussion of why this parameter is not always assumed to be zero, refer to Henden & Kaitchuck p98.

- 3) The above atmosphere instrumental magnitude differences and colour index differences can be transformed to the Johnson Cousins standard system as follows:

$$\Delta(B - V) = \mu \cdot \Delta(b - v)_0$$

$$\Delta(U - B) = \psi \cdot \Delta(u - b)_0$$

$$\Delta(V - R) = T_{vr} \cdot \Delta(v - r)_0$$

$$\Delta(R - I) = T_{ri} \cdot \Delta(r - i)_0$$

$$\Delta V = (\Delta v)_0 + \varepsilon \cdot \Delta(B - V)$$

- 4) If the comparison star has been standardised, the actual magnitude and colour of the target can be calculated as follows:

$$V_x = V_c + \Delta V$$

$$(B - V)_x = (B - V)_c + \Delta(B - V)$$

$$(U - B)_x = (U - B)_c + \Delta(U - B)$$

$$(V - R)_x = (V - R)_c + \Delta(V - R)$$

$$(R - I)_x = (R - I)_c + \Delta(R - I)$$

Where ΔV , $\Delta(B - V)$ etc. are averaged values.

This page is intentionally blank.

Appendix B E2-Region photometry results

Photometry of 10 standard stars from Graham's E2-Region has been performed. The main results are presented in Chapter 3. This Appendix provides the light curve results for all 10 standard stars. All plots are presented with the same scale for ease of comparison.

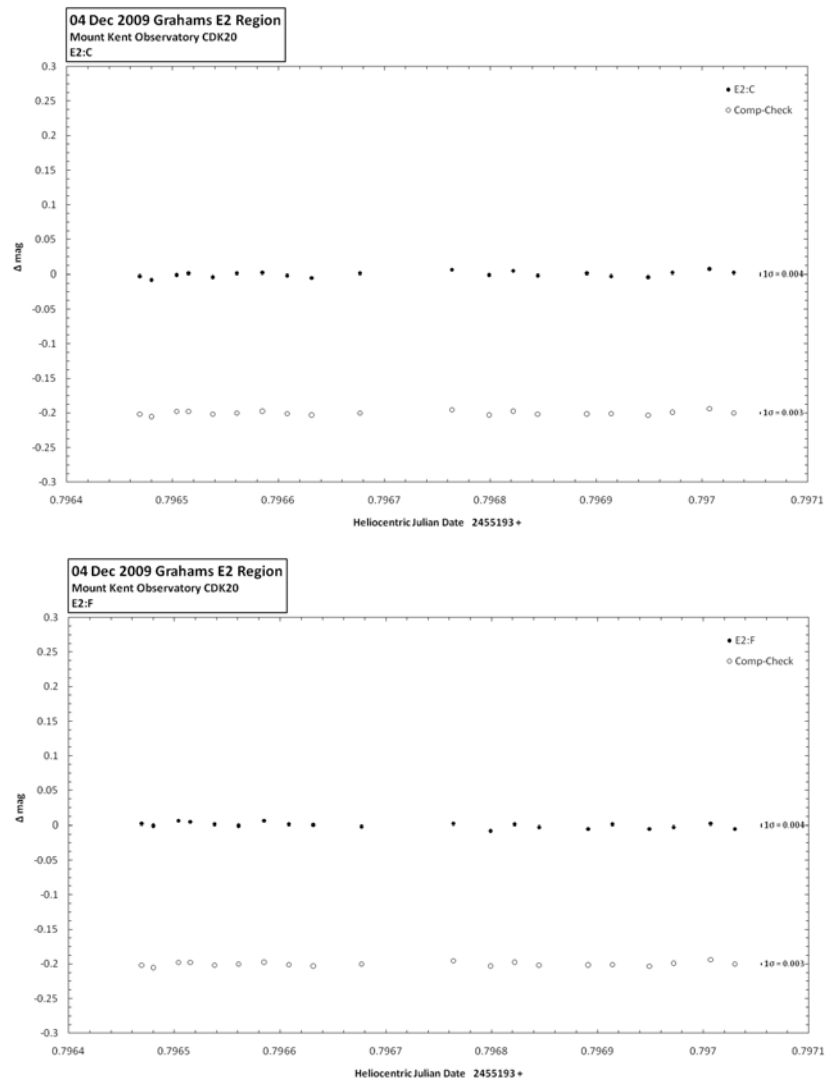


Figure B0.1 Graham's E2-Region standard star light curves - set 1/4

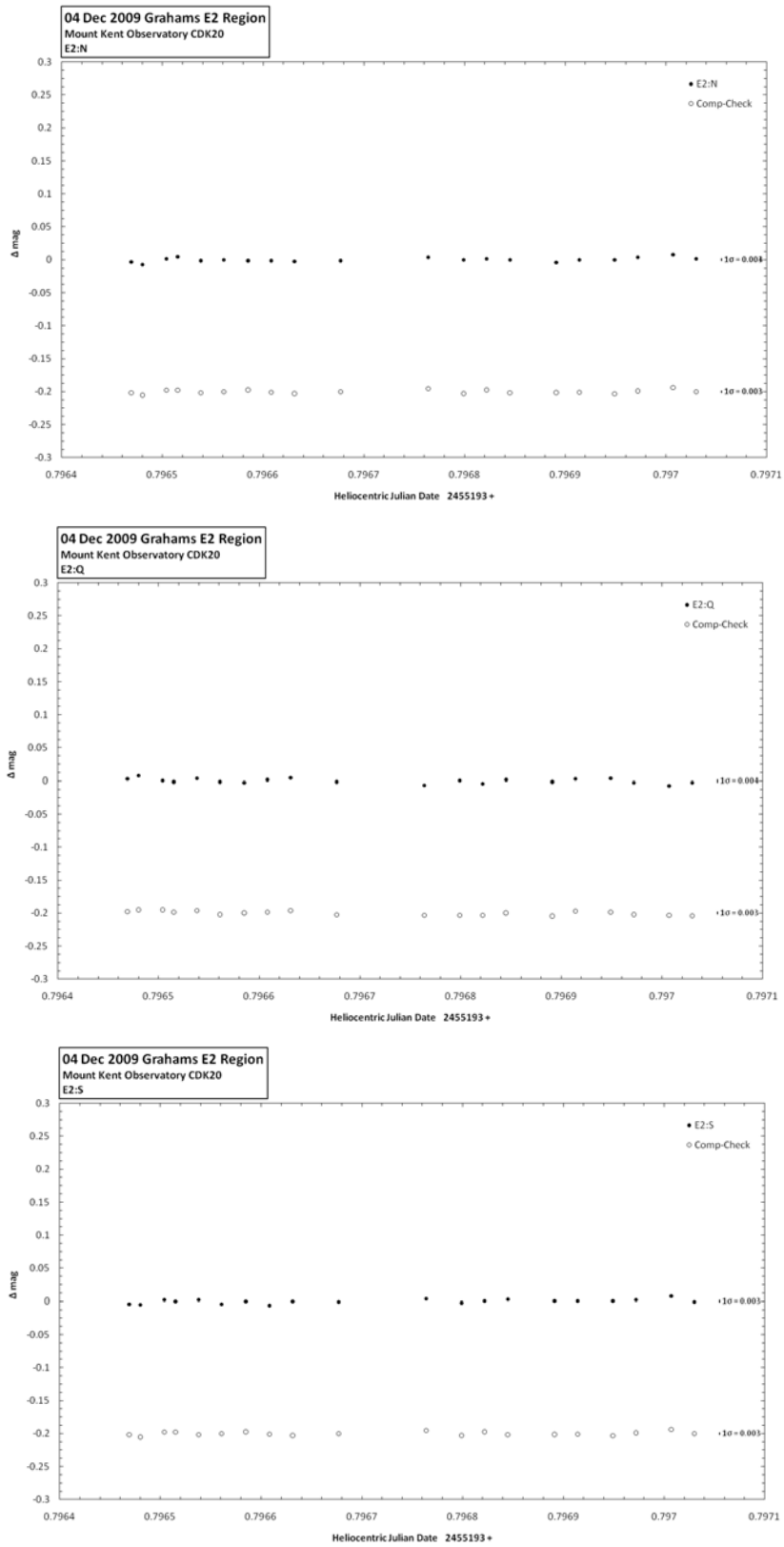


Figure B0.2 Graham's E2-Region standard star light curves - set 2/4

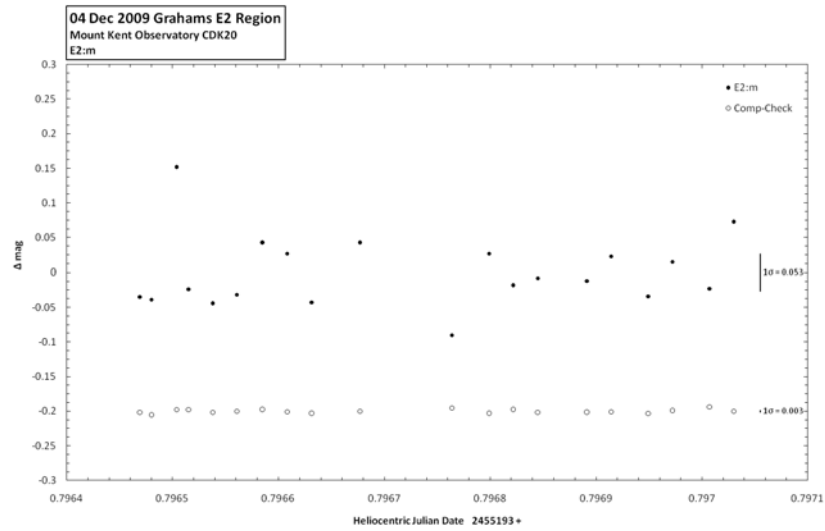
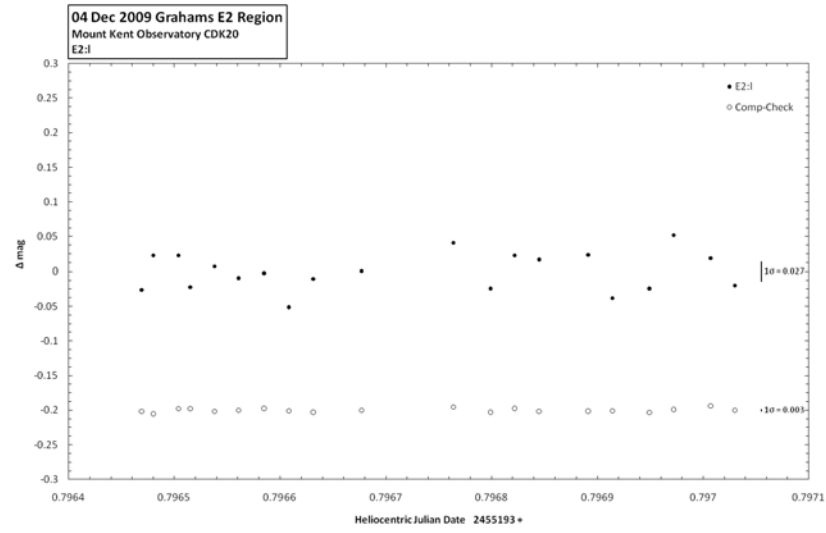
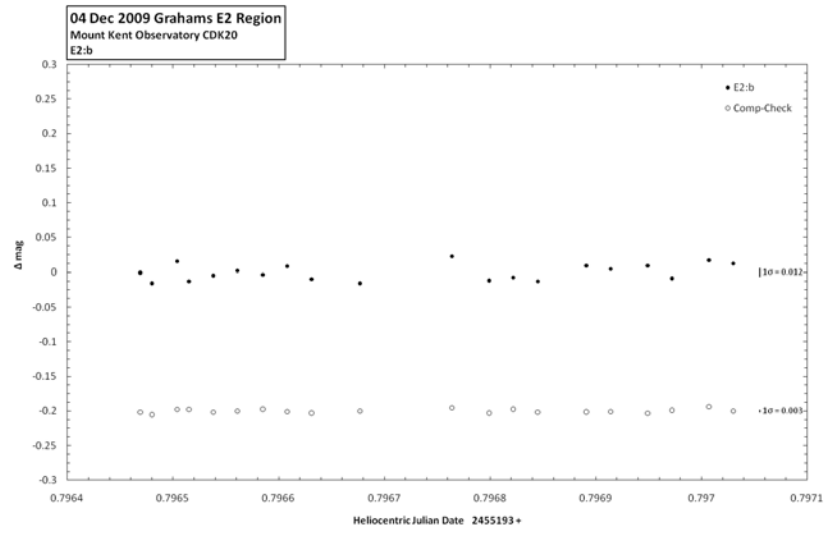


Figure B0.3 Graham's E2-Region standard star light curves - set 3/4

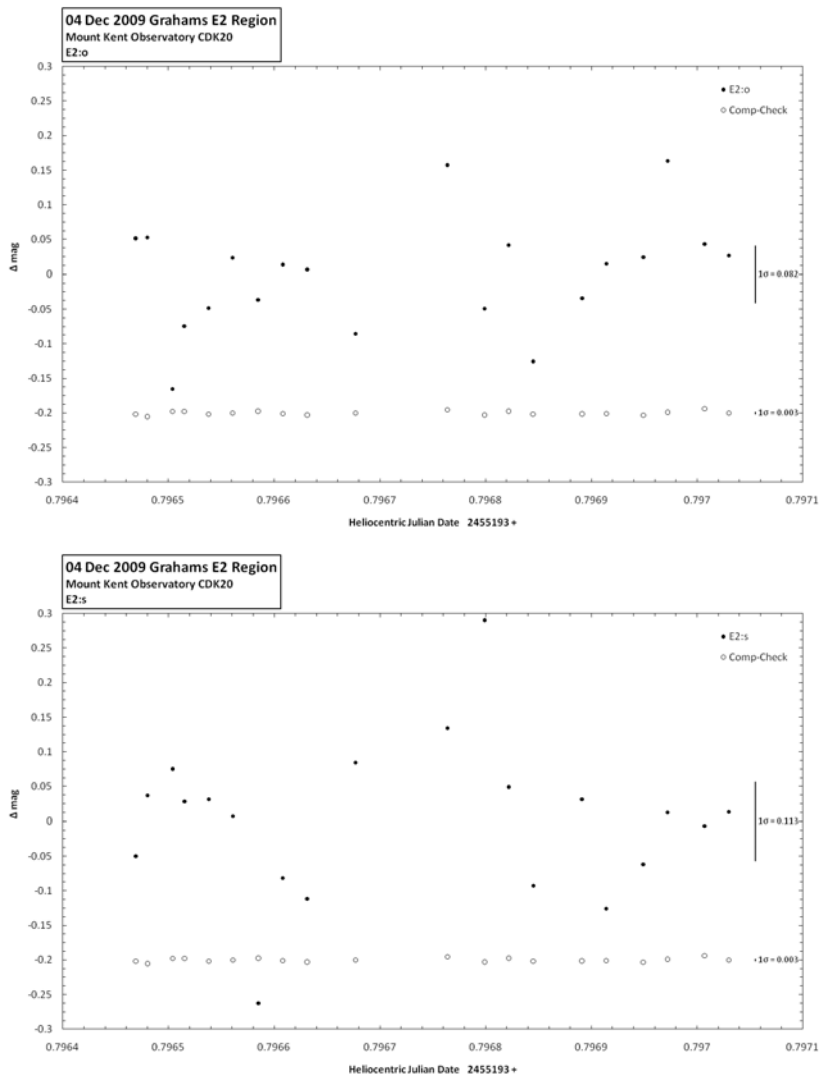


Figure B0.4 Graham's E2-Region standard star light curves - set 4/4

Appendix C IRAF photometry processing

C1 Introduction

All of the photometry analysis for this thesis was performed using IRAF running on a Ubuntu Linux virtual PC. IRAF is a command line based application and has no graphical user interface. To use the application effectively, the user must know the various commands (tasks in IRAF terminology) and be able to keep track of the processing flow manually. An IRAF guide was prepared by the author with assistance from Ian Waite so that a repeatable procedure was available whenever IRAF photometry processing was required. This Appendix presents the IRAF guide developed for this thesis. The opening page is a flowchart outlining the various stages of processing required. Each step of the flowchart is further expanded in the subsequent sections.

C2 IRAF guide

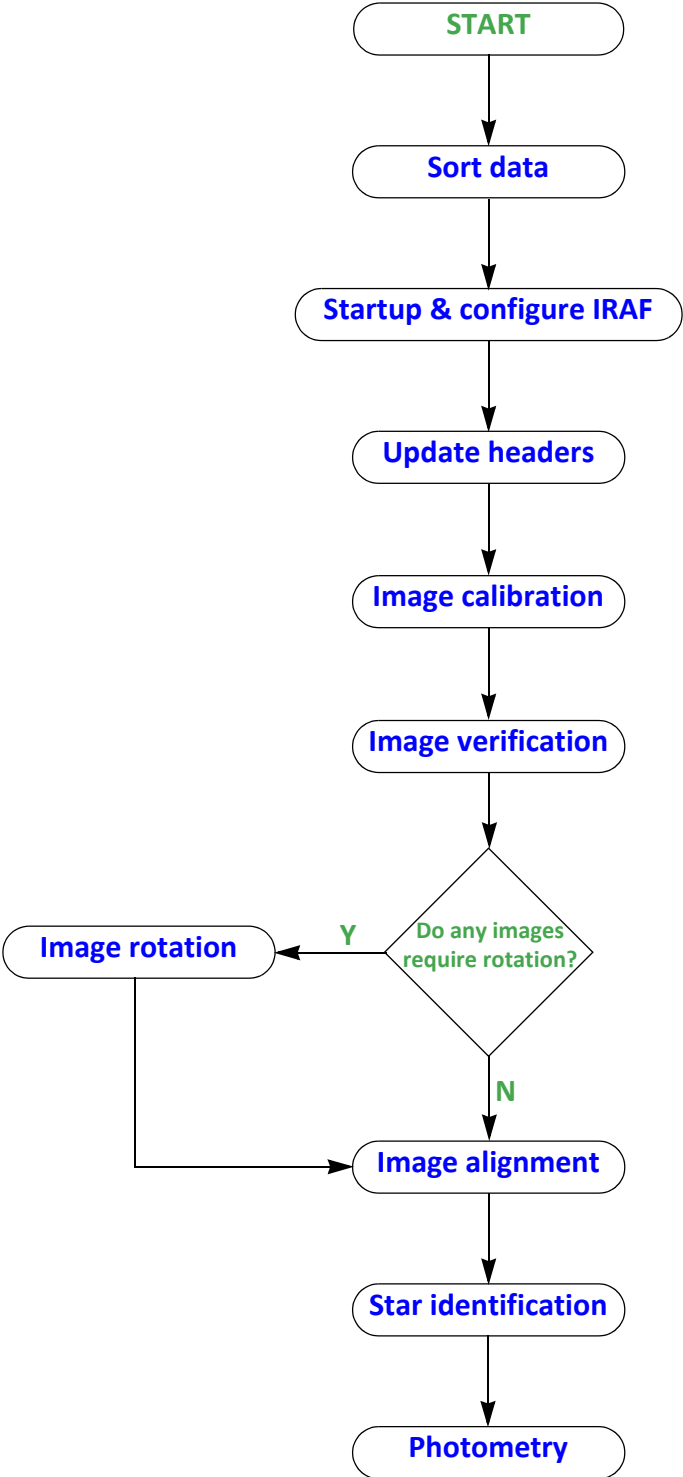


Figure C2.1 IRAF Photometry processing flowchart

C3 Sort data

A folder structure should be created to allow for a logical management of the observation data. The following folder structure is provided as an example:

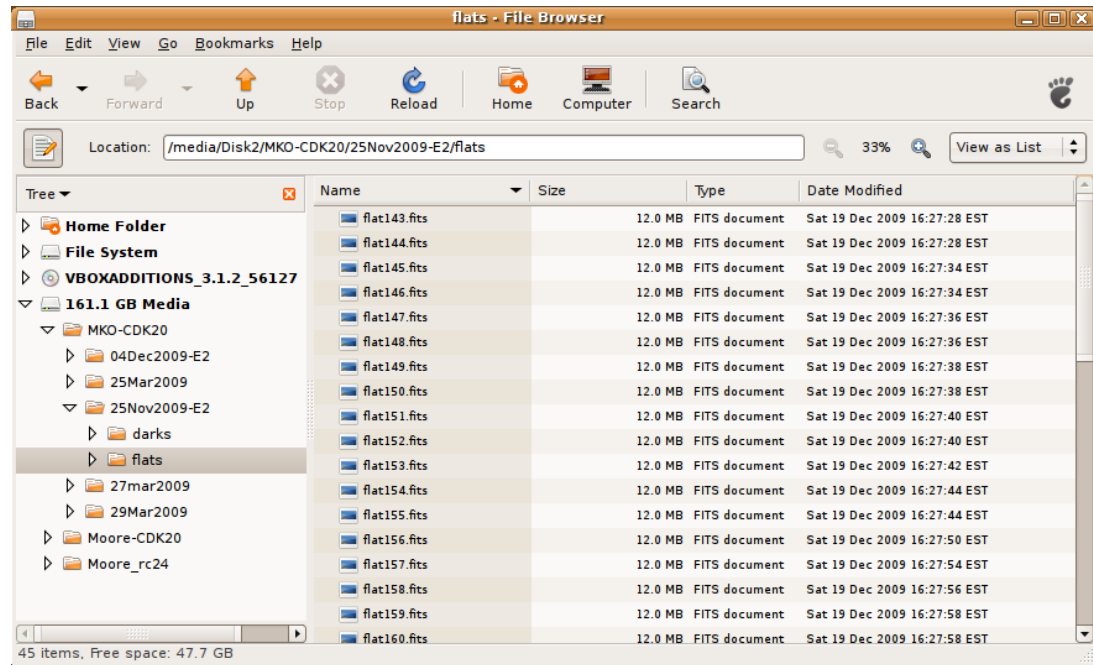


Figure C3.1 Observation data management

An important aspect of data processing is the efficient management of the astronomical data. The author used the Ubuntu Operating System running as a virtual machine on Windows 7[®]. Specific folders were created for all of the observation data used for this thesis.

All the calibration images are moved to the darks and flats folders and the science frames are moved to a dedicated folder for each target. A copy of the original observation data is kept in a separate folder on another network drive or NAS. This can then always be referred to if required.

C4 Startup & configure IRAF

C4.1 Observatory configuration

It is important to select the appropriate Observatory prior to undertaking any analysis in IRAF. There are two methods available to ensure that the observatory parameters are correctly set:

- 1) Set the obspars parameters from within the Observatory task.

The "observat" field tells IRAF what observatory data to use. An observatory database has been implemented in IRAF and observatory parameters are stored in

a simple text file. Various IRAF tasks obtain observatory related parameters by specifying an observatory identification. In the absence of a specific observatory database entry, the "observat" field can be set to "obspars". This means that the observatory parameters as defined in the parameters file of the observatory task are used.

- 2) Create a dedicated Observatory entry in the IRAF obsdb.dat file.

A more permanent method is to create an entry in the IRAF observatory database. This is achieved by editing the obsdb.dat file in /iraf/iraf/naoa/lib and creating a new entry at the end of the file. An example database entry is provided below for MKO and Moore Observatory:

```
# Created by J Monsour 26/07/2009
observatory = "mko"
name = "Mt Kent Observatory"
longitude = 208.14991111
latitude = -27.7994444444444
altitude = 683
timezone = -10

# Created by J Monsour 26/07/2009
observatory = "moore"
name = "Moore Observatory"
longitude = 85.5287194444444
latitude = 38.3447638888889
altitude = 216
timezone = 5
```

Figure C4.1 IRAF observatory database - example database entries

The author chose to use this option for all processing for this thesis.

```
noao> epar observatory
```

```
PACKAGE = noao
TASK = observatory

command = set Command (set|list|images)
obsid = moore Observatory to set, list, or image default
images = List of images
(verbose= no) Verbose output?

(observa= moore) Observatory identification
(name = Moore Observatory) Observatory name
(longitu= 85.5287194444444) Observatory longitude (degrees)
(latitud= 38.3447638888889) Observatory latitude (degrees)
(altitud= 216.) Observatory altitude (meters)
(timezon= 5.) Observatory time zone
override= mko Observatory identification
(mode = ql)
```

Figure C4.2 IRAF observatory parameters

When IRAF is started, the appropriate observatory can be selected by:

```
ec1> observatory set mko
```

C4.2 Navigate to appropriate folder

Change IRAF to the appropriate folder using:

```
ecl> cd [path to images]
```

C5 Update headers

The fits header information needs to be updated so that particular keywords are appropriately populated. In the case of MKO and Moore Observatory CDK20 telescopes, the following keywords need to be created or updated.

- a) observat
- b) obj_name
- c) rdnoise
- d) gain
- e) ut
- f) epoch
- g) mst
- h) HJD
- i) airmass

Once the headers have been updated, create a file containing a list of images using:

```
ecl> ls *.fits > image.list.1
```

Create a text file called “cmds” as follows (populate keywords as required):

```
observat = "mko"
observers = "Rhodes Hart"
obj_name = "E2 Region"
RA = "04:03:17"
DEC = "-44:36:18"
rdnoise = "13.5"
gain = "1.4"
date_obs = @'date-obs'
ut = @'date_obs'
epoch = epoch(@'date_obs')
mst = mst(@'date_obs',obsdb (observat, "longitude"))
```

Figure C5.1 Example IRAF obsdb.dat user defined observatories

The IRAF task *asthedit* can be used to update the headers of nominated images.

```
ecl> astutil
```

```
astutil> epar asthedit
```

```
PACKAGE = astutil
TASK = asthedit

images =          @sci.list  Images to be operated upon
commands=        cmds      File of commands
(table =         )          File of values
(colname=        )          Column names in table file
(prompt =        asthedit> ) Prompt for STDIN commands
(update =        yes)      Update image header?
(verbose=        no)       Verbose output?
(oldstyl=        no)       Use old style format?
(mode =         ql)
```

Figure C5.2 IRAF asthedit parameters

```
astutil> asthedit
```

C5.1 Set Julian date

The heliocentric Julian date is now added to the fits header. This is the time used when plotting the final light curves. The heliocentric Julian date is calculated and added to the header by using use *setjd* task.

```
astutil> epar setjd
```

```
PACKAGE = astutil
TASK = setjd

images =          @sci.list  Images
(observa=        moore)      Observatory of observation
(date =         date_obs)    Date of observation keyword
(time =         ut)          Time of observation keyword
(exposur=        exptime)    Exposure time keyword
(ra =           ra)          Right ascension (hours) keyword
(dec =          dec)         Declination (degrees) keyword
(epoch =        epoch)      Epoch (years) keyword

(jd =           jd)         Output Julian date keyword
(hjd =          hjd)        Output Heliocentric Julian date keyword
(ljd =          ljd)        Output local Julian date keyword

(utdate =        yes)       Is observation date UT?
(uttime =        yes)       Is observation time UT?
(listonl=        no)       List only without modifying images?
(mode =         ql)
```

Figure C5.3 IRAF setjd parameters

```
astutil> setjd
```

C5.2 Set airmass

This task will create and populate the airmass keyword.

```
astutil> epar setairmass
```

```
PACKAGE = astutil
TASK = setairmass

images = @sci.list Input images
(observa= moore) Observatory for images
(intype = beginning) Input keyword time stamp
(outtype= effective) Output airmass time stamp

(ra = ra) Right ascension keyword (hours)
(dec = dec) Declination keyword (degrees)
(equinox= epoch) Equinox keyword (years)
(st = mst) Local siderial time keyword (hours)
(ut = ut) Universal time keyword (hours)
(date = date_obs) Observation date keyword
(exposur= exptime) Exposure time keyword (seconds)
(airmass= airmass) Airmass keyword (output)
(utmiddl= utmiddle) Mid-observation UT keyword (output)
(scale = 750.) The atmospheric scale height

(show = yes) Print the airmasses and mid-UT?
(update= yes) Update the image header?
(overrid= yes) Override previous assignments?
(mode = ql)
```

Figure C5.4 IRAF setairmass parameters

```
astutil> setairmass
```

C6 Image calibration

Once the headers have been updated, the bias, dark and flat frames are processed. Load the following IRAF modules:

```
astutil> imred
```

```
imred> ccdred
```

C6.1 Bias frames

If bias frames have been taken, then it is necessary to combine the frames into a master bias frame using the IRAF task *zerocombine*. Median combine is generally used for this process.

ccdred> epar zerocombine

```
PACKAGE = ccdred
  TASK = zerocombine

input = @sci.list List of zero level images to combine
(output = biasa.fits) Output zero level name
(combine= median) Type of combine operation
(reject = minmax) Type of rejection
(ccdtype= ) CCD image type to combine
(process= no) Process images before combining?
(delete = no) Delete input images after combining?
(clobber= no) Clobber existing output image?
(scale = none) Image scaling
(statsec= ) Image section for computing statistics
(nlow = 0) minmax: Number of low pixels to reject
(nhigh = 1) minmax: Number of high pixels to reject
(nkeep = 1) Minimum to keep (pos) or maximum to reject
(neg)
(mclip = yes) Use median in sigma clipping algorithms?
(lsigma = 3.) Lower sigma clipping factor
(hsigma = 3.) Upper sigma clipping factor
(rdnoise= RDNOISE) ccdclip: CCD readout noise (electrons)
(gain = GAIN) ccdclip: CCD gain (electrons/DN)
(snoise = 0.) ccdclip: Sensitivity noise (fraction)
(pclip = -0.5) pclip: Percentile clipping parameter
(blank = 0.) Value if there are no pixels
(mode = ql)
```

Figure C6.1 IRAF zerocombine parameters

ccdred> zerocombine

This task generates *bias_master.fits* that will be used later in the processing.

C6.2 Dark frames

If a master bias frame exists, then it is necessary to subtract it from each of the dark frames as follows:

ccdred> imarith @dark.list - master_bias.fits @dark-bias.list

Sort the dark frames into groups based on exposure time. For each group, the individual dark frames can now be combined into a master dark frame (for a specific exposure time) using the IRAF task *darkcombine*. Median combine is generally used for this process.

ccdred> epar darkcombine

```
PACKAGE = ccdred
TASK = darkcombine

input = @sci.list List of dark images to combine
(output = Darkb.fits) Output dark image root name
(combine= median) Type of combine operation
(reject = minmax) Type of rejection
(ccdtype= ) CCD image type to combine
(process= no) Process images before combining?
(delete = no) Delete input images after combining?
(clobber= no) Clobber existing output image?
(scale = none) Image scaling
(statsec= ) Image section for computing statistics
(nlow = 0) minmax: Number of low pixels to reject
(nhigh = 1) minmax: Number of high pixels to reject
(nkeep = 1) Minimum to keep (pos) or maximum to reject
(neg)
(mclip = yes) Use median in sigma clipping algorithms?
(lsigma = 3.) Lower sigma clipping factor
(hsigma = 3.) Upper sigma clipping factor
(rdnoise= RDNOISE) ccdclip: CCD readout noise (electrons)
(gain = GAIN) ccdclip: CCD gain (electrons/DN)
(snoise = 0.) ccdclip: Sensitivity noise (fraction)
(pclip = -0.5) pclip: Percentile clipping parameter
(blank = 0.) Value if there are no pixels
(mode = ql)
```

Figure C6.2 IRAF darkcombine parameters

ccdred> zerocombine

This task generates *bias_master.fits* that will be used later in the processing.

C6.3 Flat frames

The following procedures are applied on a “per filter” basis. If a master bias frame exists, then it is necessary to subtract it from each of the flat field frames as follows:

ccdred> imarith @flat.list – master_bias.fits @flat-bias.list

The master dark frame with the same exposure time as the flats can now be subtracted using:

ccdred> imarith @flat-bias.list – master_dark.fits @flat-bias-dark.list

The individual flat frames can now be combined into a master flat frame using the IRAF task *flatcombine*. Median combine is generally used for this process.

```
ccdred> epar flatcombine
```

```
PACKAGE = ccdred
TASK = flatcombine

input = @sci.out List of flat field images to combine
(output = flat_v.fits) Output flat field root name
(combine= median) Type of combine operation
(reject = avsigclip) Type of rejection
(ccdtype= ) CCD image type to combine
(process= no) Process images before combining?
(subsets= no) Combine images by subset parameter?
(delete = no) Delete input images after combining?
(clobber= no) Clobber existing output image?
(scale = mode) Image scaling
(statsec= ) Image section for computing statistics
(nlow = 1) minmax: Number of low pixels to reject
(nhigh = 1) minmax: Number of high pixels to reject
(nkeep = 1) Minimum to keep (pos) or maximum to reject
(neg)
(mclip = yes) Use median in sigma clipping algorithms?
(lsigma = 3.) Lower sigma clipping factor
(hsigma = 3.) Upper sigma clipping factor
(rdnoise= RDNOISE) ccdclip: CCD readout noise (electrons)
(gain = GAIN) ccdclip: CCD gain (electrons/DN)
(snoise = 0.) ccdclip: Sensitivity noise (fraction)
(pclip = -0.5) pclip: Percentile clipping parameter
(blank = 1.) Value if there are no pixels
(mode = ql)
```

Figure C6.3 IRAF flatcombine parameters

```
ccdred> flatcombine
```

This task generates *flat_master.fits* that will be used later in the processing.

C6.4 Science frames

The science frames are now processed using the calibration frames that have just been created. The following procedures are applied on a “per filter” basis. If a master bias frame exists, then it is necessary to subtract it from each of the science frames as follows:

```
ccdred> imarith @sci.list - master_bias.fits @sci-bias.list
```

The master dark frame with the same exposure time as the science frames can now be subtracted using:

```
ccdred> imarith @sci-bias.list - master_dark.fits @sci-bias-dark.list
```

The science frames are now flat field corrected by dividing the science frames by the appropriate (by filter) master flat frame as follows:

```
ccdred> imarith @sci-bias-dark.list / master_flat.fits @sci-bias-dark-
flat.list
```

C7 Image verification

Now that all of the science frames have been properly calibrated, it is necessary to inspect each image to check the following:

- a) Image quality - note any unusable images (e.g. tracking or focusing issues etc.)
- b) Saturation - note any images with saturated targets
- c) Meridian flip - note the image filename where this occurs.

The IRAF *imexamine* task can be used to examine each image in turn:

```
ccdred> epar imexamine
```

```
PACKAGE = tv
TASK = imexamine

input = wasp12b_90_b_d_s.fits  images to be examined
(output = ) output root image name
(ncoutpu= 101) Number of columns in image output
(nloutpu= 101) Number of lines in image output
frame = 1 display frame
image = image name
(logfile= coord.log) logfile
(keeplog= yes) log output results
(defkey = a) default key for cursor list input
(autorede= yes) automatically redraw graph
(allfram= yes) use all frames for displaying new images
(nframes= 0) number of display frames (0 to autosense)
(ncstat = 5) number of columns for statistics
(nlstat = 5) number of lines for statistics
(graphicu= ) graphics cursor input
(imagecu= ) image display cursor input
(wcs = logical) Coordinate system
(xformat= ) X axis coordinate format
(yformat= ) Y axis coordinate format
(graphic= stdgraph) graphics device
(display= display(image='$1',frame=$2)) display command template
(use_dis= yes) enable direct display interaction
(mode = ql)
```

Figure C7.1 IRAF imexamine parameters

```
astutil> imexamine @image.list.1
```

The following commands are available when viewing an image:

- a) ‘,’ obtain basic details of star.
- b) ‘r’ generate a radial plot of the star (useful for detecting saturated targets).
- c) ‘n’ move on to next image.
- d) ‘p’ move back to previous image.
- e) ‘q’ quit the task.

If required, create a new text file called *image.rotate.in* containing a list of files to be rotated and *image.rotate.out* to specify the rotated filenames. Copy image.list.1 to image.list.2

```
astutil> cp image.list.1 image.list.2
```

Edit *image.list.2* to remove any bad images that have been identified and update the filenames of the images that will be rotated.

C8 Image rotation

Meridian flip occurs when the movement of the target requires the telescope on a German equatorial mount to move 180 degrees in azimuth. When this occurs, the subsequent images appear inverted relative to the preceding images. If this occurs, it is necessary to identify where the meridian flip occurred and then rotate all the subsequent images. Rotation is achieved using the IRAF *rotate* task. The files *image.rotate.in* and *image.rotate.out* created in the previous step are required.

```
astutil> epar rotate
```

```
PACKAGE = imgeom
TASK = rotate

input = @rot.list Input data
output = @rot.out Output data
rotation= 180. Rotation angle in degrees
(xin = INDEF) X origin of input image in pixels
(yin = INDEF) Y origin of input image in pixels
(xout = INDEF) X origin of output image in pixels
(yout = INDEF) Y origin of output image in pixels
(ncols = INDEF) Number of columns in the output image
(nlines = INDEF) Number of lines in the output image
(interpo= linear) Interpolant
(nearest,linear,poly3,poly5,spline3,sinc,lsinc,drizzle)
(boundar= nearest) Boundary extension
(nearest,constant,reflect,wrap)
(constan= 0.) Constant for constant boundary extension
(nxblock= 512) X dimension of working block size in
pixels
(nyblock= 512) Y dimension of working block size in
pixels
(verbose= yes) Print messages about the progress of the
task ?
(mode = ql)
```

Figure C8.1 IRAF rotate parameters

```
astutil> rotate
```

C9 Image alignment

The telescope moves slightly from one image to the next resulting in different pixels being illuminated by any given target. It is important to ensure that all images are properly aligned meaning that the x and y coordinates of the target stars are the same for each image in the set. This requirement is specified because of the way the photometry analysis is being performed in this guide, other methods of undertaking the photometry analysis are available and may not require image alignment or have any specific requirements on the target positions.

This guide makes the assumption that the observations have been made using a telescope fitted to a German Equatorial mount as is the case for the telescopes used in this thesis. Field rotation does not occur when using an equatorial mount, hence a procedure for managing rotated fields is outside the scope of this guide.

The process to align a set of images involves:

- a) Using imexamine task to find the location of a specific star in each image.
- b) Calculate the shifts required for each image (scilab script).
- c) Use the imalign task to align each image with respect to some reference image.

The first image in image.list.2 is arbitrarily chosen to be the reference image.

C9.1 Examine images & record target position

Remove any previously created log files from the imexamine task.

```
ccdred> !rm coord.log
```

Note: ! tells IRAF the command following is a unix command.

Run imexamine

```
ccdred> imexamine @image.list.2
```

The SAOImage ds9 image viewer is used to identify the target in each image. Its a good idea to magnify the image so that the cursor can be easily moved to the centre of the target. Place the cursor over the target star and press 'a'. IRAF will find the centroid position of the target and record the coordinates. Now press 'n' to move on to the next image. Repeat this process until all images have been processed. Press 'q' to quit imexamine.

The unix command grep is used to extract the lines from coord.log containing the data required (i.e. those lines containing the coordinates. Usually, the first character can be identified such as "1"). Grep does not run within IRAF so a terminal window is required to perform this task.

```
!: grep "^1" coord.log coordinates.dat
```

The grep command searches files or standard input globally for lines matching a given regular expression and prints them to the program's standard output.

^ = match empty string at the beginning of the line.

\$ = match empty string at the end of the line.

C9.2 Calculate coordinate shifts

It is now necessary to calculate the x and y shift from the reference position for each science frame. A scilab script is used for this task. Run scilab script `pixel_shift()` (refer C12).

```
--> y=read('coordinates.dat',-2,2)
--> z=pixel_shift(y)
```

This creates two files: *reference.coo* and *shifts.list*. *reference.coo* is a single line (position in the reference image) and *shifts.list* is a two column array of x and y shifts. *@image.list.2* is the text file containing the images filenames that are to be read. The first one should be the reference image.

Create *image.list.3* containing the filenames of the shifted images. For example, if the input image is *31455.fits*, the shifted image name might be *31455s.fits*.

C9.3 Image alignment

The IRAF `imalign` task is now run to shift each image. The task is setup as follows:

```
ccdred> epar imalign
```

```
PACKAGE = immatch
TASK = imalign

input = @sci.list Input images
referenc= wasp12b_5_b_d.fits Reference image
coords = reference.coo Reference coordinates file
output = @sci.out Output images
(shifts = shifts.list) Initial shifts file
(boxsize= 12) Size of the small centering box
(bigbox = 15) Size of the big centering box
(negativ= no) Are the features negative ?
(backgro= INDEF) Reference background level
(lower = INDEF) Lower threshold for data
(upper = INDEF) Upper threshold for data
(niterat= 3) Maximum number of iterations
(toleran= 0) Tolerance for convergence
(maxshif= INDEF) Maximum acceptable pixel shift
(shiftim= yes) Shift the images ?
(interp_ = linear) Interpolant
(boundar= nearest) Boundary type
(constan= 0.) Constant for constant boundary extension
(trimima= yes) Trim the shifted images ?
(verbose= yes) Print the centers, shifts, and trim
section ?
(list = )
(mode = ql)
```

Figure C9.1 IRAF `imalign` parameters

```
ccdred> imalign
```

C10 Star identification

C10.1 Determine full width at half maximum

Use the imexamine task to inspect the shifted images and determine the full width at half maximum (FWHM) for the science frames.

Place the cursor over a star. Press 'r' to see a radial profile for the star. Three estimates of the FWHM are provided in the bottom right hand side of the radial plot window. Measure a number of stars in the field to get a good sample. The FWHM should be the same for all stars in the field - a value between 3 and 5 pixels is normal.

Another way to determine FWHM is to press ',' while the cursor is over a star. This will print data about the star in the IRAF terminal window with the last column showing the maximum FWHM. However, it is better to view the radial profile and choose an integer value for the FWHM.

C10.2 Choose appropriate apertures

As a rule of thumb, the aperture radius should be chosen as 4 times the FWHM. For example, if the FWHM is 3 then the aperture radius chosen would be $3*4=12$ (Berry & Burnell 2009, Warner 2006).

A more scientific approach is to calculate the magnitude of the star through a number of apertures ranging from a radius of say 3 to 25 in steps of 1 (done as a one off process). The idea is that as the radius of the aperture increases, the instrumental magnitude decreases until any increase in the radius results in no further increase in the instrumental magnitude. This is the value of the instrumental magnitude to be used in any photometry analysis.

As a rule of thumb, choose the sky annulus value to be 10 more pixels out from the aperture size. For example if aperture size is 12 then sky annulus should be $12+10=22$. The dannulus parameter can be set to 10 pixels to get a good sampling of the background.

Summary:

```
FWHM
Aperture = 4 * FWHM
sky annulus = Aperture + 10
Sky annulus width = 10
```

```
ccdred> digiphot
digiphot> daophot
```

daophot> epar datapars

```
PACKAGE = daophot
TASK = datapars

(scale = 1.) Image scale in units per pixel
(fwhmpsf= 7.) FWHM of the PSF in scale units
(emissio= yes) Features are positive ?
(sigma = 10.) Standard deviation of background in
counts
(datamin= INDEF) Minimum good data value
(datamax= INDEF) Maximum good data value
(noise = poisson) Noise model
(ccdread= rdnoise) CCD readout noise image header keyword
(gain = gain) CCD gain image header keyword
(readnoi= 13.5) CCD readout noise in electrons
(epadu = 1.4) Gain in electrons per count
(exposur= exptime) Exposure time image header keyword
(airmass= airmass) Airmass image header keyword
(filter = filter) Filter image header keyword
(obstime= ut) Time of observation image header keyword
(itime = 1.) Exposure time
(xairmas= INDEF) Airmass
(ifilter= INDEF) Filter
(otime = INDEF) Time of observation
(mode = ql)
```

Figure C10.1 IRAF datapars parameters

Datamin and datamax can be used to exclude stars that are too faint or too bright. Set the min value fairly low and the max value fairly high. 10 and 50,000 are good values. Sometime setting these values can cause phot to fail to calculate mag. To avoid this issue, datamin and datamax can be set to INDEF.

daophot> epar findpars

```
PACKAGE = daophot
TASK = findpars

(thresho= 10.) Threshold in sigma for feature detection
(nsigma = 1.5) Width of convolution kernel in sigma
(ratio = 1.) Ratio of minor to major axis of Gaussian
kernel
(theta = 0.) Position angle of major axis of Gaussian
kernel
(sharplo= 0.2) Lower bound on sharpness for feature
detection
(sharphi= 1.) Upper bound on sharpness for feature
detection
(roundlo= -1.) Lower bound on roundness for feature
detection
(roundhi= 1.) Upper bound on roundness for feature
detection
(mkdetec= no) Mark detections on the image display ?
(mode = ql)
```

Figure C10.2 IRAF findpars parameters

daophot> epar daofind

```
PACKAGE = daophot
TASK = daofind

image = wasp12b_20_b_d_r_s.fits  Input image(s)
output = starpos.coo.4  Output coordinate file(s) (default:
image.coo.?)
(starmap= ) Output density enhancement image(s)
(skymap = ) Output sky image(s)
(datapar= ) Data dependent parameters
(findpar= ) Object detection parameters
(boundar= nearest) Boundary extension
(constant|nearest|reflect|wrap)
(constan= 0.) Constant for boundary extension
(interac= no) Interactive mode ?
(icomman= ) Image cursor: [x y wcs] key [cmd]
(gcomman= ) Graphics cursor: [x y wcs] key [cmd]
(wcsout = )_wcsout) The output coordinate system
(logical, tv, physical)
(cache = )_cache) Cache the image pixels ?
(verify = )_verify) Verify critical daofind parameters ?
(update = )_update) Update critical daofind parameters ?
(verbose= )_verbose) Print daofind messages ?
(graphic= )_graphics) Graphics device
(display= )_display) Display device
(mode = ql)
```

Figure C10.3 IRAF daofind parameters

The daofind task requires standard deviation of the background. This may be determined using the IRAF imstat task as follows:

daophot> imstat [reference image].fits

A few images should be examined to find an average.

Run daofind to identify stars in the image. If too many or not enough stars are identified, the threshold parameter may be varied. Aim to generate a list of say 30 stars.

daophot> daofind

The output from daofind (*starpos.coo.1*) is used to generate *starpos.coo.2* using the IRAF txdump task to extract only those parameters of interest.

daophot> txdump starpos.coo.1 xcenter,ycenter,mag > starpos.coo.2

The stars that have been identified can be viewed in ds9 by using the tvmark task. It is configured as follows:

daophot> epar tvmark

```
PACKAGE = tv
  TASK = tvmark

frame = 1 Default frame number for display
coords = starpos20.coo Input coordinate list
(logfile= ) Output log file
(autoolog= no) Automatically log each marking command
(outimag= ) Output snapped image
(deletio= ) Output coordinate deletions list
(command= ) Image cursor: [x y wcs] key [cmd]
(mark = circle) The mark type
(radii = 18,35,50) Radii in image pixels of concentric
circles
(lengths= 0) Lengths and width in image pixels of
concentric rectangles
(font = raster) Default font
(color = 204) Gray level of marks to be drawn
(label = no) Label the marked coordinates
(number = yes) Number the marked coordinates
(nxoffse= 15) X offset in display pixels of number
(nyoffse= -2) Y offset in display pixels of number
(pointsi= 5) Size of mark type point in display pixels
(txsize = 1) Size of text and numbers in font units
(toleran= 1.5) Tolerance for deleting coordinates in
image pixels
(interac= no) Mode of use
(mode = ql)
```

Figure C10.4 IRAF tvmark parameters

The radii parameter can be set to the values for annulus, sky annulus and sky annulus width to see concentric circles plotted on the image. e.g. 12,22,27.

daophot> display [reference image]

daophot> tvmark

Inspect the image and note any marked stars near the edge of the frame or too close together and remove them from *starpos.coo.2*.

Run scilab script `position_sort()` (refer C13).

Determine the number of stars in *starpos.coo.2*. This is used as an argument in the scilab script.

```
-->p=read('starpos.coo.2',#rows,#cols)
```

```
-->y=position_sort(p)
```

This creates two files: *position.sort* and *starpos.coo*.

Check *starpos.coo* to make sure the target star is the first entry.

daophot> tvmark

Confirm the star positions are okay and that target is labelled number 1. An example image showing the identified stars is provided in the following [Figure C10.5](#).

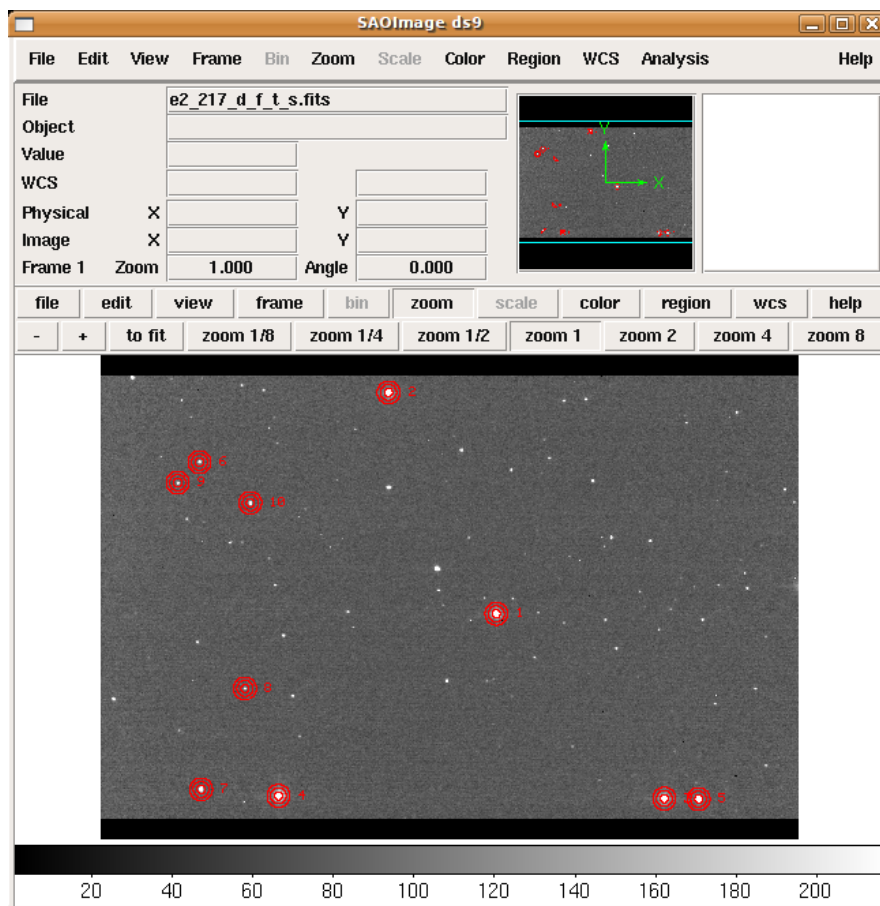


Figure C10.5 IRAF tvmark example

C11 Photometry

Photometry of the image set can now be performed. This is achieved using the IRAF phot task which has a number of associated parameter files. Each one is listed below:

daophot> epar fitskypars

```
PACKAGE = daophot
  TASK = fitskypars

(salgori=          mode) Sky fitting algorithm
(annulus=          35.) Inner radius of sky annulus in scale units
(dannulu=          10.) Width of sky annulus in scale units
(skyvalu=          0.) User sky value
(smaxite=          10) Maximum number of sky fitting iterations
(sloclip=          0.) Lower clipping factor in percent
(shiclip=          0.) Upper clipping factor in percent
(snrejec=          50) Maximum number of sky fitting rejection
iterations
(sloreje=          3.) Lower K-sigma rejection limit in sky sigma
(shireje=          3.) Upper K-sigma rejection limit in sky sigma
(khist =           3.) Half width of histogram in sky sigma
(binsize=          0.1) Binsize of histogram in sky sigma
(smooth =          no) Boxcar smooth the histogram
(rgrow =           0.) Region growing radius in scale units
(mksky =           no) Mark sky annuli on the display
(mode =            ql)
```

Figure C11.1 IRAF fitskypars parameters

Set the sky annulus and sky annulus width to the values previously determined.

daophot> epar photpars

```
PACKAGE = daophot
  TASK = photpars

(weighti=          constant) Photometric weighting scheme
(apertur=          25) List of aperture radii in scale units
(zmag =            20.) Zero point of magnitude scale
(mkapert=          no) Draw apertures on the display
(mode =            ql)
```

Figure C11.2 IRAF photpars parameters

Set the aperture to the value previously determined.

daophot> epar phot

```
PACKAGE = daophot
TASK = phot

image = @sci.list Input image(s)
coords = starpos.coo.3 Input coordinate list(s) (default:
image.coo.?)
output = default Output photometry file(s) (default:
image.mag.?)
skyfile = Input sky value file(s)
(plotfil= ) Output plot metacode file
(datapar= ) Data dependent parameters
(centerp= ) Centering parameters
(fitskyp= ) Sky fitting parameters
(photpar= ) Photometry parameters
(interac= no) Interactive mode ?
(radplot= no) Plot the radial profiles?
(icomman= ) Image cursor: [x y wcs] key [cmd]
(gcomman= ) Graphics cursor: [x y wcs] key [cmd]
(wcsin = )_.wcsin) The input coordinate system
(logical,tv,physical,world)
(wcsout = )_.wcsout) The output coordinate system
(logical,tv,physical)
(cache = )_.cache) Cache the input image pixels in memory ?
(verify = )_.verify) Verify critical phot parameters ?
(update = )_.update) Update critical phot parameters ?
(verbose= )_.verbose) Print phot messages ?
(graphic= )_.graphics) Graphics device
(display= )_.display) Display device
(mode = ql)
```

Figure C11.3 IRAF phot parameters

Set image list to *image.list.3*.

daophot> phot

Ensure that each line is reported as “ok” and that no “INDEF” strings appear in the output. Once the phot task has run without errors, the results (in individual *.mag.x* files) can be consolidated into a single output file using the *txdump* task as follows:

daophot> txdump *.mag.1 image,id,otime,xairmass,mag,merr > star.phot

The heliocentric JD needs to be recorded into a separate file. This is achieved using the following task:

daophot> hedit @image.list.3 "HJD" .> star.hjd

A scilab script is used to perform the differential photometry calculations on the data in *star.phot* and *star.hjd*.

Run scilab script *light_c20()* (refer C14).

--> *light_c20(#stars)*

This script requires the helper scilab script *sex2dec_fits()* to be loaded (Refer C15).

Running *light_c20()* creates a single user defined file containing the following data:

- a) HJD - Heliocentric Julian Date
- b) Delta Mag - difference in magnitudes

- c) OTC - time of observation
- d) Airmass
- e) Target
- f) C1, C2 ... Cx
- g) MErr - error in the magnitude
- h) Synthetic Comp.

This text file can now be further processed outside of IRAF as required.

C12 Scilab function: pixel_shift(pixel)

```
function [y] = pixel_shift(pixel);
    mdelete reference.coo
    mdelete shifts.list
    p = pixel;
    r = [pixel(1,1) pixel(1,2)]
    [a,b]=size(p);
    y=[];
    for i=1:a
        shift_x = (p(1,1)-p(i,1));
        shift_y = (p(1,2)-p(i,2));
        y=[y;shift_x shift_y]
    end
    write('reference.coo',r)
    write('shifts.list',y)
endfunction
```

C13 Scilab function: position_sort(p)

```
function [y] = position_sort(p);
    mdelete position.sort
    mdelete starpos.coo
    [j,k]=size(p)
    a=lex_sort(p,[3]);
    write('position.sort',a)
    y=[a(1:j,1),a(1:j,2)]
    write('starpos.coo',y)
endfunction
```

C14 Scilab function: light_c20(num_star)

```
function [y]=light_c20(num_star);
    aa=input('What is the file name containing the data :','s')
    fd1=mopen(aa,'r')
    bb=input('What is the file name containing the hjd :','s')
```

```

fd2=mopen(bb,'r')
data_c=[];
da=[];
num_comp=num_star-1;
disp('The data file is open and ready to be read')
funcprot(0);
while meof(fd1)==0
    data=[];
    for j=1:num_star
        star=mfscanf(fd1,'%s');
        star_id=mfscanf(fd1,'%f');
        ot=mfscanf(fd1,'%s');
        otime=sex2dec_fits(ot);
        airmass=mfscanf(fd1,'%f');
        mag=mfscanf(fd1,'%f');
        m_error=mfscanf(fd1,'%f');
        da=[star_id,otime,airmass,mag,m_error];
        data=[data;da]
    end
    data_c=[data_c;data]
end
fclose(fd1);
disp('The data file has been closed')
disp('Now reading the HJD file')
hjd=[];
while meof(fd2)==0
    image=mfscanf(fd2,'%s')
    eq=mfscanf(fd2,'%s')
    h_s=mfscanf(fd2,'%s');
    hj=evstr(h_s);
    hjd=[hjd,hj];
end
hjd=hjd';
fclose(fd2);
[nr,nc]=size(data_c);
num_image = (nr/num_star);
disp('Number of images to be analysed: ');
disp(num_image);
if num_image ~= round(num_image)
    disp('Warning: this is unlikely to provide reliable data')
    break
end
pl=1;
air=zeros(0,0);
otc=zeros(0,0);
mr=zeros(0,0);
magvec=zeros(0,0);
for i = 1:num_image
    otc=[otc;data_c(pl,2)];
    air=[air;data_c(pl,3)];
    mag=[data_c(pl:pl-1+num_star,4)];
    magvec=[magvec;mag];
    mr=[mr;data_c(pl,5)];
    pl=pl+num_star;
end

```

```

end
photarray=[hjd,otc,air,magvec,mr];
diff_hjd=max(hjd)-min(hjd);
disp('The range of time, in units of days')
disp(diff_hjd);
zpt=17;
csz=comp_star-zpt;
csz2=csz./(-2.5)
comp_star_int=10^(csz2);
syn_star_int=sum(comp_star_int,'c');
syn_star_mag=-2.5*log10(syn_star_int)+zpt;
diff_mag=photarray(:,4)-syn_star_mag;
y=[hjd,otc,air,photarray(:,4),syn_star_mag,mr]
z=[hjd,diff_mag]
j=[photarray,syn_star_mag,diff_mag]
aaa=input('Filename for results (y=[hjd,otc,air,target mag,syn_star_mag,mr]): ','s')
fd=mopen(aaa,'w')
disp('Opening the data file requested')
header="HJD OTC AIR Target ";
for i = 1:num_comp
    header=header+"C";
    header=header+string(i);
    header=header+" ";
end
header=header+"MErr Syn_Star Diff";
fprintfMat(aaa,j,"%f",header)
disp('Closing the data file')
fclose(fd)
av_hjd=mean(z(:,1))
av_m=mean(z(:,2))
stdev_hjd = stdev(z(:,1))
stdev_mag = stdev(z(:,2))
y=[av_hjd,av_m,stdev_hjd,stdev_mag]
disp('Average magnitude was :')
disp(av_m);
endfunction

```

C15 Scilab function: sex2dec_fits(t)

```

function [time]=sex2dec_fits(t);
if t <> [] then
    aa=ascii(t)
    hr=[aa(12),aa(13)]
    minute=[aa(15),aa(16)]
    sec=[aa(18),aa(19)]
    a_hr=evstr(ascii(hr));
    a_min=evstr(ascii(minute));
    a_sec=evstr(ascii(sec));
    time=a_hr+a_min/60+a_sec/3600;
else
    time=[]
end
endfunction

```

References

American Association of Variable Star Observers, website, viewed 04 September 2009, <<http://www.aavso.org/>>

Anglo-Australian Planet Search, website, viewed 18 August 2009, <http://www.phys.unsw.edu.au/~cgt/planet/AAPS_Home.html>

Automated Astronomy Group, website, viewed 22 February 2010, <http://schwab.tsuniv.edu/papers/baas/obsrep_94.html>

Baldwin G 2005, *The Teaching-Research Nexus*, University of Melbourne, Centre for the Study of Higher Education, viewed 6 January 2010, <http://www.cshe.unimelb.edu.au/pdfs/TR_Nexus.pdf>

Barnes TG et al. 1978, 'Stellar angular diameters and visual surface brightness. III - an improved definition of the relationship', *MNRAS*, Vol. 183, pp. 285-304.

Beaulieu, JP et al. 2006, 'Discovery of a cool planet of 5.5 Earth masses through gravitational microlensing', *Nature*, vol. 439, pp. 437-440.

Berry, R & Burnell, J 2009, *The Handbook of Astronomical Image Processing*, 2nd ed, 3rd printing, Willmann-Bell, Richmond.

Bond, I et al. 2004, 'OGLE 2003-BLG-235/MOA 2003-BLG-53: A Planetary Microlensing Event', *ApJ*, Vol. 606, pp. L155-L158.

Budding et al. 2001, 'The Active Algol Binary KZ Pavonis', *Astron. Soc. Aust.*, Vol. 18, pp. 140-147.

Buil, C 1991, *CCD Astronomy - Construction and use of an astronomical CCD camera*, 1st ed, Willmann-Bell, Richmond.

Carter, B et al. 2007, 'The Southern Skies Digital Science Partnership - Poster', <<http://www.astro.louisville.edu/information/asa2007.pdf>>

Clearskyinstitute, website, viewed 14 February 2010, <<http://www.clearskyinstitute.com/xephem/>>

Eker, Z 1999, 'Photometric Imaging of Starspots, Techniques and Reliability', *Turk. J. Phys.*, Vol. 23, No. 2, pp. 357 - 377.

Exoplanet Transit Database, website, viewed 09 October 2009, <<http://var2.astro.cz/ETD/index.php>>

Gardner, D, no date, 'Characterizing Digital Cameras with the Photon Transfer Curve'

Graham, JA 1982, 'UBVRI Standards in the E-Regions', *PASP* Vol. 94, pp. 244-265.

Hamacher, DW 2008, *A Search for Transiting Extrasolar Planets from the Southern Hemisphere*, p. 46

Hands-on Universe, website, viewed 22 February 2010, <<http://www.handsonuniverse.org/>>

Hebb, L et al. 2009, 'WASP-12b: The Hottest Transiting Extrasolar Planet Yet Discovered', *ApJ*, Vol 693, Iss 2, pp. 1920-1928.

Henden, A & Kaitchuck, R 1990, *Astronomical Photometry*, 2nd printing, Willmann-Bell, Richmond, p. 311.

Henry, GW et al. 1995, 'Starspot evolution, differential rotation, and magnetic cycles in the chromospherically active binaries lambda andromedae, sigma Geminorum, II Pegasi, and V711 Tauri', *ApJ*, Vol. 97, No. 2, pp. 513-549.

Hipparcos Epoch Photometry Search Facility, website, viewed 11 July 2010, <http://www.rssd.esa.int/index.php?project=HIPPARCOS&page=Epoch_Photometry>

Howell, SB 2006, *Handbook of CCD Astronomy*, 2nd ed, Cambridge University Press.

Instrument Neutral Distributed Interface, website, viewed 08 November 2009, <<http://www.indilib.org/index.php>>

International Amateur-Professional Photoelectric Photometry, website, viewed 04 September 2009, <<http://www.iappp.com/>>

Kielkopf et al. 2006, 'A Digital Science Partnership for Southern Skies in the Classroom - Poster', <<http://www.astro.louisville.edu/information/aas2006reva.pdf>>

Kielkopf et al. 1998, 'Spatial distribution of ions and molecules in Comet Hale-Bopp', *Bulletin of the American Astronomical Society*, Vol. 30, p. 1065.

Kjeldsen, H & Frandsen, S 1992, 'High-Precision Time-Resolved CCD Photometry', *PASP* Vol. 104, pp. 413-434.

Kodak 2005 *CCD Image Sensor Noise Sources*, Rev. 2.1.

Las Cumbres Observatory Global Telescope Network, website, viewed 22 February 2010, <<http://lco.net/>>

Marsden, S 2002, 'Solar-type stars in the young open clusters IC 2391 and IC 2602', PhD thesis, University of Southern Queensland, Toowoomba.

Marsden, S 2005, 'Doppler imaging and surface differential rotation of young open cluster stars - I. HD 307938 (R58) in IC 2602', *MNRAS*, Vol 359, Iss 2, pp. 711-724.

McLaughlin, DB 1924, 'Some results of a spectrographic study of the Algol System', *ApJ*, Vol. 60, pp. 22.

McLean, I 2008, *Electronic Imaging in Astronomy*, 2nd ed, Praxis Publishing, Chichester, UK.

Moore Observatory, website, viewed 14 February 2010, <<http://www.astro.louisville.edu/moore>>

Narita, N et al. 2007, 'Measurement of the Rossiter–McLaughlin Effect in the Transiting Exoplanetary System TrES-1', *PASJ*, Vol. 59, pp. 763-770.

NASA Kepler Mission, website, viewed 10 January 2010, <<http://kepler.nasa.gov/>>

NASA Mission News, website, viewed 10 January 2010, <<http://www.nasa.gov/topics/universe/features/exoplanet-20090528.html>>

NASA PlanetQuest, website, viewed 10 January 2010, <<http://planetquest.jpl.nasa.gov/>>

Ohta, Y et al. 2005, 'The Rossiter–McLaughlin Effect and Analytic Radial Velocity Curves for Transiting Extrasolar Planetary Systems', *ApJ*, Vol. 622, pp. 1118-1135.

Pan-STARRS, website, viewed 22 February 2010, <<http://pan-starrs.ifa.hawaii.edu/public/>>

PlaneWave Instruments, website, viewed 13 February 2010, <<http://www.planewave.com/>>

Pont, F et al. 2006, 'The effect of red noise on planetary transit detection', *MNRAS*, Vol. 373, pp. 231-242.

Rabus, M et al. 2009, 'A cool starspot or a second transiting planet in the TrES-1 system?', *A&A*, Vol. 494, pp. 391-397.

ROBOsky, website, viewed 22 February 2010, <<http://www.robosky.com/>>

Rodono, M et al. 1995, 'Starspot evolution, activity cycle and orbital period variation of the prototype active binary RS Canum Venaticorum', *Astronomy and Astrophysics*, Vol. 301, p. 75.

Rossiter, RA 1924, 'On the detection of an effect of rotation during eclipse in the velocity of the brighter component of Beta Lyrae, and on the constancy of velocity of this system', *ApJ*, Vol. 60, p. 15.

Schlesinger, F 1910, 'The Algol-Variable δ Libræ', *Publ. Allegheny Obs.*, Vol. 1, p. 123

Schultz, AB 1999, 'Imaging Planets about other Stars with NGST', SPIE Conf. 3759, pp. 49-58.

Shared Skies Partnership, website, viewed 14 July 2010, <<http://www.sharedskies.org>>

SkyMapper, website, viewed 22 February 2010, <<http://www.mso.anu.edu.au/skymapper/>>

SLOOH, website, viewed 22 February 2010, <<http://www.slooh.com/>>

Southern Skies Digital Science Partnership, website, viewed 14 February 2010, <<http://www.astro.louisville.edu/software/>>

Stentz, A 2001, 'Robotic Technologies for Outdoor Industrial Vehicles', Proc. SPIE Vol. 4364, pp. 192-199.

Strassmeier, KG et al. 2010, 'The STELLA Robotic Observatory on Tenerife', Advances in Astronomy, Vol. 2010, Article ID 970306, 11 pages, 2010.

Tingley, B 2004, 'Using color photometry to separate transiting exoplanets from false positives', A&A, Vol. 425, p. 1125.

The Ohio State University, MicroLensing Follow-Up Network, website, viewed 12 December 2009, <<http://www.astronomy.ohio-state.edu/~microfun/ob06109/>>

Transitsearch.org, website, viewed 14 August 2009, <<http://www.transitsearch.org/>>

USQ Strategy, website, viewed 22 February 2010, <<http://www.usq.edu.au/aboutusq/strategy>>

Vogt, S et al. 2010 'A Super-Earth and two Neptunes Orbiting the Nearby Sun-like star 61 Virginis', ApJ, Vol. 708, Iss 2, pp. 1366-1375.

Warner, BD 2006 *Lightcurve Photometry and Analysis*, Springer Science+Business Media.

Wikipedia, Gravitational Microlensing, website, viewed 12 December 2009, <http://en.wikipedia.org/wiki/Gravitational_microlensing>

Wikipedia Zeeman Doppler Imaging, website, viewed 01 December 2009, <http://en.wikipedia.org/wiki/Zeeman-Doppler_imaging>

Wright, JT et al. 2009 'Ten New and Updated Multi-planet Systems, and a Survey of Exoplanetary Systems', ApJ, Vol. 693, Iss 2, pp. 1084-1099.